Investigation of tunnel junctions on proximitized topological insulator nanoribbons

presented by

Dennis Heffels

October 2020

A master's thesis submitted to the Faculty of Mathematics,
Computer Science and Natural Science at RWTH Aachen

prepared at
Peter Grünberg Institut (PGI-9)
Forschungszentrum Jülich

1st examiner: Prof. Dr. Detlev Grützmacher
2nd examiner: Prof. Dr. Markus Morgenstern

Abstract

Since A. Yu. Kitaev predicted in 2001 that quasi-one-dimensional p-wave superconductors are a possible platform for Majorana bound states (MBSs), numerous experiments have been conducted to find signatures and prove the existence of these MBSs. The majority of these experiments focused on tunnel spectroscopy on proximitized III-V semiconductor nanowires. Another possible platform to realize this exotic superconductivity are 3D topological insulators (3D-TIs) proximitized by s-wave superconductors. A major challenge to perform such tunnel spectroscopy experiments on 3D-TIs is the prevention of deterioration of the sensitive 3D-TI surface and the additional need to fabricate a suitable tunnel barrier. In this thesis selective area epitaxy of BiSbTe is conducted to obtain nanoribbons of this 3D-TI. Moreover, a multi-stage *in situ* fabrication technique for the assembly of tunnel junctions at the ends of niobium-proximitized BiSbTe nanoribbons is demonstrated. The process presented here allows to grow and deposit nanostructures of four different materials completely under UHV (ultra-high vacuum) conditions, i.e. *in situ*. First measurements at ultra-low temperatures were performed on tunnel junctions fabricated with this method. Two different models are derived and discussed to provide a physical explanation of the features shown in these measurements. Additionally, I present quantum transport simulations of such proximitized 3D-TI tunnel junctions.

Table of Contents

1 Introduction

Today we live in the age of the digitalization of information. Never before in human history has the processing and transmission of information been so efficient and cost-effective. This revolution in information processing was facilitated by micro- and nanoelectronics. Nanoelectronics, in turn, would not work without the development of quantum mechanics making it possible to calculate the behavior of circuits at atomic scale. Thus quantum mechanics has become an essential part of modern life.

Today's computers are engineered by the principles of quantum mechanics. Information processing, however, is still purely classical, realized by processing binary states (the classical bit) defined as 1 and 0. Information, however, can also be processed by following the laws of quantum mechanics. A computer that is capable of processing quantum information is generally called a quantum computer. The smallest possible information unit of a quantum computer is a qubit (i.e. the quantum analog to a classical bit). The qubit is a quantum mechanical two-state system with the states $|1\rangle$ and $|0\rangle$. According to the rules of quantum mechanics, the qubit can be in any superposition state of the individual states (of the eigenbasis). Only after the measurement the qubit is unambiguously fixed to one of the two distinguishable states $|1\rangle$ and $|0\rangle$. It is expected to provide a considerable speed advantage in solving certain problems. Especially the simulation of quantum mechanical processes [1] (e.g. in chemistry, solid state physics) requires huge computational resources on conventional computers and could be accelerated considerably on quantum computers.

However, the realization of a universal quantum computer is extremely difficult and the question whether it is even possible to build a quantum computer that offers relevant advantages over classical computers can be considered an open research question. The biggest challenge in realizing a quantum computer is to maintain the coherence of the quantum mechanical state, which encodes the information. Even the smallest disturbances affect the quantum states. Such quantum errors hinder the realization of high-performance logical qubits that can store information on arbitrarily long time scales. Quantum error correction algorithms have been developed to counteract this problem [2]. However, they considerably increase the number of physical qubits needed for a calculation. In order to realize fault-tolerant quantum processors it is important to make the quantum mechanical state and the operations on it less prone to errors/noise, to reduce the required number of physical qubits in the circuit that are needed for error correction.

A novel class of materials that have caused a small revolution in solid state physics may offer the solution. These materials are called TIs (topological insulators) and have the special property that their band structure is topologically nontrivial. This means that a continuous change of system parameters (e.g., due to disorder or impurities) does not affect the physical properties of the material that are determined this nontrivial topology (the topological invariant does not change). This results in some extraordinary properties that may allow to realize topological quantum computers. So the quantum computer realized with these materials inherits basically the protection against disorder or noise from the TI [3].

Theoretically, it should be possible to transfer the topological properties of the TI to the qubits by means of special quasiparticle excitations. These quasiparticles are known as MBSs (Majorana bound states) and they follow nonabelian statistics. This nonabelian statistics makes so-called braiding possible by swapping MBSs in a register that allows the execution of quantum algorithms [4, 5]. The peculiarity about this is that the state of the Majorana qubit is encoded in the fermion parity which is shared nonlocally by the MBSs. Hence, local disorder or noise do not affect the algorithm or the coherence of the state.

The existence of Majorana particles was first predicted in 1937 by Ettore Majorana [6]. In solid state physics so-called MBSs or just “Majoranas” manifest themselves as an equal superposition of electron and hole at zero energy. Numerous experiments have been conducted to prove the existence of MBSs [7-9]; however, this has been proven to be extremely difficult.

A possible platform for the generation of MBSs are superconducting proximitized TIs. The requirements for the fabrication of such structures pose extreme challenges for the quality of the materials used as well as for their interfaces [10].

However, the proof of the existence of MBSs is an important step towards quantum computing based on braiding. In this thesis a TI nanoribbon is brought into contact with a superconductor. Through a tunnel contact the local density of bound states can be resolved at the end of the nanoribbon. Such experiments have already been performed on proximitized III-V semiconductor nanowires [7, 11-15] . A signature for MBS in such tunnel experiments is a peak in conductance at zero-bias voltage which has already been detected for the III-VI semiconductor nanowires. Even when the challenges of fabrication are overcome, the interpretation of ZBP (zero-bias peak) signatures indicating the existence of MBSs is difficult as there are numerous physical effects that can cause similar results [16, 17].

The special feature of the approach used in this thesis is the use of a 3D-TI as well as the complete *in situ* fabrication of the tunnel junction. The great importance of the *in situ* fabrication is supported by previous works [18, 19], which have highlighted the need for a high quality interface.

2 Theory

In 2001 A. Yu. Kitaev showed theoretically the existence of MBSs in one-dimensional (1D) p-wave superconductor. Here, we consider the proposal for realizing a 1D p-wave superconductor and MBSs based on proximitized 3D-TIs. By applying a layer of a s-wave superconductor to a normally non-superconducting 3D-TI, the topological material becomes superconducting at the interface to the superconductor itself. The s-wave superconductor induces superconductivity in the TI, which is known as the proximity effect. Due to the special properties of TIs, the induced superconductivity has p-wave character. To achieve the required one-dimensionality a nanowire (or nanoribbon) made of 3D-TI is used. Such TI nanowires have special properties that make it necessary to apply an in-plane magnetic field (to close the gap) to realize MBSs in such a nanowire.

In this chapter the theoretical basics of MBSs in 3D-TI nanowires (or ribbons) are explained. Section 2.1 describes the essential properties of 3D-TIs and their typical surface states. Section 2.2 explains the basic properties of superconductors. For a microscopic understanding the Bogoliubov-de Gennes Hamiltonian is introduced. The proximity effect, which is important for the appearance of MBS, is also briefly described. For the behavior of NS (normal conductor-superconductor) interfaces, the Andreev reflection is essential and is therefore also treated. Section 2.3 briefly explains the basic properties of MBSs. Finally, Section 2.4 gives an introduction to tunneling spectroscopy to provide a better understanding of the experimental procedure and the interpretation of the results.

2.1 Topological insulators

The classification of different phases of matter is a common procedure in condensed matter physics. For example, the superconducting state can be described as a separate phase. This division into phases is done in the usual way with the Landau theory of phase transitions. In the last 15 years, a new way of classifying has been established according to topological classification [20, 21].

In mathematics, the topology describes structures that retain their properties with continuous deformation e.g., twisting or stretching. A common picture is that of a cup that converts into a torus or donut with the topology being unchanged. A central concept of topology is the definition of topological invariants with the help of which it is possible to distinguish different topologies. The number of holes in a body is such an invariant. Since cup and torus have the same number of holes one can use this invariant to classify these objects under the same topology.

In 1982 Thouless, Kohmoto, Nightingale and de Nijs (TKNN) [22] showed how this mathematical concept of topological invariants can be used to explain the integer QHE (quantum Hall effect). TKNN showed more precisely that the protected current carrying boundary states (1D) for which the QHE is known can be understood in a topological view. We consider the Bloch Hamiltonian $\mathrm{H}(\mathbf{k})$ whose band structure has a band gap. A topology can be assigned to this Hamiltonian using the so-called Chern number, which is the topological invariant in this context. As long as the continuous deformations of the Bloch Hamiltonian do not close the band gap the Chern number and thus the topology of the Bloch Hamiltonian does not change. Hence the Chern number is the equivalent of the number of holes in a solid body e.g. a torus. This makes the topology and thus the physical properties very robust. TKNN showed that the characteristic Hall conductivity associated with the integer QHE is calculated as follows $\sigma_{xy} = ne^2/h$, where the Hall conductivity is directly related to the total Chern number n. This explains why the quantization of the conductivity of the integer QHE is so robust to interference [3]. For example, moderate amounts of disorder cannot change the topology of the Hamiltonian because they cannot close the bulk band gap.

The Chern number can be understood from the physical point of view using the Berry phase

$$\gamma(\mathrm{C}) = \mathrm{i} \oint_{\mathrm{C}} \langle u_m(\boldsymbol{k}) | \nabla_{\boldsymbol{k}} | u_m(\boldsymbol{k}) \rangle \, d\boldsymbol{k} = \oint_{\mathrm{C}} \boldsymbol{A}_m(\boldsymbol{k}) d\boldsymbol{k} \tag{2.1}$$

where the states $|u_m(\boldsymbol{k})\rangle$ are the Bloch eigenstates of $\mathrm{H}(\mathbf{k})$ with m the index for the occupied bands. The state $|u_m(\boldsymbol{k})\rangle$ accumulates a Berry phase along path C in reciprocal space. For a closed path C, the so-called Berry flux $\boldsymbol{F}_m = \nabla \times \boldsymbol{A}_m$ can be defined. The Chern number

$$n_m = \frac{1}{2\pi} \int_{\mathrm{BZ}} \boldsymbol{F}_m \, d^2\boldsymbol{k} \tag{2.2}$$

can now be defined as integral over the entire Berry flux $\boldsymbol{F}_m$ of the Brillouin zone (BZ). The Chern number n_m is quantized and the total Chern number $n = \sum_{m=1}^{N} n_m$ is obtained by summing over occupied bands m up to the total number of occupied bands N. In this context it is also important to mention that TRS (time reversal symmetry) is broken in the system if the Chern number is nonzero.

The preceding brief description of the QHE was only intended to give a simple introduction to the concept. Central in this context is to describe the electronic structure of condensed matter systems by means of their topological properties. For TIs, the underlying concepts are similar. In comparison to QHE, however, the TRS is not broken for TI. This makes it necessary to define a different topological invariant than the Chern number ($n = 0$ for all TI). TIs are described with topological invariants $\mathbb{Z}_2$ which can be either 0 or 1 with unbroken TRS. For 2D TI a single topological invariant ν_0 is sufficient. However, the description of 3D-TIs requires four invariants (ν_0, ν_1, ν_2, ν_3), which results in 16 different topological phases (topological equivalence classes for the Bloch Hamiltonian) [23]. These 16 different topological phases are divided into weak and strong topological isolators on the basis of the invariant ν_0. 3D-TIs with $\nu_0 = 1$ possess topologically protected states on all 6 surfaces (for one cuboid) and are therefore called strong topological isolators. While TIs with $\nu_0 = 0$, which are called weak topological isolators, do not have topologically protected states on all surfaces. The topologically protected surface states (2D) are basically equivalent to the edge states (1D) existing in QHE. Since the exact treatment of all these topological phases and the derivation of the topological invariants would go beyond the scope of this thesis, we refer to the work of Fu, Kane, and Mele [23] and Moore and Balents [24], Roy [25]. In this thesis only strong TIs are used so only their properties are described in the following section.

TIs get their topologically nontrivial properties from a band inversion at the Γ point. The inversion of the bands is caused by three different physical effects, which are normal chemical bonds between the elements forming the crystal, the crystal-field effect and spin-orbit coupling. All these effects lead to a hybridization of orbitals as shown in Figure 2.1. The shift in energy levels is so large that the valence band and conduction band are reversed at the Γ point. This causes a band inversion and reversed the parity of the bands that is shown in Figure 2.2.

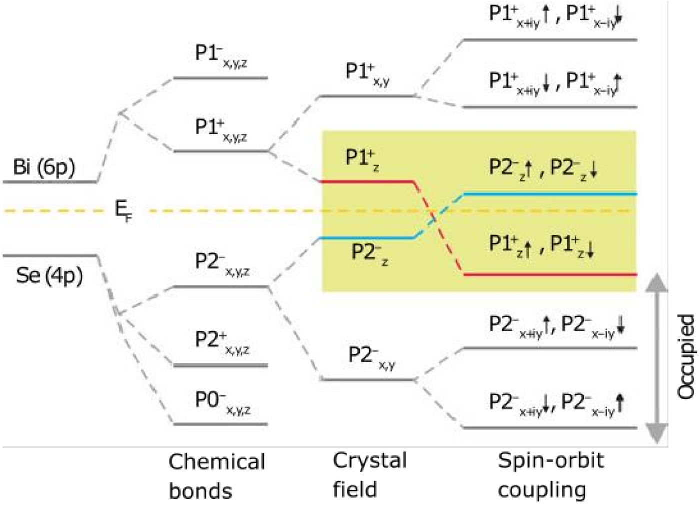

Figure 2.1: Schematic representation of the orbitals of Bi_2Se_3 involved in the conduction and valence bands and their splitting by effects of chemical bonding, crystal field, and spin-orbit coupling at the Γ point. Figure taken from Ref. [26].

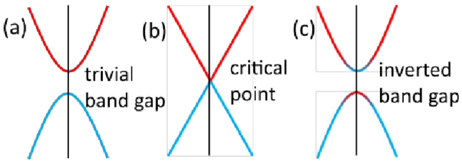

Figure 2.2: Schematic representation of the band inversion of the trivial band gap a) that closes b) through the effects shown in Figure 2.1 and opens again c) with exchanged orbital character near the point of symmetry. Figure taken from Ref. [27].

When a material band structure inverted in this way (nontrivial topology) is brought into contact with a topologically trivial insulator (this can also be a vacuum), the bands connect with the same parity via the interface and the connection must therefore cross the band gap. This band crossing induces a gapless band structure along the interface with surface or edge states that have a metallic character. In other words, the nontrivial topology of the bulk Hamiltonian is connected to the appearance of states at the boundary, known as bulk-boundary correspondence. The dimension of the band structure is one lower as that of the bulk, so a 2D interface for 3D bulk and 1D interface for 2D bulk. The TI has surface or edge states that can be directly traced back to its nontrivial topology. These are not to be confused with surface states as found in nontopological materials (e.g. caused by open chemical bonds). Since these surface or edge states do not have a protected gapless band structure that is robust along the whole interface. The topological surface and edge states have a linear dispersion and can be described by a massless Dirac Hamiltonian [26, 28]:

$$H(\boldsymbol{k}) = \hbar v_D\left(\sigma_x k_y - \sigma_y k_x\right) \tag{2.3}$$

Here $\hbar$ is the reduced Planck constant, v_D the Dirac velocity, k_x and k_y the wave vectors of the electronic states and σ_x and σ_y are the Pauli matrices acting on a spin-1/2 basis. The eigenstate spectrum

$$E(\boldsymbol{k}) = \pm v_\mathrm{D}\hbar|\boldsymbol{k}|. \tag{2.4}$$

is linear in momentum. Because this dispersion is a rotationally symmetric cone and is derived from the Dirac equations it is called a Dirac cone. The bands with positive and negative energies described by the last equation meet in a zero-dimensional point called the Dirac point. In the simple case described here this is at a momentum of $\boldsymbol{k} = 0$ with an energy $E = 0$.

A closer look at the structure of the energy eigenstates reveals some highly interesting transport properties. The spin is uniquely tied to the momentum and the direction of the spin is always perpendicular to the direction (spin-momentum locking). Therefore direct backscattering (Umklapp scattering) is prohibited if time reversal symmetry is not broken (e.g., due to magnetic impurities) because the state at $-k$ has the orthogonal spin. In Figure 2.5 this spin polarization is plotted together with a 2D Dirac cone. These properties have caused great interest in TIs. They are now being investigated for a variety of applications, including spintronics, thermoelectronics and of course quantum computing.

In this thesis I investigate MBE (molecular beam epitaxy) grown grow $(Bi_{1-x}Sb_x)_2Te_3$ ternary (3D-TI material) nanoribbons. The properties of quasi-1D nanoribbons are more complicated because the confinement leads to a quantization of a k component. The topological protection against direct backscattering, for example, disappears in the quasi-1D case. This fact will be discussed in the following section by considering theoretically a cylindrical nanowire.

2.1.1 Topological insulator nanostructures under the influence of a magnetic field

For a quasi-1D nanowire, the surface state Dirac cone transforms into subbands and a gap opens at the Dirac point in the dispersion relation. For the calculations shown here, cylindrical coordinates are chosen for simplification. A cylindrical nanowire is assumed, but the results of the calculations are generally valid for an arbitrary cross-section as long as there is a sufficiently large bulk region. At the beginning of the derivation we start in normal Cartesian coordinates without an external magnetic field. For this the following Dirac Hamiltonian can be used

$$h_0 = \frac{v_D}{2}[\hbar\nabla \cdot \boldsymbol{n} + \boldsymbol{n} \cdot (\boldsymbol{p} \times \boldsymbol{s}) + (\boldsymbol{p} \times \boldsymbol{s}) \cdot \boldsymbol{n}]. \tag{2.5}$$

where $\boldsymbol{n}$ is a unit vector normal to the nanowire surface, $\boldsymbol{s}$ is a vector of the Pauli matrices and $\boldsymbol{p}$ is the momentum operator $\boldsymbol{p} = -i\hbar\nabla$ [29]. The cylindrical coordinates are naturally chosen such that the radius r describes the distance from the center of the wire to the surface states. The z coordinate is chosen such that it is aligned with the wire. With the consideration of the magnetic field and the use of cylindrical coordinates the following Hamiltonian is obtained for a cylindrical nanowire

$$h = \frac{1}{2r} I_{2\times2} + (\boldsymbol{n} \times \boldsymbol{\pi}) \cdot \boldsymbol{s} + \boldsymbol{s} \cdot \boldsymbol{m}. \tag{2.6}$$

With the additional parameter $\boldsymbol{m} = m\hat{z}$ representing the Zeeman coupling to the external magnetic field [30]. In order to take into account the orbital effect of the magnetic field, the momentum operator $\boldsymbol{p} = -i\hbar\nabla$ is substituted by $\boldsymbol{\pi} = \boldsymbol{p}\text{-}(e/c)\boldsymbol{A}$ with the magnetic vector potential $\boldsymbol{A}$, the electron charge e and the speed of light c. This is known as the minimal coupling procedure. By choosing these coordinates the following vector potential is obtained to describe a magnetic field in z direction along the wire

$$\boldsymbol{A} = \eta\Phi_0(\hat{z} \times \boldsymbol{r})/2\pi r^2. \tag{2.7}$$

The total magnetic flux through the wire cross-section is described by $\Phi = \eta\Phi_0$ with $\Phi_0 = h/e$ the flux quantum.

The spectrum of this Hamiltonian is

$$E_{kl} = \pm v_D \hbar \left(k^2 + \frac{\left(l + \frac{1}{2} - \eta\right)^2}{r^2} \right)^{\frac{1}{2}} \tag{2.8}$$

with $m = 0$ since the Zeeman coupling can safely be neglected [30, 31]. Here k is the momentum along the 1D wire in the z direction and $l = 0, \pm 1, \ldots$ is the quantum number for orbital angular momentum. For a more detailed derivation, see Refs. [30, 31].

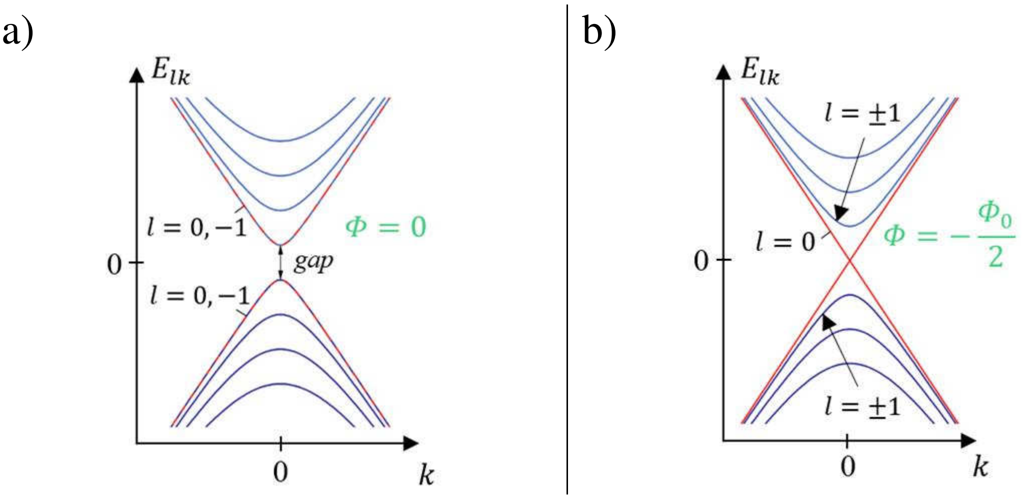

Figure 2.3: Plot of the spectrum without (a) and with (b) magnetic field along wire direction. Above is shown the corresponding band structure of the surface states. Without magnetic field the surface state spectrum has a band gap with a magnetic flux of $\Phi = -\Phi_0/2$ *the gap closes. Figure extracted from Ref. [32].*

The goal of the thesis is to prove that MBSs are present, which requires that the Fermi energy cuts an odd number of bands when superconductivity is proximity induced [29]. This is the case in the whole bulk gap when the wire cross section is pierced by a half-integer flux quantum and a single subband with gapless linear spectrum appears, as can be understood from equation (2.8) and seen in Figure 2.3.

2.1.2 3D topological insulator materials

The preceding descriptions are highly idealized for simplification. To obtain such a perfect 3D-TI in reality is quite difficult. An important challenge is to obtain the bulk insulation mentioned above. Otherwise, the special transport properties of the surface states are covered by the bulk transport and can only be identified with much difficulty in transport experiments.

The two TIs under consideration here, i.e., Bi_2Te_3 and Sb_2Te_3 are very similar in their crystal structure and both have a rhombohedral crystal structure with space group $R\bar{3}m$. The unit cell consists of three quintuple layers stacked on top of each other and held together by Van der Waals bonds. Figure 2.4 shows the crystal structure and the typical quintuple layers.

Both Bi_2Te_3 and Sb_2Te_3 have the problem of a relatively high background doping. Due to antisites with Te (Bi is substituted by Te) in the crystal, Bi_2Te_3 has an n-type doping [33-37]. Sb_2Te_3 is p-type doping [34, 35, 38, 39], which is caused by antisites, but in this case the Te is replaced by Sb.

Both materials can be grown using MBE and have nearly identical lattice constants. The idea is to combine the two materials to get the possibility to influence the doping. The material resulting from this idea is $(Bi_{1-x}Sb_x)_2Te_3$ [34]. By adjusting x it is now possible to directly influence the doping and thus the position of the Fermi level. With a concentration of $x = 0.49$ the Fermi level is above the Dirac point. If one increases the concentration to $x = 0.93$ the Fermi level will be at the Dirac point as desired. For pure Sb_2Te_3 so $x = 1$ the Fermi level is below the Dirac point [40]. These values for x and the corresponding position of the Fermi level can only be considered as basic guidelines.

Because differences between a flawless and oxidized surface can have a strong influence on the position of the Fermi level.

$(Bi_{1-x}Sb_x)_2Te_3$ is also used in the fabrication of the nanoribbons produced in this thesis. $(Bi_{1-x}Sb_x)_2Te_3$ can also be grown selectively with MBE on a [111] silicon surface that is partly covered with a hard mask. The exact process for this is described in the chapter 3 Fabrication process.

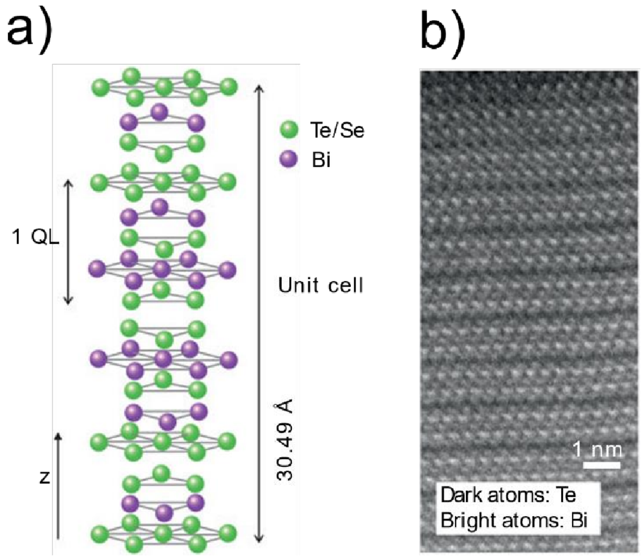

Figure 2.4: a) Crystal structure of the 3D-TI $(Bi_{1-x}Sb_x)_2Te_3$*. b) Transmission electron microscopy image of a* Bi_2Te_3 *layer. Figure adapted from Ref. [26].*

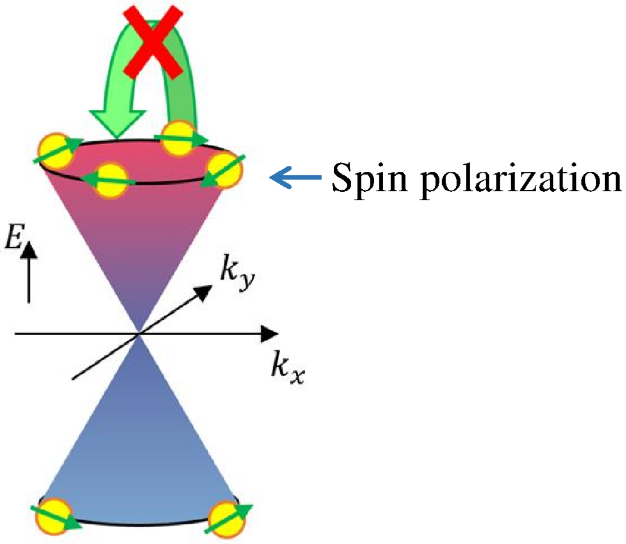

Figure 2.5: The dispersion relation of the surface states forming a 2D Dirac cone. Direct backscattering (big green arrow) is not possible. Figure extracted from Ref. [32].

2.2 Introduction to superconductivity

Superconductivity is a special state of matter in which the electrical resistance disappears below a characteristic critical temperature T_C and critical magnetic field H_C. It was first discovered by Kamerlingh Onnes [41, 42], whose work in the field of cryogenic cooling with the help of liquid helium made it possible to fall below the critical temperature T_C of mercury in 1911.

An important property of superconductors is the appearance of a macroscopic quantum state that describes a collective of electrons with a single wave function. The phenomenological Ginzburg-Landau theory was formulated to describe the macroscopic properties of superconductors [43]. In this section an introduction to superconductivity is presented with an overview of the most important properties. However, a microscopic understanding is only possible with the microscopic BCS theory [44] which is described in the next section.

Superconductivity is primarily known for the resistance-free conduction of electrical currents and for historical reasons has thus also been given the name with reference to this property. However, it is actually another physical effect of superconductors that describes their properties more fundamentally, namely their perfect diamagnetism also known as the Meissner-Ochsenfeld effect [45].

Superconductors are classified as Type I and Type II depending on their behavior in magnetic fields [46]. When a Type I superconductor is exposed to a magnetic field, shielding currents are induced which prevent the low magnetic flux from entering the superconductor due to the reverse polarity of the induced magnetic field. Only when a critical field strength H_C is exceeded, the superconductivity collapses and so do the shielding currents.

With Type II the behavior is more complex. Before the complete collapse of superconductivity, so-called flux tubes are created where the superconductivity has collapsed and magnetic flux enters the superconductor. Each of these flux tubes encloses a magnetic flux of $\Phi_0 = h/(2e)$ also known as flux quantum [47]. Above the first critical field H_{C_1}, flux tubes are created. If the field strength continues to increase, more and more flux tubes are formed until it reaches H_{C_2}, above which superconductivity disappears.

2.2.1 Microscopic description and Bogoliubov-de Gennes Hamiltonian

The mechanism causing superconductivity was unknown for a long time. With the BCS theory, named after its developers John Bardeen, Leon Neil Cooper and John Robert Schrieffer [44], a microscopic description of superconductivity was finally obtained (in 1957, almost 50 years after discovery of SC). The underlying idea is the existence of an attractive interaction between two electrons. This attractive interaction has its cause in the electron-phonon coupling [48, 49] and ensures that below the critical temperature T_C it is energetically favorable for the electrons to form so-called Cooper pairs. The Cooper pairs condense into a Bosen-like many-particle state at the Fermi energy E_F, into a so-called Bose condensate with a macroscopic (describing the whole condensate) wave function [46]. Cooper pairs consist of two electrons with opposite spin and momentum. This electron pair is coupled by a binding energy Δ. Another important property described by the BCS theory is that superconductors open a band gap with width equal to 2Δ. Within this band gap there are no states for charge transport through electrons or holes, charge is transported exclusively through the Cooper pairs, via a supercurrent with zero resistance.

The electrons and their electron-phonon-induced pairing interaction can be described using mean-field theory with the following Hamiltonian [50]

$$H = \sum_{\boldsymbol{k},s_1,s_2} \varepsilon_{s_1 s_2}(\boldsymbol{k}) c^{\dagger}_{\boldsymbol{k},s_1} c_{\boldsymbol{k},s_2} + \frac{1}{2} \sum_{\boldsymbol{k},s_1,s_2} \left[\Delta^{*}_{s_1 s_2}(\boldsymbol{k}) c_{\boldsymbol{k},s_1} c_{-\boldsymbol{k},s_2} + \Delta_{s_1 s_2}(\boldsymbol{k}) c^{\dagger}_{\boldsymbol{k},s_1} c^{\dagger}_{-\boldsymbol{k},s_2}\right] \quad (2.9)$$

using the annihilation and creation operators $c_{\boldsymbol{k},s}$,$c^{\dagger}_{\boldsymbol{k},s}$ for the electrons with momentum $\boldsymbol{k}$ and spin s. The first term consists of the energy operator $\varepsilon_{s_1 s_2}(\boldsymbol{k})$ and the number operator $c^{\dagger}_{\boldsymbol{k},s_1} c_{\boldsymbol{k},s_2}$ of the electrons. The second term describes the interaction of the electrons with the superconducting pair potential $\Delta^{*}_{s_1 s_2}(\boldsymbol{k})$. The pair potential $\Delta^{*}_{s_1 s_2}(\boldsymbol{k})$ can be written as

$$\Delta_{s_1 s_2}(\boldsymbol{k}) = - \sum_{\boldsymbol{k}',s_3,s_4} V_{s_1 s_2 s_3 s_4}(\boldsymbol{k},\boldsymbol{k}') \langle c_{\boldsymbol{k}',s_3} c_{-\boldsymbol{k}',s_4} \rangle . \quad (2.10)$$

Here $V_{s_1 s_2 s_3 s_4}(\boldsymbol{k},\boldsymbol{k}')$ describes the pair interaction. It is then common to write the Hamiltonian using a 4 × 4 matrix, resulting in the following form

$$H = \frac{1}{2}\sum_{\boldsymbol{k}} \begin{pmatrix} c^{\dagger}_{\boldsymbol{k},\uparrow} \\ c^{\dagger}_{\boldsymbol{k},\downarrow} \\ c_{-\boldsymbol{k},\uparrow} \\ c_{-\boldsymbol{k},\downarrow} \end{pmatrix}^{T} \underbrace{\begin{pmatrix} \varepsilon(\boldsymbol{k}) & \Delta(\boldsymbol{k}) \\ \Delta^{\dagger}(\boldsymbol{k}) & -\varepsilon(-\boldsymbol{k})^{T} \end{pmatrix}}_{\mathcal{H}_{4\times4}(\boldsymbol{k})} \begin{pmatrix} c_{-\boldsymbol{k},\uparrow} \\ c_{-\boldsymbol{k},\downarrow} \\ c^{\dagger}_{\boldsymbol{k},\uparrow} \\ c^{\dagger}_{\boldsymbol{k},\downarrow} \end{pmatrix} \tag{2.11}$$

with the following 2×2 matrices as subblocks $\varepsilon(\boldsymbol{k}) = \begin{pmatrix} \varepsilon_{\uparrow\uparrow}(\boldsymbol{k}) & \varepsilon_{\uparrow\downarrow}(\boldsymbol{k}) \\ \varepsilon_{\downarrow\uparrow}(\boldsymbol{k}) & \varepsilon_{\downarrow\downarrow}(\boldsymbol{k}) \end{pmatrix}$ and $\Delta(\boldsymbol{k}) = \begin{pmatrix} \Delta_{\uparrow\uparrow}(\boldsymbol{k}) & \Delta_{\uparrow\downarrow}(\boldsymbol{k}) \\ \Delta_{\downarrow\uparrow}(\boldsymbol{k}) & \Delta_{\downarrow\downarrow}(\boldsymbol{k}) \end{pmatrix}$.

The 4×4 matrix $\mathcal{H}_{4\times4}(\boldsymbol{k})$ used is called Bogoliubov-de Gennes Hamiltonian. Using the so-called Bogoliubov-de Gennes equation

$$\mathcal{H}_{4\times4}(\boldsymbol{k}) \begin{pmatrix} u_{\uparrow}(\boldsymbol{k}) \\ u_{\downarrow}(\boldsymbol{k}) \\ v^{*}_{\uparrow}(\boldsymbol{k}) \\ v^{*}_{\downarrow}(\boldsymbol{k}) \end{pmatrix} = E(k) \begin{pmatrix} u_{\uparrow}(\boldsymbol{k}) \\ u_{\downarrow}(\boldsymbol{k}) \\ v^{*}_{\uparrow}(\boldsymbol{k}) \\ v^{*}_{\downarrow}(\boldsymbol{k}) \end{pmatrix} \tag{2.12}$$

we can define Bogoliubov-de Gennes quasiparticles that represent hole-like and particle-like quasiparticles in the superconductor. It is then possible to determine the eigenenergies of these quasiparticles described by $\mathcal{H}_{4\times4}(\boldsymbol{k})$ by diagonalization. Eigenenergies $E_1(\boldsymbol{k}),\ E_2(\boldsymbol{k}), -E_1(-\boldsymbol{k}), -E_2(-\boldsymbol{k})$ are obtained. As mentioned above, the pairing potential $\Delta(\boldsymbol{k})$ couples particles (electrons) and holes. The solutions $E_i(\boldsymbol{k})$ $(i = 1, 2)$ are the eigenenergies of Bogoliubov-de Gennes quasiparticles and are a mixture (superposition) of particles (electrons) and holes. The solutions spectrum of these quasiparticles is also symmetric around $E = 0$ due to the particle-hole symmetry. It is also important to note that the Cooper pairs themselves are only described by the pairing potential $\Delta(\boldsymbol{k})$, which is proportional to the density of Cooper pairs, as can be seen from Equation (2.10), and are not included in the quasiparticle spectrum of the Bogoliubov-de Gennes Hamiltonian itself.

For $\varepsilon(\boldsymbol{k})$ the Bloch Hamiltonian of specific materials can be used, for example a free electron gas or the Hamiltonian of a 3D-TI. This will be relevant in the later chapter 4 to obtain the Hamiltonian of a topological superconductor.

2.2.2 Andreev reflection

Here I would like to briefly consider an important effect that occurs at NS interfaces. The first question that arises is what happens when an electron with an energy smaller than the superconducting band gap $\epsilon < \Delta$ hits the superconductor. For this question, Figure 2.6 is helpful in the schematic representation with $\epsilon = 0$ in the middle of the superconducting gap Δ. Within the superconducting band gap there are no individual electronic states (only the Cooper pair condensate at zero energy). The electron can only enter the superconductor when paired with another electron. In the case that a conduction band electron meets the superconductor, it pairs with an electron (with opposite spin) from the valence band. For the electron taken out of the valence band, a hole moves away from the superconductor with opposite momentum. In an alternative physical image, the incident electron is reflected as a moving hole (Figure 2.6(b)). In addition, a new Cooper pair has formed in the superconductor. The inverse process in relation to the previous description is also possible. Here, a hole with the energy $-\epsilon$ hits the superconductor (Figure 2.6(a)) and is reflected back as an electron, whereupon a Cooper pair is absorbed in the superconductor. The processes are known as Andreev reflection (Figure 2.6(b)) and reverse Andreev reflection (Figure 2.6(a)) [51].

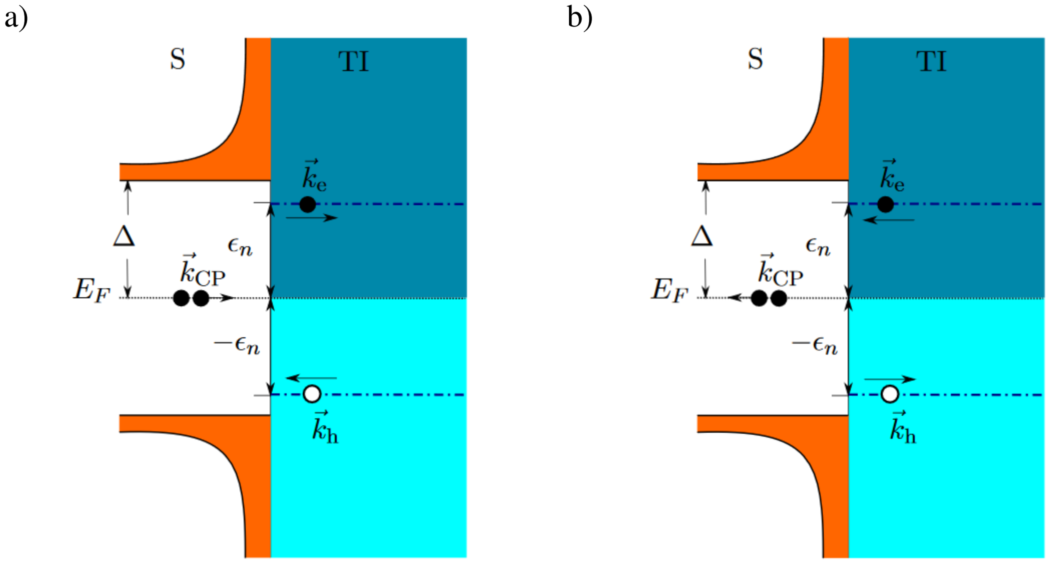

Figure 2.6: a) A hole is Andreev-reflected as an electron at the SN interface and a Cooper pair is "absorbed" from the superconductor. b) An electron is Andreev-reflected as a hole at the SN interface and a new Cooper pair is generated in the superconductor.

2.2.3 Proximity effect

In this thesis MBSs will be investigated. As already mentioned in the introduction, they can form in so-called p-wave superconductors. One way to get such a p-wave superconductor is to bring a TI into contact with an s-wave superconductor. The s-wave superconductor then induces superconductivity in the TI at the interface, which is called the proximity effect [52].

In this consideration we distinguish between the coherence length ξ_S and ξ_N in the superconductor and in the normal conductor. Cooper pairs have a typical extension proportional to their coherence length ξ_S. There are two limit case regimes for the description of the proximity effect at an SN interface the so-called *clean* and *dirty limits* [51, 53].

For the *clean limit* $l_{\mathrm{mean}} \gg \xi_N$ in this case the coherence length ξ_{N} is given by

$$\xi_N \approx \frac{\hbar v_{\mathrm{F}}}{2\pi k_{\mathrm{B}} T}. \tag{2.13}$$

with the mean free path of the electrons l_{mean}, the Fermi velocity v_{F} (Dirac velocity v_{D} if TI surface states are proximitized), temperature T and the Boltzmann constant k_{B}.

The reverse limit case is the *dirty limit* case, which in this case means that $l_{\mathrm{mean}} \ll \xi_N$. In this case the coherence length ξ_{N} is given by

$$\xi_{\mathrm{N}} \approx \left(\frac{\hbar D_{\mathrm{N}}}{2\pi k_{\mathrm{B}} T}\right)^{\frac{1}{2}}. \tag{2.14}$$

In this context, D_{N} is a material-dependent diffusion constant for the normal conductor. Considering the Cooper pair binding energy $\epsilon = 2\pi k_{\mathrm{B}} T$ [54] we can see that the coherence length decreases with increasing energy.

The proximity effect can also be understood by considering the reverse Andreev reflection process. If the hole absorbed by the superconductor is considered as reflected electron. In this image, a Cooper pair splits into two electrons when entering the normal conductor. Due to the different energies of the electron and consequently different wave vectors, the two electrons accumulate a phase difference [54]. If this phase difference exceeds $\delta\varphi = \pi$ the electrons are no longer correlated. The energy-dependent coherence length, which indicates from which penetration depth into the normal conductor the phase difference $\delta\varphi = \pi$ is exceeded, is $\mathrm{L}_{\varepsilon} = \sqrt{\hbar \mathrm{D}/\varepsilon}$. If the energy is at the position of the Fermi level $\varepsilon = E_{\mathrm{F}}$ the coherence length would go towards infinity in this case it is limited by the phase-breaking length L_{φ} [54] of the normal conducting region.

2.3 Majorana bound states

The Majorana bound state takes its name from the Italian physicist Ettore Majorana. In 1937, he reformulated the Dirac equations and found new solutions that described particles being their own antiparticles [6], which were named after him, i.e., Majorana fermions. A. Yu. Kitaev in 2001 predicted them as a quasi-particle version, so-called Majorana bound states (MBSs) or Majorana zero modes (MZMs), in condensed matter physics [55]. More specifically, for a one-dimensional (1D) p-wave superconductor.

Of particular interest in this thesis is that by combining the properties of TIs and superconductors, a topological p-wave superconductor can be realized [3, 56]. In these topological p-wave superconductor a special type of subgap-bound state exists which can occur at its boundaries or at topological defects such as vortices or domain walls.

These states occur at zero energy and the second quantization operators that describe these states are self-conjugated $\gamma_i^{\dagger} = \gamma_i$ and $\gamma_i{}^2$ =1. Thus they share the particle-equal-antiparticle property of the famous Majorana fermion [57]. It is important not to consider γ_i as a particle operator because in the context shown here occupied or unoccupied makes no sense for γ_i. Rather γ and the corresponding MBS should be considered as an exotic quasi-particle excitation representing one half of a fermionic state. More precisely, a couple of MBSs γ_1 and γ_2 can be combined to a regular fermionic state $f = (\gamma_1 - \gamma_2)/\sqrt{2}$ for which a number operator is well defined. The MBSs γ_1 and γ_2 resulting from its combination f can theoretically be located arbitrarily far away from each other. So f has a strong non local character although f is a normal fermion operator, which satisfies the canonical anticommutation relations. Furthermore the state represented by f can be filled or emptied without the need of energy. This results in a degeneracy of the ground-state energy when multiple MBS pairs are present in the system [58]. The individual MBSs can be moved around (each other) and display peculiar exchange statistics, namely non-abelian statistics. The exotic quasi-particle excitation that MBSs represent are therefore anyons and not fermions.

This quantum statistical property makes MBSs a promising platform for fault-tolerant quantum computing. The quantum information of the fermionic state is encoded in pairs of MBSs γ_1 and γ_2 that can be spatially separated, which protects the information against local disorder or noise. Together with the anyon statistics that allow the manipulation of the quantum state or information via braiding, this makes MBSs highly interesting for the realization of fault-tolerant quantum computation [4, 5].

However, an important step towards a quantum computer based on MBSs is first of all to demonstrate their appearance and robustness. In this thesis I try to do just that by tunnel spectroscopic investigations on a superconducting proximitized 3D-TI nanoribbon.

2.4 Tunneling spectroscopy

To detect MBS at the end of a nanowire or nanoribbon, tunnel spectroscopy can be used. This is a method in which a tunnel conductance is measured between a normal conductor, a tunnel barrier, and a superconductor. Since the tunnel conductance measured is proportional to the local density of states behind the tunnel barrier, a MBS can be detected. The MBS allows resonant Andreev reflection over the tunnel barrier and thus is expected to show up as a conductance peak quantized to $2G_0$ at ZBP at very low temperatures. For elevated temperatures the height of the peak is reduced. Experiments based on this method have already been successfully performed [7, 11-15].

For the derivation of the tunnel conductance we start with the Landauer-Büttiker formalism in which we consider the current through the normal conductor/contact as the sum of three different contributions

$$
\begin{aligned}
I^{(\mathrm{e})} &= -\frac{e}{h}\int \mathrm{d}E\, f(E+eV_{\mathrm{bias}})[N(E,V_{\mathrm{bias}})-R_{\mathrm{ee}}(E,V_{\mathrm{bias}})],\\
I^{(\mathrm{h})} &= \frac{e}{h}\int \mathrm{d}E\, f(E-eV_{\mathrm{bias}})R_{\mathrm{eh}}(E,V_{\mathrm{bias}})\\
&= \frac{e}{h}\int \mathrm{d}E\, [1-f(E+eV_{\mathrm{bias}})]R_{\mathrm{he}}(E,V_{\mathrm{bias}}),\\
I^{(\mathrm{sc})} &= -\frac{e}{h}\int \mathrm{d}E\, f(E)T_{\mathrm{es}}(E,V_{\mathrm{bias}}),
\end{aligned}
\tag{2.15}
$$

where $I^{(\mathrm{e})}$ and $I^{(\mathrm{h})}$ are the electron and hole currents going into the superconductor. The chemical potential is set to zero as reference point for the bias voltage (this does not mean that chemical potential is at the Dirac point energy). $I^{(\mathrm{sc})}$ is the quasiparticle current through the superconductor and f is the Fermi distribution. N is the number of electron modes in the normal conductor contact, R_{ee} is the electron reflection amplitude, R_{eh} is the Andreev reflection amplitude and T_{es} is the transmission amplitude of modes above the superconductor gap [59].

The total current then adds up to the well-known BTK (Blonder-Tinkham-Klapwijk) formula

$$
\begin{aligned}
I = \frac{e}{h}\int \mathrm{d}E\, [f(E)-f(E+eV_{\mathrm{bias}})][&N(E,V_{\mathrm{bias}})-R_{\mathrm{ee}}(E,V_{\mathrm{bias}})\\
&+R_{\mathrm{he}}(E,V_{\mathrm{bias}})].
\end{aligned}
\tag{2.16}
$$

The differential conductance hat is relevant for comparison with the results of the experiment is then

$$
\begin{aligned}
G = \frac{\mathrm{d}I}{\mathrm{d}V_{\mathrm{bias}}} = \frac{e^2}{h}\big(&N(-eV_{\mathrm{bias}},V_{\mathrm{bias}})-R_{ee}(-eV_{\mathrm{bias}},V_{\mathrm{bias}})\\
&+R_{\mathrm{he}}(-eV_{\mathrm{bias}},V_{\mathrm{bias}})\big)\\
&-\frac{e}{h}\int_0^{-eV_{\mathrm{bias}}} \mathrm{d}E\left[\frac{\partial R_{\mathrm{he}}(E,V_{\mathrm{bias}})}{\partial V}-\frac{\partial R_{\mathrm{ee}}(E,V_{\mathrm{bias}})}{\partial V}\right]
\end{aligned}
\tag{2.17}
$$

in the limit case for T towards 0. In the linear response limit, the integral can be neglected [59] thus resulting in

$$\begin{aligned} G = \frac{\mathrm{d}I}{\mathrm{d}V_{\mathrm{bias}}} = \frac{e^2}{h}\big(&N(-eV_{\mathrm{bias}}, V_{\mathrm{bias}}) - R_{ee}(-eV_{\mathrm{bias}}, V_{\mathrm{bias}}) \\ &+ R_{\mathrm{he}}(-eV_{\mathrm{bias}}, V_{\mathrm{bias}})\big). \end{aligned} \tag{2.18}$$

It must be considered that $R_{eh} \sim \rho_{ABS}$ and $(N - R_{ee}) \sim \rho_q$ with ρ_{ABS} being the density of Andreev bound states and ρ_q being the quasi-particle density of states. Together it is possible that with the differential conductance $\mathrm{d}I/\mathrm{d}V$ the ρ_{ABS} in the gap and ρ_q are resolved. A quantized ZBP can be created with the presence of a MBS, since resonant tunneling with perfect probability for Andreev reflection via the MBS is possible.

3 Fabrication process

In the previous chapter, it was explained theoretically which requirements our device has to meet. This section explains how these can be implemented in a real device. Problems that arose during fabrication and approaches to solving them are also discussed.

The underlying motivation for the tunnel junction is the detection of so-called MBS, a quasiparticle state which was explained in more detail in the section 2.3. Signatures of MBS have already been found in III-V semiconductor based tunnel junctions. However, the tunnel junction shown in Figure 3.1 uses a 3D-TI instead of a semiconductor.

Since TIs are sensitive to surface degradation (described in more detail in Section 3.1), they posed numerous challenges to the manufacturing process, including in-situ fabrication, alignment, mask removal, and selective area growth (SAG). However, this effort should be worthwhile as 3D-TIs should provide an energetically much wider topological gap compared to III-V semiconductors [60].

As shown in Figure 3.1, the tunnel junction consists of different components, which are produced in different manufacturing steps. From the previous theory chapter we know that we need a 3D-TI nanoribbon (blue), superconducting contacts (top, red), normally conducting contacts (sides, turquoise) and a tunnel barrier (between TI and N). With the choice of the materials and geometries used for these parts, there are numerous possible variations. However, the basic structure of a tunnel junction always corresponds to the schematic representation shown in Figure 3.1.

A major problem is the need for a tunnel barrier because the TI cannot be depleted via a gate. This is prevented by the topological nature of the material itself, A tunnel barrier must therefore be physically created by introducing a dielectric. Unlike the tunnel barrier created by the gate in semiconductors, the thickness of the tunnel barrier created by a dielectric is not tunable after fabrication.

It is crucial that the quality of the TI superconductor interface is guaranteed. For this purpose all process steps after growth of the TI until the TI is protected by a capping are carried out *in situ*. The process allows the TI surface to be protected against degradation. This is enabled by the stencil lithography process and selective area growth of TI presented in Ref. [10]. A more detailed explanation of the individual process steps follows in the sections of this chapter. At this point I would like to thank Michael Schleenvoigt, who performed the growth described in section 3.3.

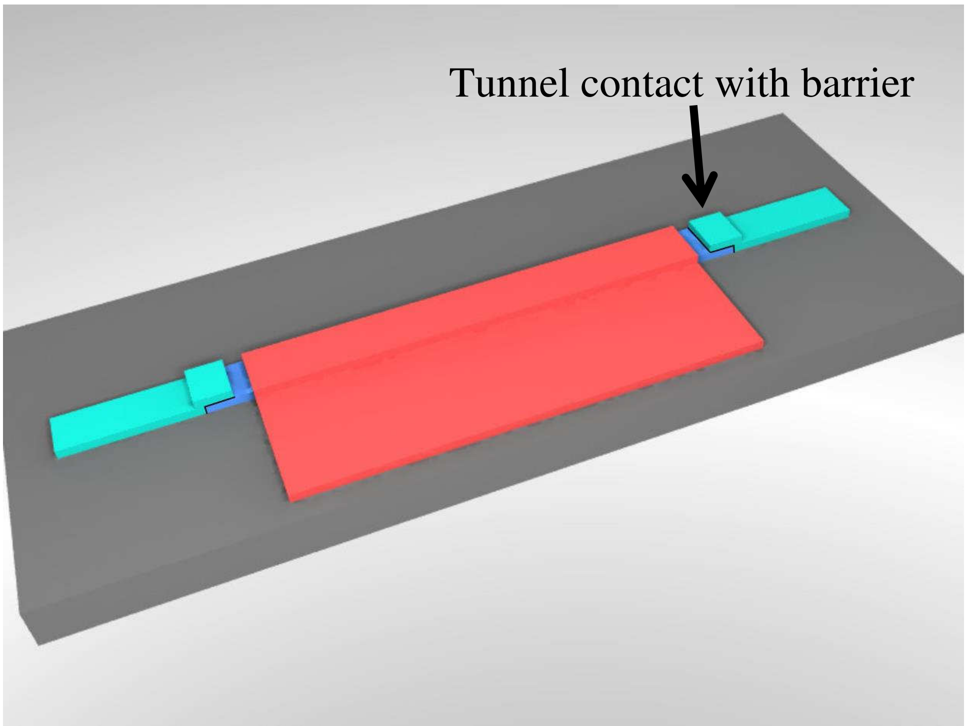

Figure 3.1: Three-dimensional schematic representation of the TI tunnel junction. The TI is dark blue, the normal conductor is shown in turquoise, the superconductor in red and the substrate in grey. The position of the tunnel barrier is marked by a black line. The shadow mask is not shown for simplification.

3.1 Surface degradation

It has already been emphasized that the motivation behind the choice of an *in situ* manufacturing process is the surface degradation of the TI. In the following, this process will be briefly described. The peculiarity of TIs are their protected surface states. However, these surface states can be protected by suitable passivation layers on the surface of the TI by other states.

Oxidation on the surface [18, 19] of the (Bi,Sb)-based TI lead to the formation of nontopological states. A similar effect has been proven for the exposure to water vapor [61]. Contact with water induces a chemical reaction at the surface. This causes a band bending which shifts the Dirac point deep into the occupied states and thus creates quantum well states with Rashba-type splitting on the surface. These states coexist with the topological states. This finding is based on angle-resolved photoemission spectroscopy (ARPES) measurements. In addition, the reaction causes an n-type doping of the TI.

To prevent surface degradation, an Al_2O_3 passivation is often used. Signatures in SdH (Shubnikov-de-Haas) oscillations and WAL (weak anti-localization) effects due to topological surface states could be better resolved by applying an *in situ* passivation with Al_2O_3 by MBE [62]. An Al_2O_3 passivation also appears to lower the carrier concentration [63].

Surface degradation is the central motivation for the *in situ* fabrication of the tunnel junction. In the following sections I will explain how to fabricate the stack of SiO_2 and Si_3N_4 layers necessary for stencil lithography and selective area epitaxy. How these layers are then used to define masks needed for *in situ* patterning during growth and deposition processes in the MBE chamber.

3.2 Fabrication of a selective area epitaxy mask and a mask for stencil lithography

The process described here combines the possibilities of selective area epitaxy. As well as the production of masks for stencil lithography of different materials. The process shown in the following is largely based on the work of D. Rosenbach [64], T. Schmitt [65] and P. Schüffegen [10, 32] on *in situ* structuring of superconductors with stencil lithography. The new technique developed in this thesis is to deposit two different metals at two different positions using a single mask for stencil lithography. This makes it possible to contact the tunnel junction *in situ* with a superconductor and a normal conductor.

3.2.1 Substrate fabrication

The substrate produced by the process described in this section was provided by Tobias Schmitt. In order to describe the complete fabrication of the tunnel junction, the individual steps required to fabricate the substrate are also described in detail here. This substrate allows for selective growth, i.e. it defines the areas where the TI will grow later selectively. Figure 3.2 shows the cross section of the substrate after its individual process steps.

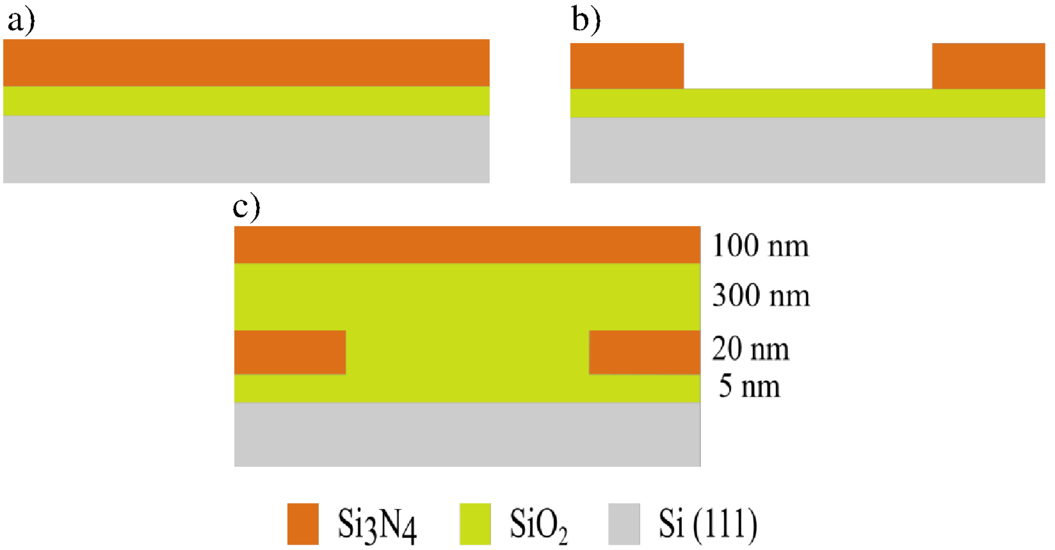

Figure 3.2: Cross-section of the substrate according to selected process steps. a) The Si substrate with the first SiO_2 and Si_3N_4 layers. b) After etching of nanotrenches in the Si_3N_4 layer for selective growth. c) After applying SiO_2 and Si_3N_4 for the shadow mask.

The process starts with a Si(111) wafer. The surface of the wafer is exposed to a cleaning process to ensure subsequent growth of the TI on the Si(111) surface of the wafer. The following cleaning process is applied; first, the wafer is bathed in piranha solution (mixture of 96% sulfuric acid (H_2SO_4), and 31% hydrogen peroxide (H_2O_2) in a ratio of 2:1) for 10 min. Subsequently, it is rinsed in DI (Deionized) water for 10 min. This is followed by etching with 1% HF (hydrofluoric acid) solution for 10 min and again rinsed in DI water for 10 min.

With thermal oxidation, a 5 nm thick SiO_2 layer is applied to the Si(111) wafer surface cleaned in the previous step. On this SiO_2 layer a 20 nm thick Si_3N_4 layer is applied. The result of these two steps is shown in Figure 3.2(a). The Si_3N_4 layer is deposited with low pressure chemical LPCVD (low pressure chemical vapour deposition), which allows sufficient etch selectivity between the SiO_2 and the Si_3N_4 layer for etching with 1% HF solution. On this Si_3N_4 layer it is now possible to define the nanotrenches for the subsequent selective area growth of the TI using an EBL (electron beam lithography) process and RIE (reactive ion etching). The result is shown in Figure 3.2(b).

However, this layer stack has so far only allowed selective growth of the TI. The stencil lithography mask is still missing, which allows the *in situ* production of the contacts. For this purpose the layer stack is extended by two additional layers which are added after etching the trenches into the 20 nm thick Si_3N_4. These layers are another SiO_2 layer with a thickness of 300 nm and a 100 nm thick Si_3N_4 layer. Both layers are generated with LPCVD. The result is shown in Figure 3.2(c). The substrate for the growth of nanoribbons and the fabrication of a mask for stencil lithography is now ready.

3.2.2 Electron-beam lithography and reactive-ion etching

This section describes how the geometry of the mask for stencil lithography is defined by an EBL process and RIE (reactive-ion etching) of the top Si_3N_4 layer. In the previous section 3.2.1, the structuring of a Si_3N_4 layer was already required for the selective area epitaxy mask. The procedure used is identical to the one described here, except for a possible variation of the etch time of the RIE.

The process starts with the application of a resist suitable for nanostructures and EBL (electron-beam lithography) processes. For the nanostructures in this work, the spinning of AR-P 6200.09 (Allresist GmbH) was chosen. Before spin coating, the sample is cleaned by bathing in acetone, IPA (isopropanol) and DI water for 5 min each (order: acetone, IPA, DI). After blowing off with nitrogen, the sample is placed on a 100 °C hotplate for 5 min to remove any remaining water.

After this cleaning, the resist is spin coated for 45 s at a speed of 6000 s^{-1} and an acceleration of 4000 s^{-2}. After the spin coating, a so-called softbake is performed and residual solvents are evaporated. For this purpose, the sample is placed on a 150 °C hot heating plate for 1 min.

The resist layer applied in this way can now be structured by an electron beam. To develop the resist, the sample is immersed for 1 min in AR 600-546 (Allresist GmbH) at 0 °C. The developer is then removed by bathing twice in IPA for 30 s each. IPA is prepared in two separate beakers for this purpose. To remove IPA residues, the sample is briefly immersed in DI water again and can then be blown off with nitrogen.

It is now possible to etch structures in the Si_3N_4 layer. Reactive-ion etching (RIE) is used because it has a very good anisotropy of the etch direction. The individual steps for the resist processes are listed in Table 3.1. The exact process parameters for RIE process can be found in Table 3.2 and EBL parameters in Table 3.3. A SEM image of the stencil after RIE is shown in Figure 3.4.

After the RIE, the resist must be removed. For this purpose, the sample is submerged with ultrasound in the resist remover AR 600-71 for 10 min. To take off the resist remover, the sample is bathed in IPA for 5 min. It is then blown dry with nitrogen. To remove any remaining resist, an oxygen plasma ashing process is performed with a power of 600 W and a gas flow of 600 sccm for 5 min.

The result of this step can be seen in Figure 3.3 and Figure 3.4. Indirectly, the geometries of both metals, namely the superconducting and normal conducting electrodes, are also defined by the shadow cast by the mask in the later MBE process.

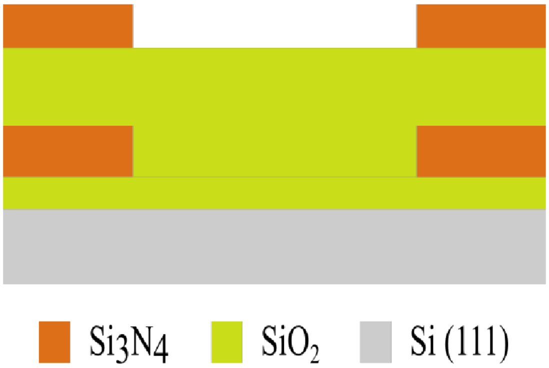

Figure 3.3: Result of the EBL and RIE process to define a mask for stencil lithography.

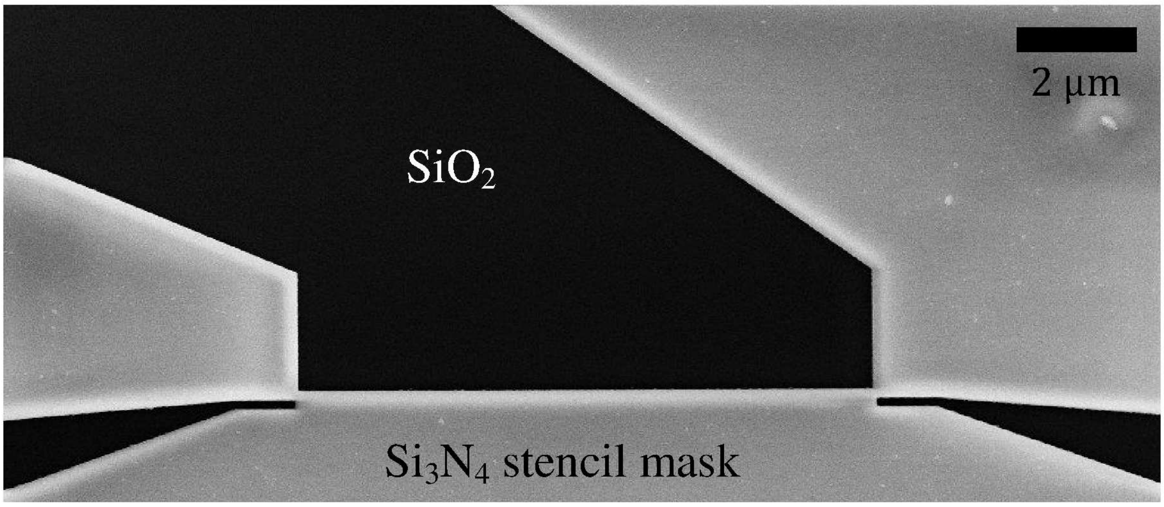

Figure 3.4: SEM image of the stencil hard mask of Si_3N_4 (gray) after the RIE etching and cleaning, the trench for selective growth is here covered by SiO_2 (black) and therefore not visible.

The sample must be cleaned before growth. The piranha solution cleaning method mentioned above is used for this. This means the sample is placed in piranha solution for 10 min and then in DI water for 10 min.

This is followed by an underetching step in which all SiO_2 up to the nanotrench is removed. This is combined with the creation of the hydrogen passivation of the Si(111) layer immediately before growth in the MBE chamber. This results in a total etching time of 18.5 min in 1% HF solution. The substrate now has the appearance shown in Figure 3.5, Figure 3.6 and Figure 3.7 with the hydrogen passivated Si(111) surface in the nanotrench. The next steps for the sample are explained in section 3.3.1 on MBE growth of the TI.

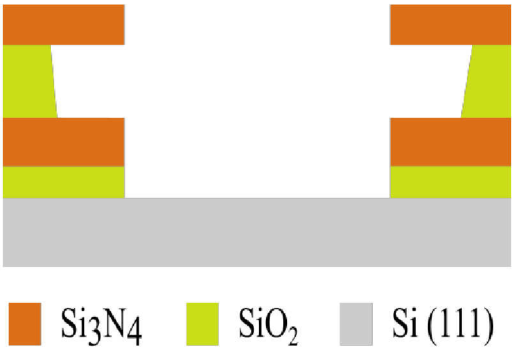

Figure 3.5: a) Sample after underetching of the shadow mask including removing the 5 nm SiO_2 protective layer.

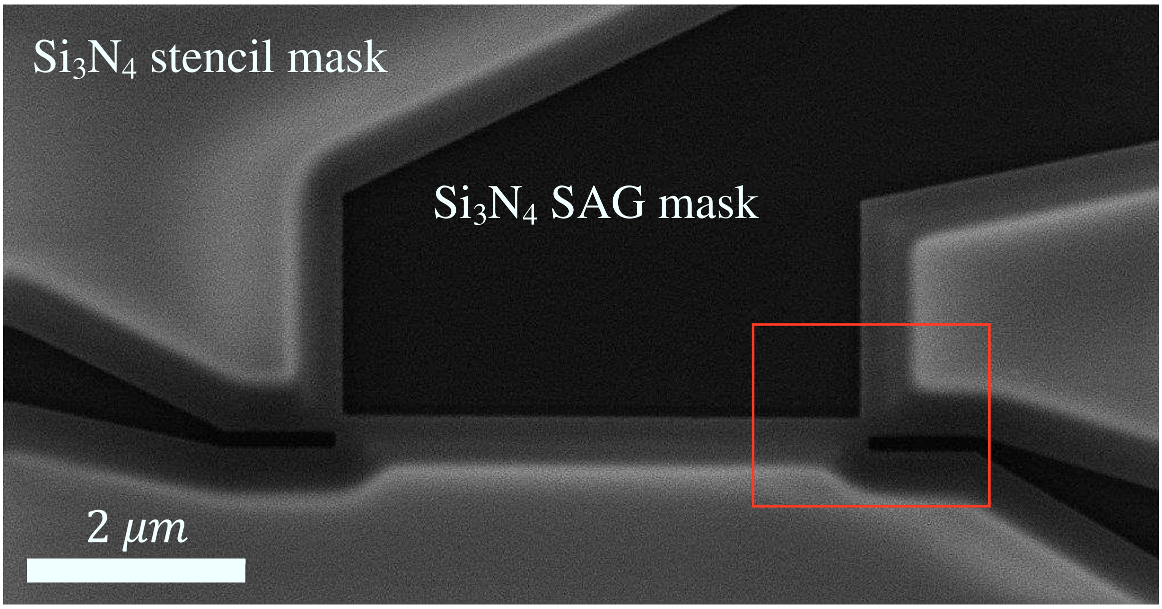

Figure 3.6: SEM image of the hard mask for the production of the tunnel junction which was underetched with 1% HF solution. A zoom-in of the region in the red box is shown in Figure 3.7.

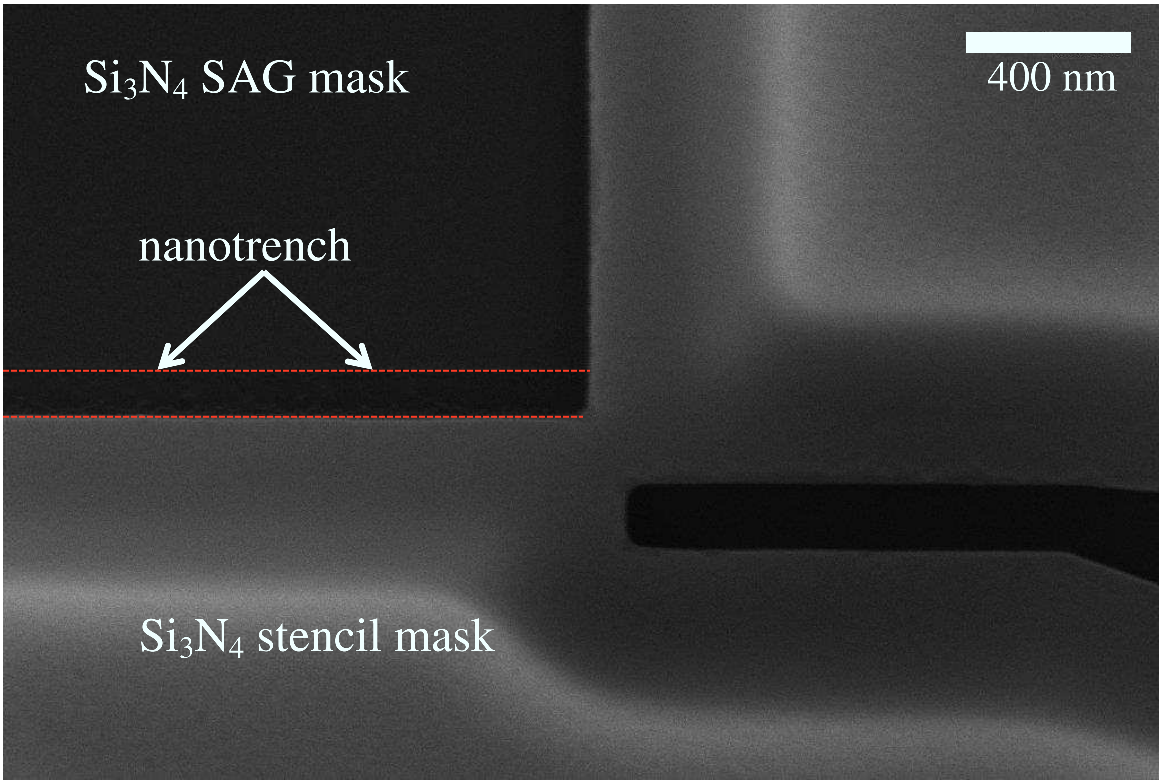

Figure 3.7: A closer section of the hard mask shown in Figure 3.6 (red box) here shows the area for the deposition of the superconductor (Nb) on the left. The nanotrench for selective growth can also be seen within this range. The area for the normal conductor can be seen on the right-hand side.

Process steps	
Cleaning	5 min aceton 5 min IPA 5 min DI water
Dehydration	5 min @ 100°C
resist	AR-P 6200.09
Spin coating	6000 min^{-1}, 4000 s^{-2}, 45 s
Softbake	1 min @ 150°C
EBL process (Table 3.3)	
Development	60 s @ AR 600-546 (0°C)
Development stop	2 x 30 s IPA
RIE process (Table 3.2)	
Resist removal	10 min AR 600-71 5 min aceton 5 min IPA
Oxygen plasma cleaning	5 min, 600 W, 600 sccm without Faraday cup

Table 3.1: Resist processes for in situ tunnel junction. The basis is the process described in Ref. [65]. Different process parameters were adapted to enable EBL with 100 kV *acceleration voltage.*

Process steps		
Machina HNF		RIE 5
RIE process		Etching the Si_3N_4 hard mask
etching	Gas / flow [sccm]	CHF_3 / 55 + O_2 /5
	rf power [W]	25
	ICP power [W]	100
	Time [min]	3
cleaning	Gas / flow [sccm]	Ar / 100 + O_2 / 50
	rf power [W]	50
	ICP power [W]	1800
	Time [min]	10

Table 3.2: RIE processes for in situ tunnel junction. The RIE process was developed by Tobias Schmitt [65] and is listed here again for completeness and reproducibility.

equipment	RAITH EBPG5200	
EBL parameter	**fine**	**coarse**
acceleration voltage [kV]	100	100
step size [nm]	2	20
dose [μC/cm^2]	4x140	4x140
write current	500 pA	40 nA
defocus	no	no
high resolution mode	no	no
proximity correction	on	on
multi- path	on	on

Table 3.3: EBL parameters to write the mask layout for in situ tunnel junction.

3.3 Ultra-high vacuum lithography

3.3.1 Selective area epitaxy of the topological insulator

Selective surface growth is based on the use of different material surfaces that have different sticking coefficients due to the chemical properties of the surfaces. As a result, the material to be grown has different growth temperature windows for nucleation on the different surfaces.

In previous studies it was found that selective growth of (Bi,Sb)-based TIs is possible [66, 67]. A mask of SiO_2 and Si_3N_4 can be produced on a Si(111) substrate [10]. This will result in a desired TI film growth on an Si(111) surfaces, whereas with suitable growth parameters, no nucleation of TI takes place on the SiO_2 and Si_3N_4 surfaces. The different growth temperatures of TI on the surfaces of SiO_2 and Si_3N_4 compared to the Si(111)-surfaces are simply due to the fact that SiO_2 and Si_3N_4 have an amorphous surface.

It’s challenging to find the right temperature to determine the temperature window in which the desired film growth occurs on the Si(111) surface. Also a careful cleaning of the substrate before growth is of great importance because even the slightest contamination can strongly influence growth.

In order to contact the structures grown with the selective area epitaxy mask *in situ*, a mask for stencil lithography will be integrated on the chip before growth, too. The fabrications of the selective area epitaxy mask and the mask for stencil lithography have been explained in detail in the previous sections. In the following, the TI growth in the MBE chamber will be described.

The samples are placed in the MBE chamber as soon as possible after the underetching described at the end of section 3.2.2. Because hydrogen passivation is not maintained for a long period of time, in order to protect the Si(111) surface from exposure to normal ambient air. After introducing the sample into the growth chamber, it is heated up to 700 °C for 20 min to remove the hydrogen passivation layer. During this time the effusion cells are heated to the temperatures required for growth. The shutters in front of the effusion cells are closed during this time. During the actual growth, the sample is rotated at 10 rpm and adjusted to a temperature that allows for selective growth. This SAG temperature window is relatively small, so that a precise setting of the sample temperature has a strong influence on the selectivity. A substrate temperature of 220 °C was chosen for the growth of the $(Bi_{1-x}Sb_x)_2Te_3$ nanoribbon. The temperatures of the effusion cells for the TI growth can be found in Table 3.4. The device can be seen in Figure 3.8 after successful growth of the TI (indicated in blue) in the nanotrench.

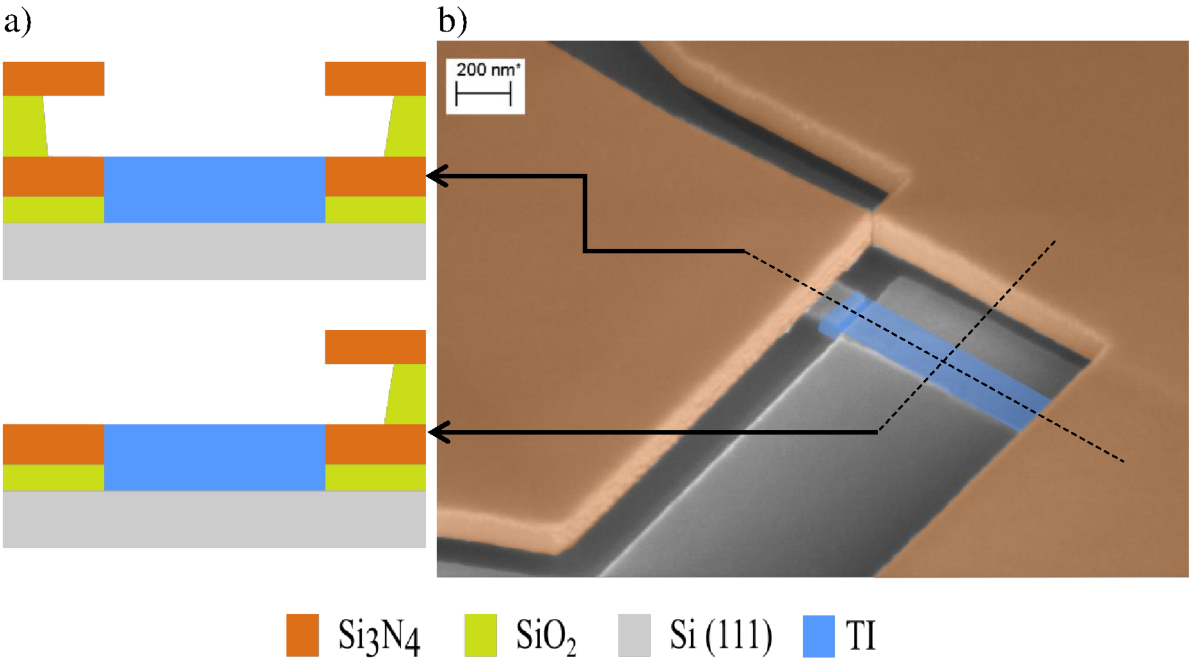

Figure 3.8: a) Schematic cross-section of the sample along the individual dotted lines in (b). b) Colorized SEM image of the sample after growth of TI.

	T_{Bi}	T_{Sb}	T_{Te}
Effusion cells main	460 °C	410 °C	380 °C
Tip	600 °C	--	--
Valve	--	440 °C	500 °C
Cracker	--	1000 °C	1000 °C

Table 3.4: Temperatures for the MBE growth of $(Bi_{0.6}Sb_{1-0.94})_2Te_3$.

3.3.2 Manufacturing of metal contacts and tunnel barrier via stencil lithography

The metal contacts are evaporated in the metal MBE chamber of the HNF nanocluster. Since the two separate MBE chambers for TI growth and deposition of the metal contacts are connected by a UHV transfer system, the sample can be transferred *in situ*. At the beginning of this work no MBE chamber for TI growth was connected to the UHV transfer system. At that time, the TI had to be grown in a completely separate MBE chamber. This required the use of a vacuum suitcase to transfer the sample into the MBE chamber for deposition of the metal contacts. One of the disadvantages of such a vacuum suitcase is the time required for the transfer compared to the UHV transfer system.

In the metal MBE chamber, the superconducting contact can now be applied using EBPVD (electron-beam physical vapor deposition). For this purpose the sample is rotated to the electron beam evaporator so that deposition from the direction shown in Figure 3.9 occurs. As the molecular beam arrives at an azimuth angle of 32.5°, a shadow is cast through the mask.

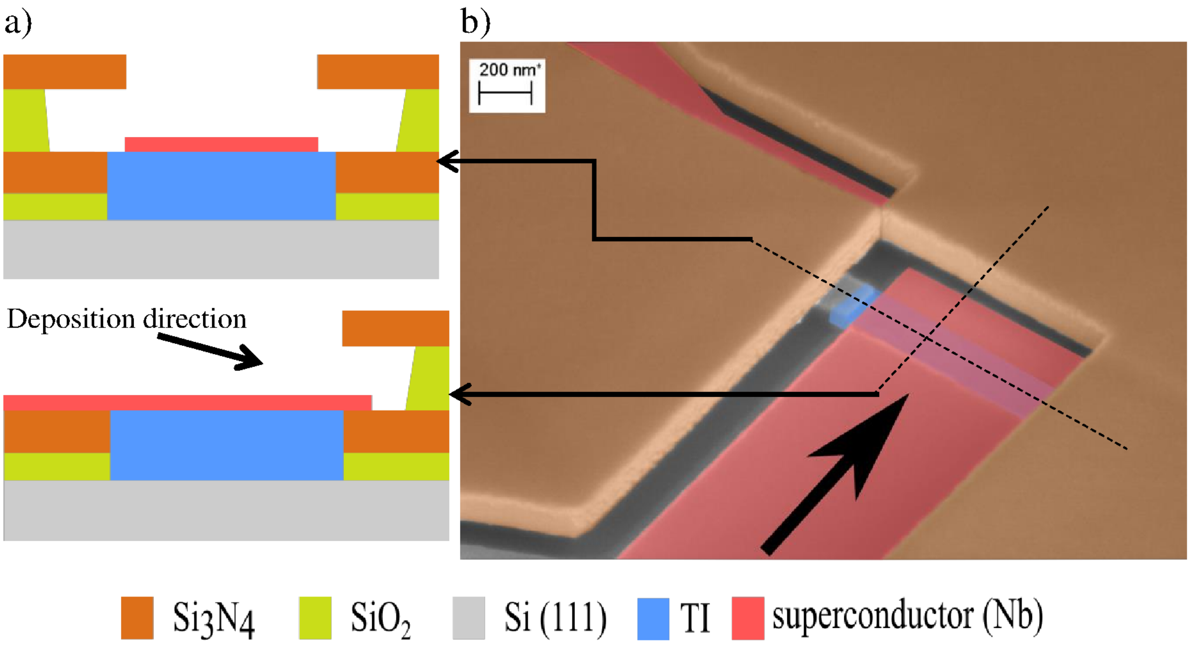

Figure 3.9: a) Schematic cross-section of the sample along the individual dotted lines in (b). b) Colorized SEM image of the sample with superconductor (Nb) deposited from the direction of the black arrow.

Via EBPVD a layer of Al_2O_3 is applied as dielectric for the tunnel barrier while the substrate is rotated to achieve a uniform Al_2O_3 coverage. The target thickness for the tunnel barrier at the contact is between 1 nm to 3 nm, taking into account that shading effects from the mask can also have a strong influence on the deposition rate, see section 3.5.

The normal-conducting contacts are applied according to the same principle as the superconductor, with the exception that by rotating the sample the molecular beam comes from the opposite direction. This results in a shadow cast corresponding to the mask. The shadow should be placed at the end of the TI separation. This process is shown in Figure 3.10.

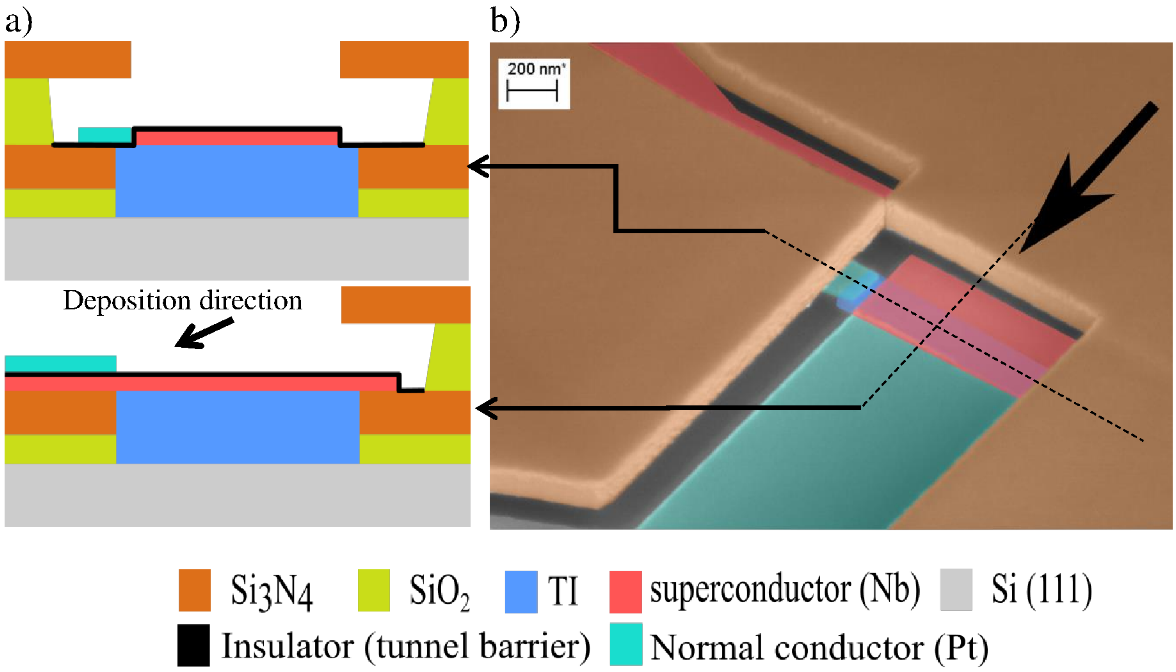

Figure 3.10: a) Schematic cross-section of the sample along the individual dotted lines in (b). b) Colorized SEM image of the sample with normal conductor (Pt) deposited from the direction of the black arrow.

As a last growth step an Al_2O_3 layer is applied as a capping to protect the tunnel junction from air and other influences. The MBE growth parameters for the Al_2O_3 and the metal contacts are listed in Table 3.5.

Material	**$T_{substrat}$**	**$R_{deposition}$**	**d**	**rotation**
Nb	50 °C	0.19 nm/s	30 nm	no
Al_2O_3	50 °C	0.07 nm/s	2.5 nm	20 rpm
Pt	50 °C	0.01 nm/s	30 nm	no
Al_2O_3	50 °C	1.07 nm/s	5 nm	20 rpm

Table 3.5: MBE parameters for the growth of metal contacts and Al_2O_3. The indicated thicknesses d are only given as an example and have been adjusted depending on the sample.

3.4 Stencil mask optimization

The first completed samples showed some problems. These were solved by optimizing the layout for the mask.

In the first samples the alignment of the normal conducting contacts were not optimally aligned to the end of the TI ribbons. The alignment of the normal conducting contacts could be further optimized in both horizontal and vertical direction.

As shown in Figure 3.11, the generated bridge between the areas of normal and superconducting contact of the mask is too narrow and therefore too unstable. Even slight mechanical stresses in the mask are sufficient to cause the bridge to tear and thus damage the mask. It is therefore necessary to increase the width of this bridge. However, increasing the width of the bridge may directly conflict with the alignment of the normal conducting contact. Also, shortening the superconducting contact in the horizontal direction to increase the width of the bridge must be done with care to avoid oversizing the ends of the TI ribbon that are not covered by the superconductor.

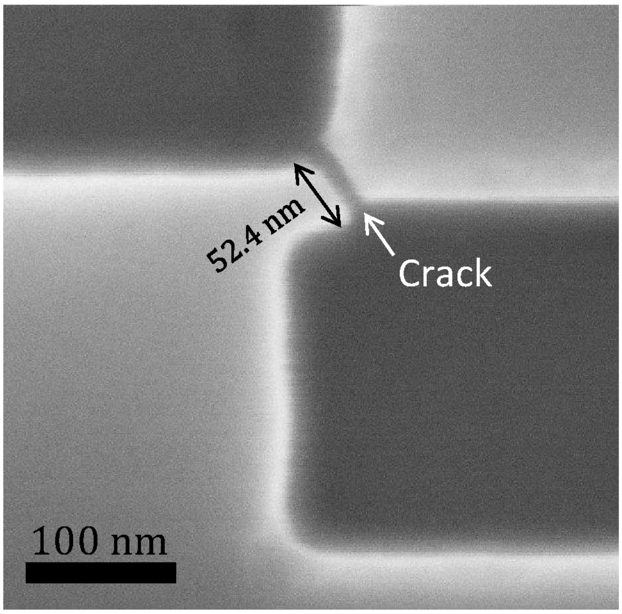

Figure 3.11: Broken Si_3N_4 stencil mask bridge between the regions of the normal conductor and the superconductor due to stresses in the mask.

Both problems can be solved by optimizing the layout geometry. Therefore a dose test tailored to the tunnel junction was performed. This test was necessary anyway because the electron beam system used for lithography was upgraded from an acceleration voltage of 50 kV to 100 kV. This required a re-determination of the dose used for the EBL process.

The layout for the dose test was created using the Klayout [68] Python (programming language) package and a self-written Python script. This allowed the layout to be defined in a program script that automatically generates the individual structures for the dose test. In this way many structures with different distances to the trench end could be investigated without further design effort. Figure 3.12 shows the dose test sample before underetching and Figure 3.13 after underetching with 1% HF solution.

Figure 3.12: Structures of the dose test after RIE etching.

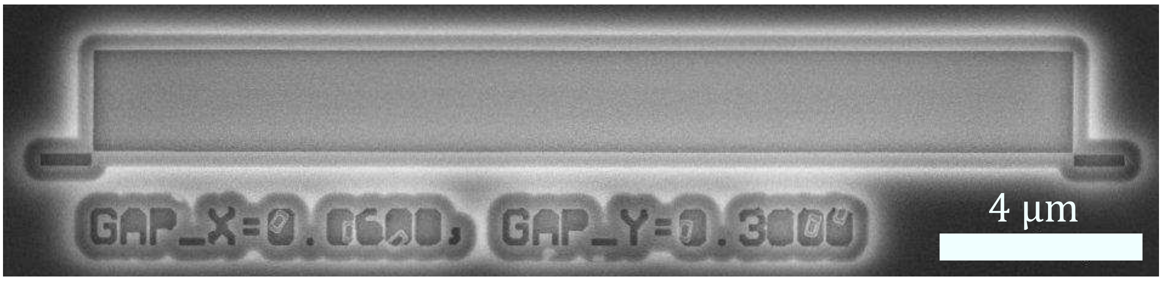

Figure 3.13: Structures of the dose test after 1% HF solution underetching.

After RIE etching and underetching of the mask with 1% HF solution, this allowed to determine the optimal spacing for bridge and alignment in combination with the dose to be used for the EBL process.

In Figure 3.14 and Figure 3.15 the results of the optimizations are shown, as well as the bridges that are intact and the improved alignment compared to the first version of the layout.

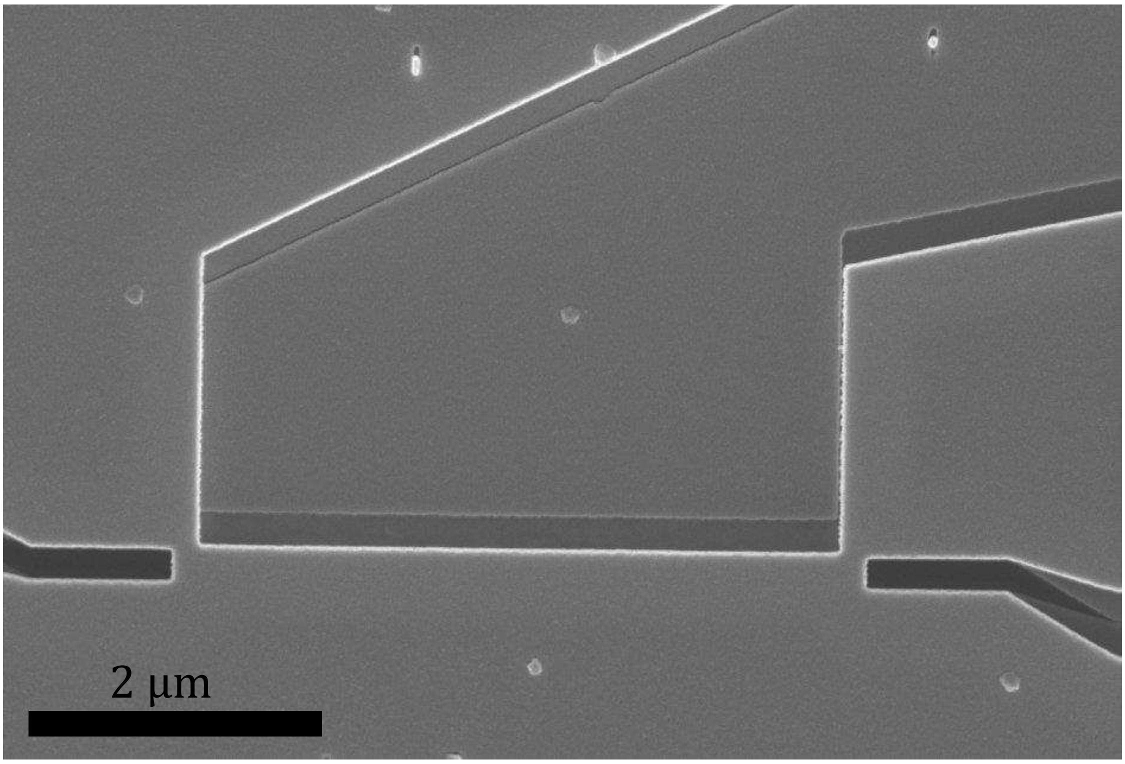

Figure 3.14: SEM image of the tunnel junction after MBE growth. The image shows the stencil mask layout used for tunnel junction with two normal conductors and one superconductor contact.

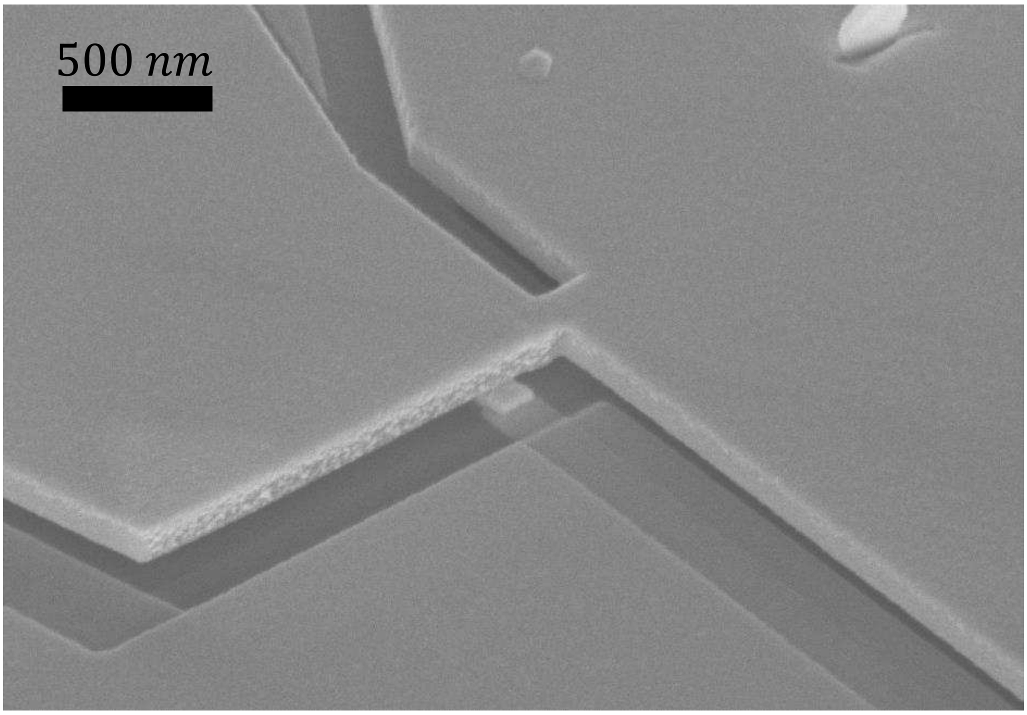

Figure 3.15: SEM image of an end of the tunnel junction after MBE growth taken at an angle (image taken by Tobias Schmitt).

3.5 Estimation of the tunnel barrier thickness

A rough estimate for the thickness of the deposited tunnel barrier was calculated using a Python script. The script illuminates a polygon that corresponds to the layout of the hard mask. The shadow cast by the hard mask after a substrate rotation is then calculated from this polygon. A grid of points is placed over this polygon and then projected onto the substrate. This results in a shift of the projected point due to the molecular beam angle of 32.5°. The angle θ is the angle of incidence of the molecular beam. The angle ϕ describes the state of rotation of the substrate. The simple transformation matrix $\overline{T}(\theta, \phi)$ shown in equation (3.1) is made possible by the fact that the molecular beams can be assumed to be parallel.

$$P_{\mathrm{F}} = \overline{T} \cdot P_{\mathrm{M}}$$

$$\overline{T}(\theta, \phi) = \begin{pmatrix} 1 & 0 & \frac{\cos(\phi)}{\tan(\theta)} \\ 0 & 1 & \frac{\sin(\phi)}{\tan(\theta)} \\ 0 & 0 & 0 \end{pmatrix} \tag{3.1}$$

A point P_{M} of the mask is transformed using the matrix $\overline{T}$ so that it is projected onto the substrate level. This new point is referred to as P_{F} here. It should be noted that such a simple calculation cannot take the thickness of the mask into account. In this calculation, it is assumed to be infinitesimally thin. Surface diffusion is also neglected. The result of such a calculation can be seen in Figure 3.16. This showed that the deposition rate at the tunnel contact can be reduced by up to 80% by the shadow cast.

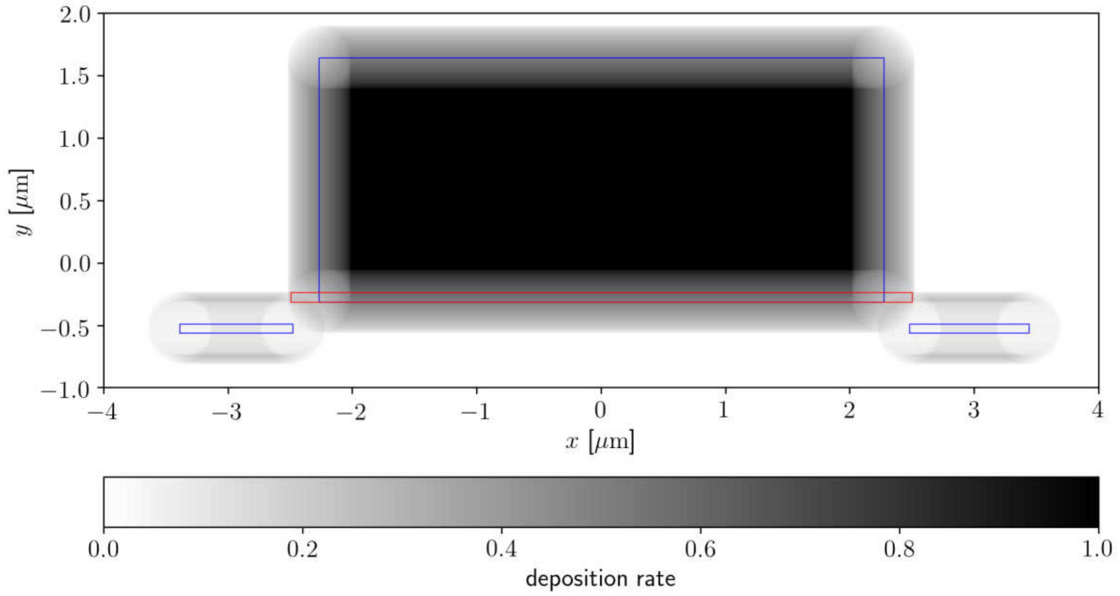

Figure 3.16: Representation of a calculated deposition rate after substrate rotation. A value of 1 means that there was no shading during substrate rotation, so there was no influence of the mask on the deposition rate. Accordingly, values less than 1 mean that the hard mask has shaded the area and reduced the deposition rate. The holes in the hard mask is shown as blue polygons and the TI nanoribbon as a red polygon.

3.6 Stencil mask removal

An important point in the fabrication process is the removal of the stencil lithography mask after the growth of the TI, it was metallized during the fabrication of the superconducting and normal conducting contacts. There are major reasons why we do not want to have a metallized mask on the samples when measuring it. Since a magnetic field is to be applied for later measurements, the superconductor on the mask must be removed to avoid shielding effects by the superconductor. The removal is also important to avoid short circuits of the contacts over this metal layer. Last but not least the fabrication of top gates is prevented by the presence of the mask.

The challenge here is to remove the mask as completely as possible without damaging the tunnel junction. Different processes are suitable for this. Their advantages and disadvantages will be explained below.

3.6.1 Remove via wet etching

Experiments were carried out to remove a hard mask by etching with 1% HF solution, as in the process step to under-etch the mask. The SiO_2 layer under the mask is removed by the etching. So is the Si_3N_4 mask with the metals lift off if the etching time is sufficiently long. In order to protect the created structures, a selenium capping is applied before the etching. The selenium capping is highly resistant to HF etching and can thus protect the underlying structures.

The test sample used is a grid mask on which Al (as dummy metal) was deposited which was then covered with the selenium capping. The selenium capping is deposited under rotation, so it is deposited below the mask without any shadows.

The result after etching and evaporation of the selenium is shown in Figure 3.17(a). Unfortunately one can clearly see that the Al structures were strongly attacked. So it can be assumed that HF can penetrate the edges of the capping between the Si and the Se shown in Figure 3.17(b). In this way an unwanted etching of the Al takes place. In addition, large parts of the hard mask are left behind and have not completely detached.

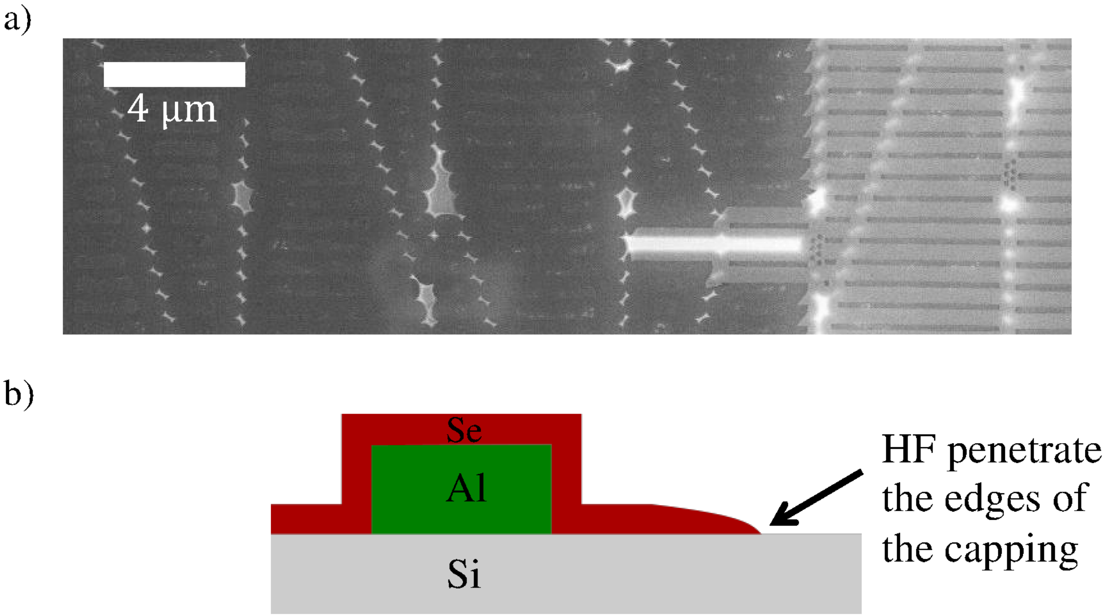

Figure 3.17: a) SEM image of a selenium-capped sample after wet etching with 1% HF solution for 3 min and evaporating the capping. b) Schematic representation of the cross-section of a part of the sample. The 1% HF solution can possibly penetrate at the edge of the Se capping between the Si and the Se (see arrow).

3.6.2 Frame etching

Experiments were carried out to remove parts of the hard mask by RIE etching. This requires a further EBL step to determine which areas of the hard mask should be etched. Since the etching is performed relatively close to relevant structures that should not be damaged, a very good alignment is required to ensure that only the desired areas are etched.

Compared to polishing described in section 3.6.3, this is a clean process as no polishing paste is used and no other mechanical damage can occur. The disadvantage is that the sample is heated during RIE etching which can make it difficult to remove resist.

A test sample was used which has the same layer stack as the tunnel junction. The result is shown in Figure 3.18 and can be seen as promising. The edges are well defined and the resist has protected the other areas well. The removal of the resist residues turned out to be unproblematic.

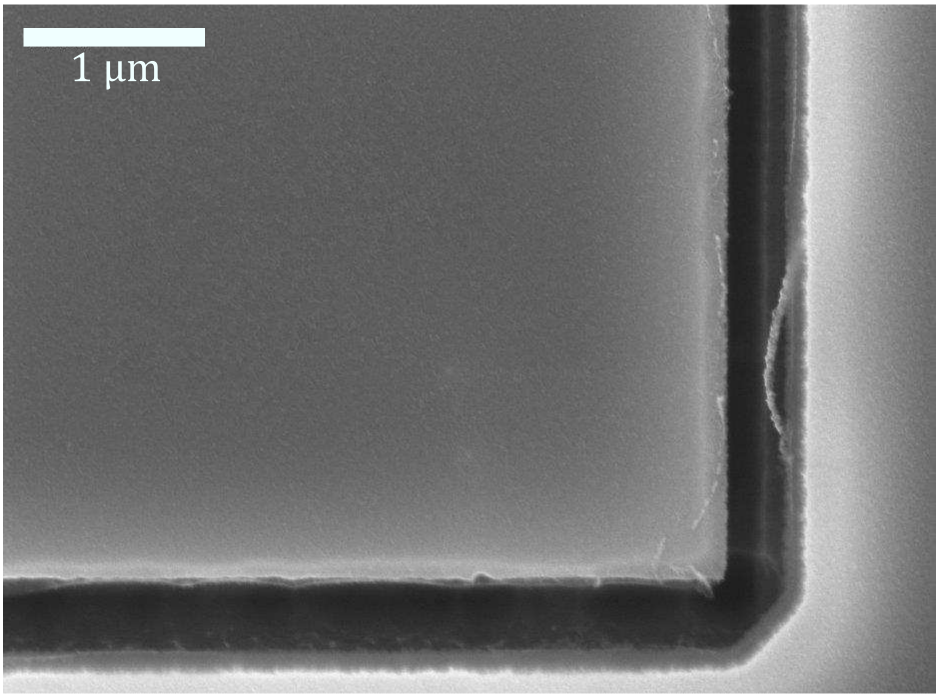

Figure 3.18: SEM image of the sample after frame etching with RIE process.

3.6.3 Polishing

Mechanical polishing of the hard mask with a polishing paste while resist protects the lower lying structures is a proven procedure [10] and is relatively reliable. It also prevents possible negative effects due to chemical influence on the tunnel junction due to the purely mechanical principle of action.

Nevertheless, this also has its disadvantages. The nanostructures can be damaged during polishing by larger particles that come off the sample. An important disadvantage in relation to the production of the tunnel junction is that polishing the hard platinum layer has proven to be difficult. Thus, an overhang of Si_3N_4 remains at the edge of the mask, which makes the later fabrication of gates more difficult.

Figure 3.19 shows a SEM image of a tunnel junction that has been polished with the procedure described above. The polishing procedure was also used for the sample measured in chapter 5.

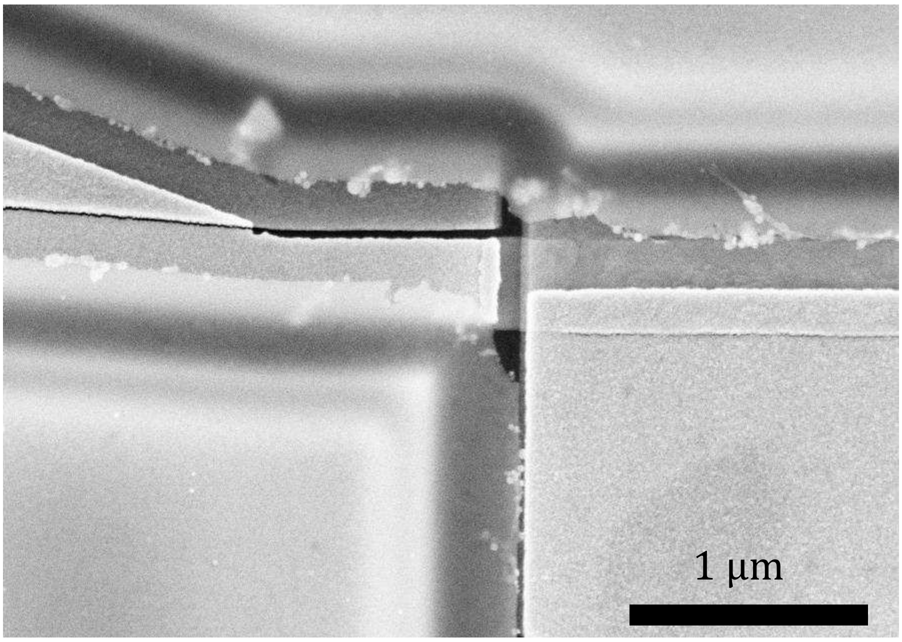

Figure 3.19: SEM image of a tunnel junction after polishing. On the edges of the mask protruding Si_3N_4 residues can be seen, which appear slightly transparent. In addition, some residues from the polishing compound can be seen.

4 Quantum transport modeling (with Kwant)

Quantum transport simulations were performed to get a better understanding of the expected measurement results. Kwant is a Python package that makes it easy to define tight-binding models and calculate the quantum transport properties of nanostructures of any geometry. Thus the scattering matrix and with the help of this matrix the conductivity over a tunnel junction can be calculated. It was developed by Christoph W. Groth, Michael Wimmer, Anton R. Akhmerov and Xavier Waintal [69].

To create a tight-binding model that can be applied to various device shapes, an effective continuum model for the bulk electronic band structure near the Γ point is discretized on a grid. The resulting terms can be classified as onsite terms and hopping terms, yielding a graph consisting of sites and hoppings that connect them. The nodes and connections of this graph are then assigned to the terms obtained by the discretization procedure. Semi-infinite leads can be connected to a discretized system under consideration and the scattering matrix, connecting all the input and output modes, can be calculated efficiently with Kwant. By specifying which of the leads is the input and output lead, Kwant can then use the scattering matrix to calculate the conductance.

4.1 Model for the tunnel junction

The model was inspired by the model presented in Ref. [70, 71] to model a tunnel contact. The main differences to the model presented here are the adaptation to the investigated experimental setup and the simulation of a 3D-TI with a real 3D model. The model consists of five parts in total. A central non-superconducting 3D-TI cuboid, which is connected from above with a tunnel contact. The tunnel contact consists of a metal lead which is connected to a metal monolayer of sites. This monolayer in turn couples to the TI cube and hopping between TI and metal is governed by a single tunneling parameter to represent the actual tunnel barrier in the simulations. The TI cube is connected to a lead of superconducting TI from the side. The system and connected leads are presented in Figure 4.1.

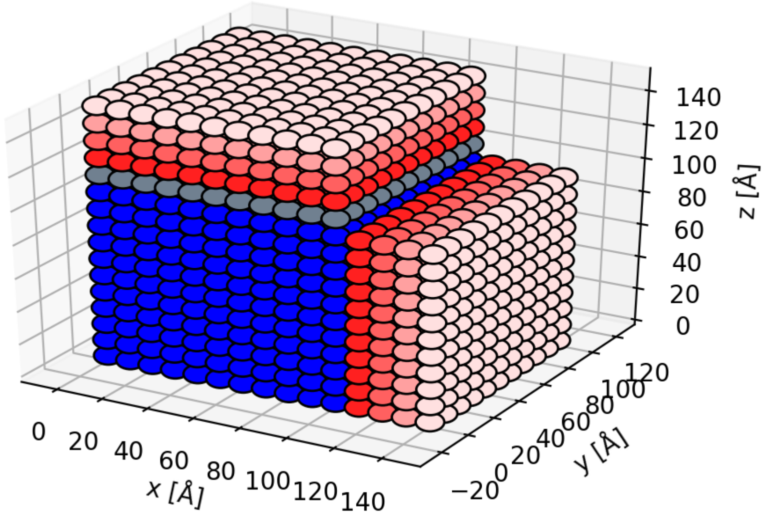

Figure 4.1: A Plot of the Kwant system, with each sphere shown representing a site of the tight-binding model. The monolayer of sites (gray) represents metal. The hopping terms from this metal to the TI (blue) in the z direction are adjusted with a tunnel parameter t. The lead connected to the metal from above represents also metal (the layers with red and light red color represent the infinite leads). The blue area consists of TI with $\Delta = 0$ to which a lead from TI with $\Delta > 0$ is connected.

We consider the effective 4-band Hamiltonian for the Bi_2Se_3 material family. This Hamiltonian has been derived using $\boldsymbol{k} \cdot \boldsymbol{p}$ perturbation theory around the Γ-point and symmetry considerations in Ref. [28, 72]. The Hamiltonian is

$$\begin{aligned} \mathrm{H(k)} &= \epsilon(k) + \mathrm{M}(k) s_z + A_\perp s_x\left(k_x \sigma_x + k_y \sigma_y\right) + A_z k_z s_x \sigma_z, \\ \epsilon(k) &= C_0 - C_\perp\left(k_x^2 + k_y^2\right) - C_z k_z^2, \\ M(k) &= M_0 - M_\perp\left(k_x^2 + k_y^2\right) - M_z k_z^2 \end{aligned} \tag{4.1}$$

with z as the stacking direction for the quintuple layers and the Pauli matrices $\boldsymbol{s} = \left(s_x, s_y, s_z\right)$ and $\boldsymbol{\sigma} = \left(\sigma_x, \sigma_y, \sigma_z\right)$, $\boldsymbol{s}$ acting on the orbital and $\boldsymbol{\sigma}$ on the spin subspace. A Kronecker product is assumed between the Pauli matrices, which is not explicit in the notation. To take superconductivity into account, the conventional procedure is used to obtain a Bogoliubov-de Gennes (BdG) Hamiltonian

$$\mathcal{H} = \frac{1}{2}\sum_{k} \psi_k^{\dagger} H^{\mathrm{BdG}} \psi_k, \tag{4.2}$$

$$H^{\mathrm{BdG}}(k) = \begin{pmatrix} H - \mu_{\mathrm{TI}} & i\sigma_y\Delta \\ -i\sigma_y\Delta^* & \mu_{\mathrm{TI}} - H^{\dagger} \end{pmatrix} \tag{4.3}$$

This adds the superconducting order parameter Δ to the Hamiltonian. A chemical potential μ_{TI} is also added. In the notation with Pauli matrices and Kronecker product, the Hamiltonian can be written as follows

$$\begin{aligned} H^{\mathrm{BdG}}(\boldsymbol{k}) = (\epsilon(\boldsymbol{k}) - \mu)\tau_z s_0 \sigma_0 + M(\boldsymbol{k})\tau_z s_z \sigma_0 + A_{\perp} s_x\left(k_x \tau_0 \sigma_x + k_y \tau_z \sigma_y\right) \\ + A_z k_z \tau_0 s_z \sigma_x - \Delta \tau_y s_0 \sigma_y \end{aligned} \tag{4.4}$$

with the Pauli matrices $\boldsymbol{\tau} = \left(\tau_x, \tau_y, \tau_z\right)$ acting on the particle-hole subspace. The Hermitian operator $H^{\mathrm{BdG}}(k)$ acts on the eight-component Nambu spinor

$$\Psi_{\boldsymbol{k}} = \begin{pmatrix} c_{\boldsymbol{k}\uparrow A} & c_{\boldsymbol{k}\uparrow B} & c_{\boldsymbol{k}\downarrow A} & c_{\boldsymbol{k}\downarrow B} & c_{-\boldsymbol{k}\uparrow A}^{\dagger} & c_{-\boldsymbol{k}\uparrow B}^{\dagger} & c_{-\boldsymbol{k}\downarrow A}^{\dagger} & c_{-\boldsymbol{k}\downarrow B}^{\dagger} \end{pmatrix}^{\dagger}. \tag{4.5}$$

The basis ensures that the BdG Hamilton H^{BdG} has the form shown in Equation (4.4).

For the normal conducting lead of the model and a monolayer (gray in Figure 4.1) the following Hamiltonian

$$H_{\mathrm{Metal}}(\boldsymbol{k}) = \left(\frac{\hbar^2}{2m_e}\left(k_x^2 + k_y^2 + k_z^2\right) - \mu_{\mathrm{M}}\right)\tau_z s_0 \sigma_0 \tag{4.6}$$

is used to model a metal, with the effective mass m_e, the chemical potential for the metal μ_{M}, and the reduced Planck constant $\hbar$.

The hopping matrix for the tunnel barrier between the metal layer and TI has the form

$$H_{\text{hop-tunnel}} = \frac{t}{2}\sigma_0 \tau_0 (I_{2\times 2} + s_x) \tag{4.7}$$

where $H_{\text{hop-tunnel}}$ is diagonal in spin and particle-hole subspace, but randomly coupled to the different atomic orbitals.

4.1.1 Discretization of the Hamiltonian

To maintain the onsite and hopping terms, the Hamiltonian must be discretized. The proceeding is analog to the procedure shown in Ref. [73]. For this, $\boldsymbol{k}$ is replaced by $-i\,\nabla$ in the Hamiltonian

$$\begin{aligned} H^{\mathrm{BdG}} = {} & (\epsilon - \mu)\tau_z s_0 \sigma_0 + M \tau_z s_z \sigma_0 + i A_\perp s_x \left(\partial_x \tau_0 \sigma_x + \partial_y \tau_z \sigma_y\right) \\ & + i A_z\, \partial_z \tau_0 s_z \sigma_x - \Delta \tau_y s_0 \sigma_y, \end{aligned} \tag{4.8}$$

with $\epsilon = C_0 - C_\perp\left(\partial_x^2 + \partial_y^2\right) - C_z\, \partial_z^2$, $M = M_0 - M_\perp\left(\partial_x^2 + \partial_y^2\right) - M_z\, \partial_z^2$.

The Hamiltonian H^{BdG} is discretized to a cubic lattice with the lattice constant a. The grid is indexed with integer $(x, y, z) = (ai, aj, ak) = \boldsymbol{r}$ grid coordinates. The differential operators can then be written with the help of creation and annihilation operators $c_{\boldsymbol{r}}^\dagger, c_{\boldsymbol{r}}$ in position space. The first and second order derivatives then have the following form

$$\begin{aligned} \partial_x &= \frac{1}{a} \sum_{i,j,k} \left(c_{\boldsymbol{r}}^\dagger c_{\boldsymbol{r}+a\hat{\boldsymbol{x}}} - c_{\boldsymbol{r}}^\dagger c_{\boldsymbol{r}}\right) \\ \partial_x^2 &= \frac{1}{a^2} \sum_{i,j,k} \left(c_{\boldsymbol{r}}^\dagger c_{\boldsymbol{r}+a\hat{\boldsymbol{x}}} + c_{\boldsymbol{r}+a\hat{\boldsymbol{x}}}^\dagger c_{\boldsymbol{r}} - 2 c_{\boldsymbol{r}}^\dagger c_{\boldsymbol{r}}\right). \end{aligned} \tag{4.9}$$

Corresponding expressions are obtained for the other derivatives $\partial_y, \partial_z, \partial_y^2, \partial_z^2$. With these differential operators, the Hamiltonian operator can now be converted into a form in, which the onsite and hopping terms required for the tight binding model appear explicitly.

$$H = \sum_{i,j,k} \boldsymbol{c}_{\boldsymbol{r}}^\dagger\, H_{\mathrm{onsite}} \boldsymbol{c}_{\boldsymbol{r}} + \sum_{i,j,k} \left(\boldsymbol{c}_{\boldsymbol{r}}^\dagger H_{\mathrm{hop,x}} \boldsymbol{c}_{\boldsymbol{r}+a\hat{\boldsymbol{x}}} + \boldsymbol{c}_{\boldsymbol{r}}^\dagger H_{\mathrm{hop,y}} \boldsymbol{c}_{\boldsymbol{r}+a\hat{\boldsymbol{y}}} + \boldsymbol{c}_{\boldsymbol{r}}^\dagger H_{\mathrm{hop,z}} \boldsymbol{c}_{\boldsymbol{r}+a\hat{\boldsymbol{z}}}\right) \tag{4.10}$$

$\boldsymbol{c}_{\boldsymbol{r}}^\dagger, \boldsymbol{c}_{\boldsymbol{r}}$ is now a vector of creation and annihilation operators, like $\Psi_{\boldsymbol{k}}$ [10], with the difference that they act in the position space instead of in the momentum space. With the onsite and hopping matrices

$$
\begin{aligned}
H_{\mathrm{hop,x}} &= \frac{1}{2a^2}(C_\perp \tau_z s_0 \sigma_0 + M_\perp \tau_z s_z \sigma_0) + \frac{iA_\perp}{2a} s_x \tau_0 \sigma_x \\
H_{\mathrm{hop,y}} &= \frac{1}{2a^2}(C_\perp \tau_z s_0 \sigma_0 + M_\perp \tau_z s_z \sigma_0) + \frac{iA_\perp}{2a} s_x \tau_z \sigma_y \\
H_{\mathrm{hop,z}} &= \frac{1}{2a^2}(C_z \tau_z s_0 \sigma_0 + M_z \tau_z s_z \sigma_0) + \frac{iA_z}{2a} s_0 \tau_z \sigma_x
\end{aligned}
\tag{4.11}
$$

these matrices can then easily be used to define a tight binding model with Kwant.

4.1.2 Peierls substitution

In section 2.1.1, the behavior under the influence of a magnetic field is described. To simulate the orbital effect, the Peierls substitution method [74] is applied to the hopping terms of the tight-binding model. The hopping terms are multiplied by a phase factor considered here as an example along the x-direction

$$H'_{\mathrm{Hop,x}} = H_{\mathrm{Hop,x}} e^{i\phi_r^x} \tag{4.12}$$

with the phase factor $e^{i\phi_r^x}$, and the hopping term is represented by $H_{\mathrm{Hop,x}}$ as described in Ref. [73]. With the phase

$$\phi_r^x = \frac{q}{\hbar}\int_i^{i+1} \boldsymbol{A}_x(x, aj, ak)\,\mathrm{d}\,x \tag{4.13}$$

the procedure is identical for the coordinates y, z. The charge q is negative in case of holes. This is important when using a BdG Hamiltonian to take into account the correct charge for the hole block. The vector potential used is defined according to $\boldsymbol{B} = \nabla \times \boldsymbol{A}$ and must be chosen such that it results in the desired magnetic field $\boldsymbol{B}$ in the simulations.

4.1.3 Transport simulations

There are currently no values available for the material parameters of $(\mathrm{Bi}_{1-x}\mathrm{Sb}_x)_2\mathrm{Te}_3$ in Equation (4.11). Therefore, simple parameters from Ref. [75] are used to capture the essential features of a 3D-TI bulk and surface state spectrum. These are $A_\perp = 3$ eV·Å, $A_z = 3$ eV·Å, $M_0 = 0.3$ eV, $M_\perp = 15$ eV·Å^2, $M_z = 15$ eV·Å^2, $C_0 = 0$ eV, $C_\perp = 0$ eV·Å^2, $C_z = 0$ eV·Å^2.

The question arises for which chemical potential μ_{TI} and magnetic field strength B_x a MBS and therefore ZBP appears? To answer this question a phase diagram of the tunnel junction is simulated using the parameters μ_{TI} and B_x. To get a MBS we also have to open a superconducting gap. For this we set $\Delta = 0.2\mathrm{meV}$. For the chemical potential of the metal $\mu_{\mathrm{M}} = 1$ meV is chosen so that a conducting channel exists and $t = 15$ meV for the tunnel barrier. This is the value of the hopping terms t in Equation (4.7) and cannot be directly understood as barrier height. The plot of the phase diagram is shown in Figure 4.2. The conductance is always evaluated at an energy of $E = 0$ (ZBP at E = 0).

From basic theoretical considerations, only a diamond structure with a conductivity of $G = 0$ and $G = 2e^2/h$ would be expected. In the diamond-shaped areas with conductivity $G = 2e^2/h$ a MBS is present and all other areas have a conductivity of $G = 0$. This structure results from the number of bands that intersect the Fermi level. Only for an odd number of band crossings a MBS exists. As the position of the Fermi level and the bands with μ and B_x changes, the number of band crossings also changes.

This diamond pattern is not exactly shown in Figure 4.2, which can probably be traced back to symmetry effects. For the simulated nanowire cross section, a discrete rotational symmetry exists that protects the spectrum from opening a superconducting gap Δ. This seems to occur predominantly when the induced gap Δ has no winding phase around the circumference of the nanowire as described in Ref. [76]. This is different from the winding phase assumptions made in the work of Cook et al [29].

The details of this conductance pattern and deviations from the expected diamond pattern are still unclear and form an interesting topic for further investigation.

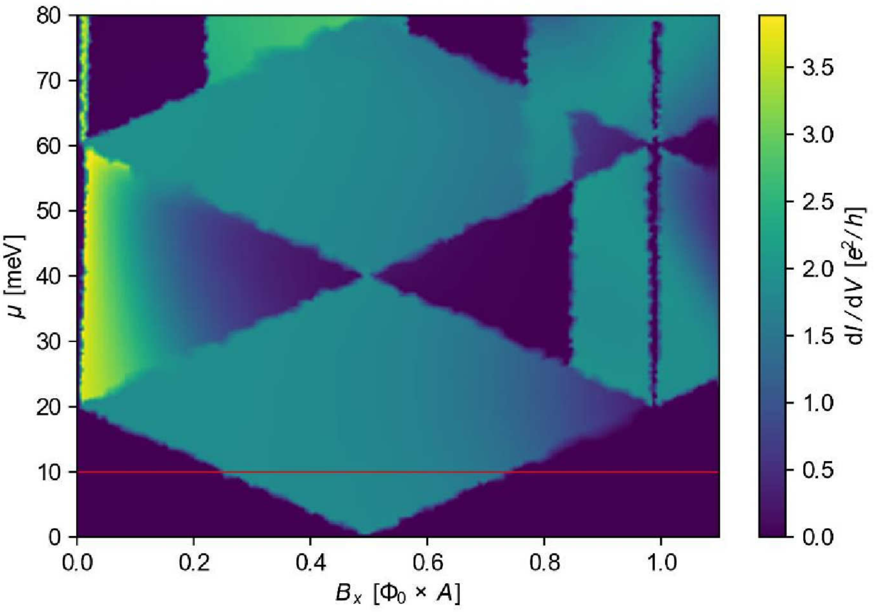

Figure 4.2: Phase diagram of the tunnel junction as a function of μ_{TI} and B_x. In the diamond-shaped areas with a conductivity of $G = 2e^2/h$ there is a ZBP and thus also a MBS. The red line shows the μ_{TI} value at which the simulation of Figure 4.3 was performed.

For a simulation that is closer to the experimentally feasible, the chemical potential is now set to $\mu_{\mathrm{TI}} = 10\,\mathrm{meV}$. Instead of the chemical potential μ_{TI}, the energy E is now varied to calculate the conductivity. This corresponds to a change of the bias voltage in the experiment. This simulation is shown as a color plot in Figure 4.3 and already shows a ZBP. In the Figure 4.4 a line cut through the ZBP is shown so that it is easy to see that the ZBP is quantized to $G = 2e^2/h$.

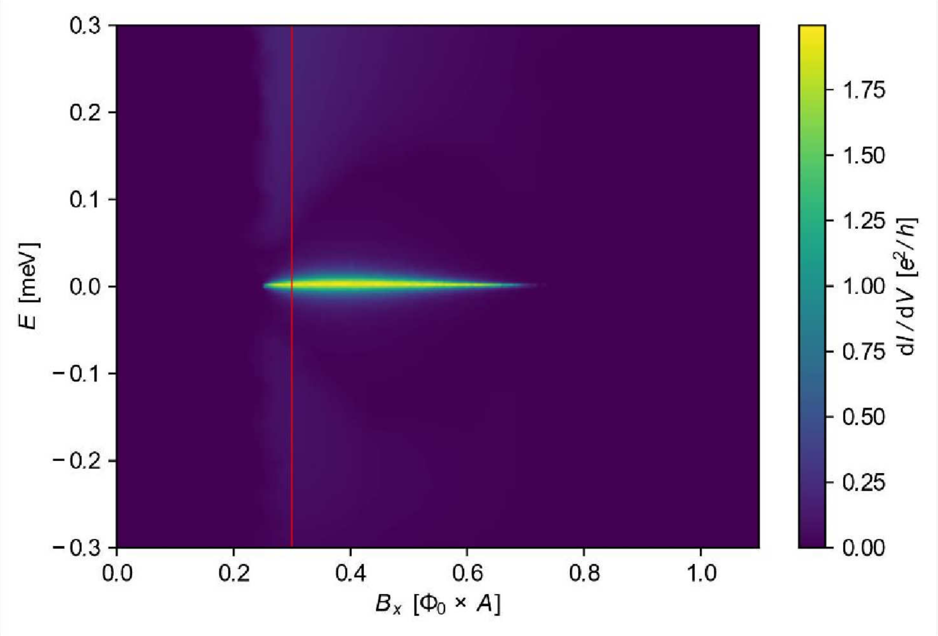

Figure 4.3: Simulation of the ZBP as a function of the magnetic field B_x. The red line shows the position of the line cut shown in Figure 4.4.

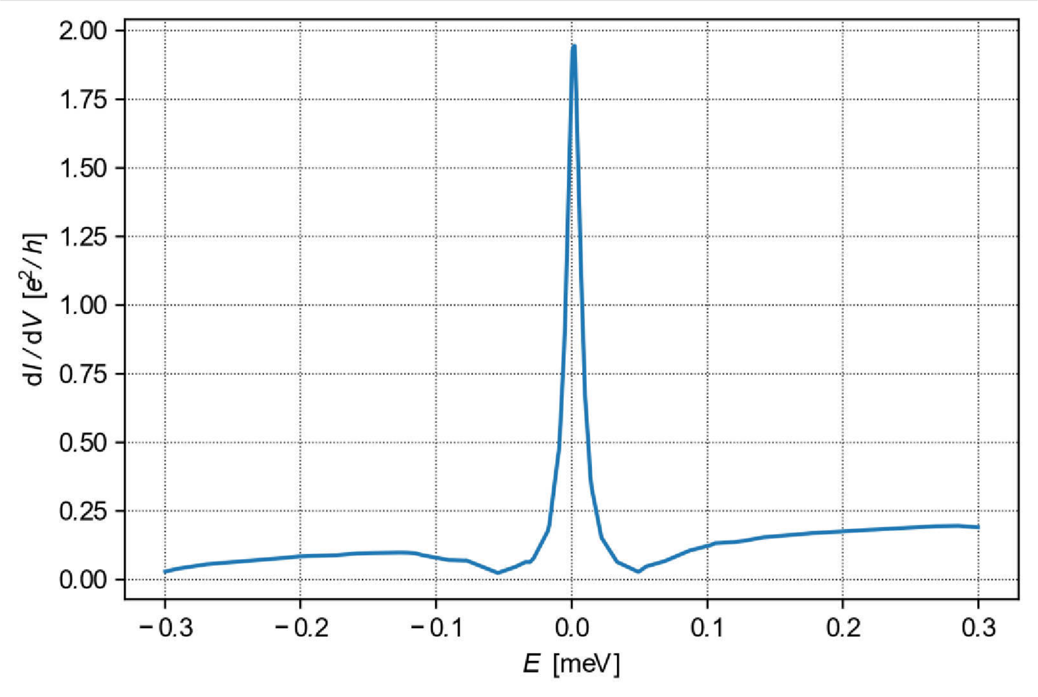

Figure 4.4: Line cut of the simulation shown in Figure 4.3 at $B_x = 0.5\Phi_0$. The plot shows the ZBP quantized in height to $2e^2/h$.

5 Results and Discussion

In the context of this thesis measurements were made on one of the manufactured devices. Special thanks to the University of Twente (UT) for providing the measurement time in their dilution refrigerator. The manufactured chip contains several junctions, so in a first step the quality of each junction was evaluated by means of SEM images. On the basis of these images it was then decided which of these junctions should be bonded.

In previous attempts to bond the samples and take IV measurements at room temperature, it became clear that the junctions are highly sensitive to the introduction of static electricity. Even with very careful handling, all contacted junctions on a first chip were destroyed. In order to minimize such influences, no further attempts were made to record IV curves of the junctions at room temperature. After loading the chip into the dilution fridge and first test measurements it turned out that only one junction was intact it can be assumed that all other junctions on the chip were destroyed due to electrostatic discharge.

To characterize the junction, the tunnel conductivity was investigated at different temperatures and magnetic field strengths. The magnetic field applied was aligned in-plane along the TI nanoribbon in all measurements.

5.1 Geometry of the measured tunnel junction

An SEM image of the junction measured in the dilution fridge is shown in Figure 5.1. In addition, Figure 5.1 shows the cross-section of the junction for the end. It consists essentially of four components, the TI grown in the trench, a superconductor Nb, a tunnel barrier of Al_2O_3 and a normally conducting contact Pt. The superconductor Nb does not cover the ends of the TI nanoribbon. Instead, they are covered by an insulator Al_2O_3 to which a normally conducting contact Pt is applied. There is no contact between superconductor and normal conductor.

The whole structure is a tunnel contact which is used to determine the density of states locally under the tunnel barrier in TI by tunneling from the normal conductor via the tunnel barrier into TI. In other words, the measured tunnel conductance $\mathrm{d}I/\mathrm{d}V$ is directly proportional to the local density of states as shown in section 2.4.

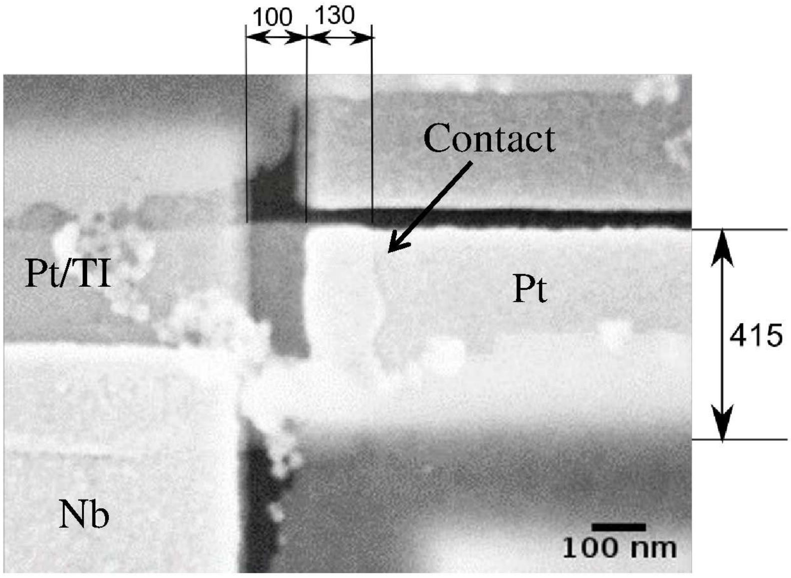

Figure 5.1: SEM image of the junction measured in the dilution fridge. You can see the TI nanoribbon covered with Nb and the overlap between the normal conductor and the TI nanoribbon. The blurred areas of the image are caused by protruding remnants of the mask that were not completely removed during polishing (all lengths indicated in nm).

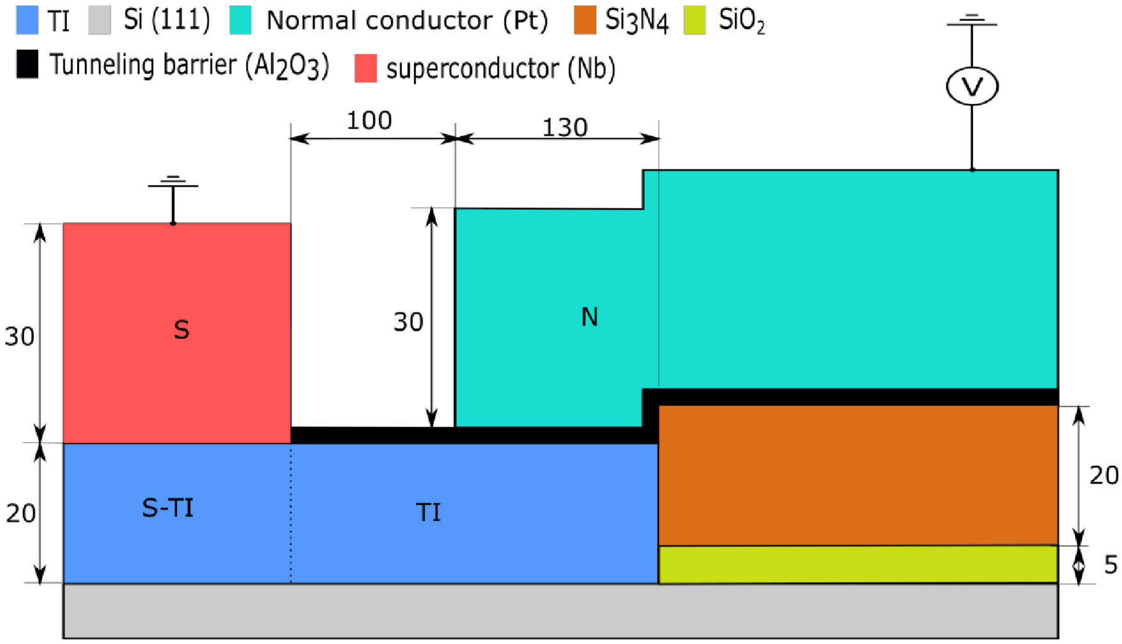

Figure 5.2: Schematic representation of the cross section of the junction end, all lengths in nm (The distances in the horizontal direction are not drawn to scale.)

5.2 Experimental setup

The dilution refrigerator used has superconducting coils with which a magnetic field of $-8\ \mathrm{T}$ to $8\ \mathrm{T}$ can be applied. The orientation of the magnetic field is in-plane along the nanoribbon in all measurements. The setup contains two different temperature sensors to measure different temperature ranges which will be referred to later with T_5 and T_8. The lowest temperature reached during the measurements was about $16\ \mathrm{mK}$ (base temperature). The sample was glued into a chip carrier with conductive silver paint. The contact pads defined in the layout are then bonded to the contacts of the chip carrier. So that e.g. a junction with three contacts occupies a total of six pads on the chip carrier. This enables the comparison of the AC current signal with the AC voltage drop at the tunnel junction and is required for the quasi four-point measurement (one of the two normal conductor contacts of the sample with two bonds is not measured).

The measurement carried out is intended to record the tunnel current from the normal conductor to the superconductor. According to the four-point measurement method, both metals were contacted twice (as described above). A bias DC current is sent via a normal conductor and a superconducting contact, to which an AC current is added with a lock-in amplifier. Parallel to this current, the corresponding DC voltage is measured at the other two contacts. This makes it possible that line and contact resistances up to the contact pads can be neglected. The actual differential conductance is determined by the lock-in amplification. Using an SMU (Source measure unit) operated as a voltmeter, the bias DC voltage drop at the junction is measured. The differential conductance can therefore be determined for different bias DC voltages and currents. A schematic diagram of this measurement setup is shown in Figure 5.3.

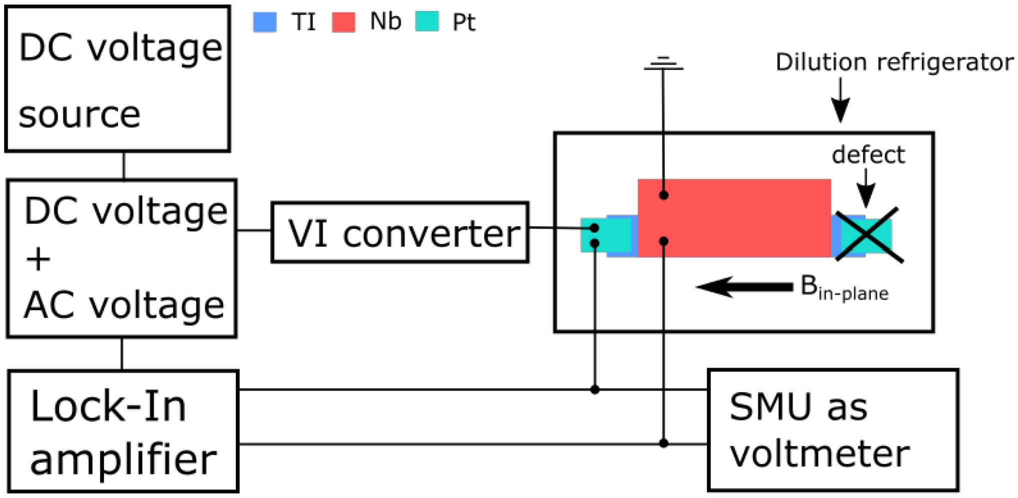

Figure 5.3: Schematic representation of the measurement setup in the MESA+ Institute for Nanotechnology at the University of Twente.

5.3 Differential tunneling conductance

In the wide range measurement shown in Figure 5.4 from -7.75 mV to 7.75 mV at 16 mK and without an applied magnetic field, the gap induced by the proximity effect is immediately visible. The coherence peaks of this gap are also visible. Thus, the width of the gap 2Δ can be estimated to be about 300 μeV to 400 μeV.

Furthermore, no influence of the sweep direction of the bias current on the measured $\mathrm{d}I/\mathrm{d}V$ curves could be detected. This was verified for arbitrary magnetic fields as well as temperatures.

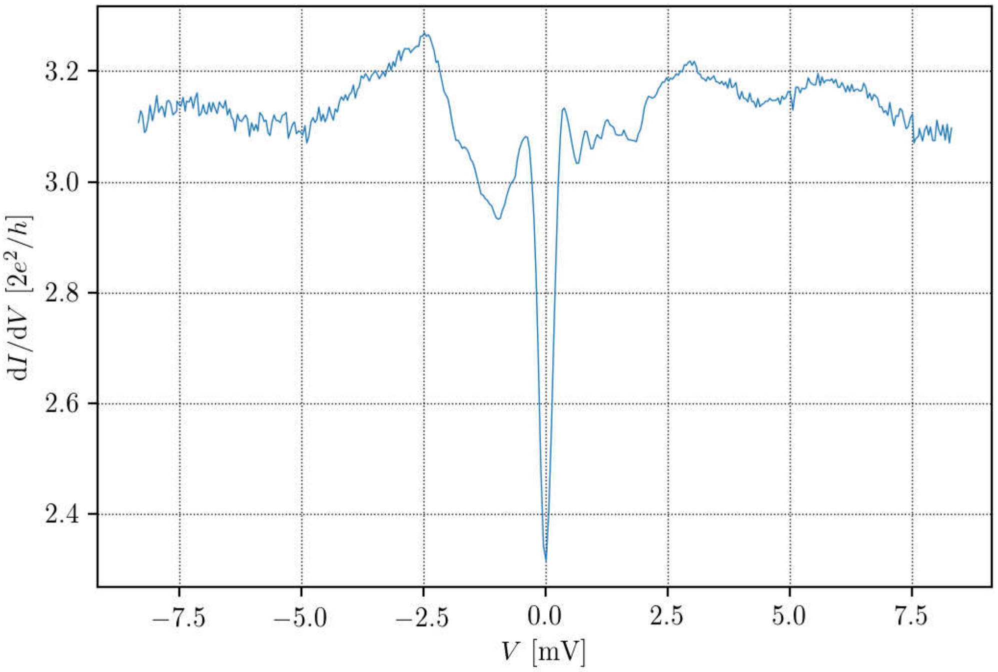

Figure 5.4: Wide-range measurement of the differential conductance over the bias voltage for the tunnel junction at a temperature of 16 mK.

5.3.1 Magnetic field dependency

Different measurements were carried out to investigate the behavior of the tunnel current under the influence of a magnetic field. The magnetic field used was applied in-plane parallel to the wire. At the beginning a measurement with low resolution and short integration time for the lock-in amplifier were performed to get a general overview. This measurement is shown in a color plot in Figure 5.5.

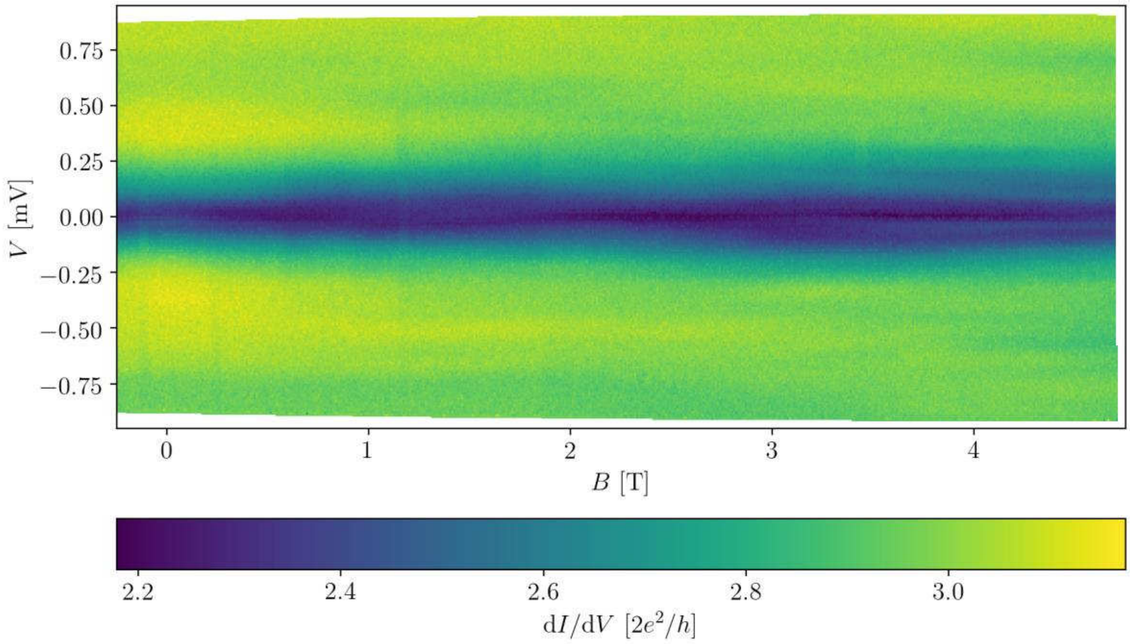

Figure 5.5: Plot of the magnetic field dependency of the tunneling conductance for different bias voltages. First measurements to get a general overview with a resolution for the magnetic field of $\Delta B = 0.01\ \mathrm{T}$ *and a ramp rate of* $0.1\ \mu\mathrm{A/s}$. *In the direction of the bias voltage, the measurement has a resolution of 401 measurement points.*

With this measurement the superconducting gap induced by the niobium is already visible. In addition, it can be seen that even with 8 T the critical magnetic field strength of the superconductor (Nb) was not reached. This was followed by three more field sweeps with a slower measurement speed to get a better resolution. Unfortunately a quench of the superconducting magnet in the cryostat occurred during a measurement due to the failure of the cooling water. Due to its rapid temperature change, this probably changed the behavior of the sample.

In the measurements shown in Figure 5.6, an AC current of 1 nA was used for the lock-in amplifier. This measurement shows subgap features that become more and more visible with increasing magnetic field. Thus, the subgap features are easily recognizable, especially in the B = 6.4 T curves (red arrows in Figure 5.6).

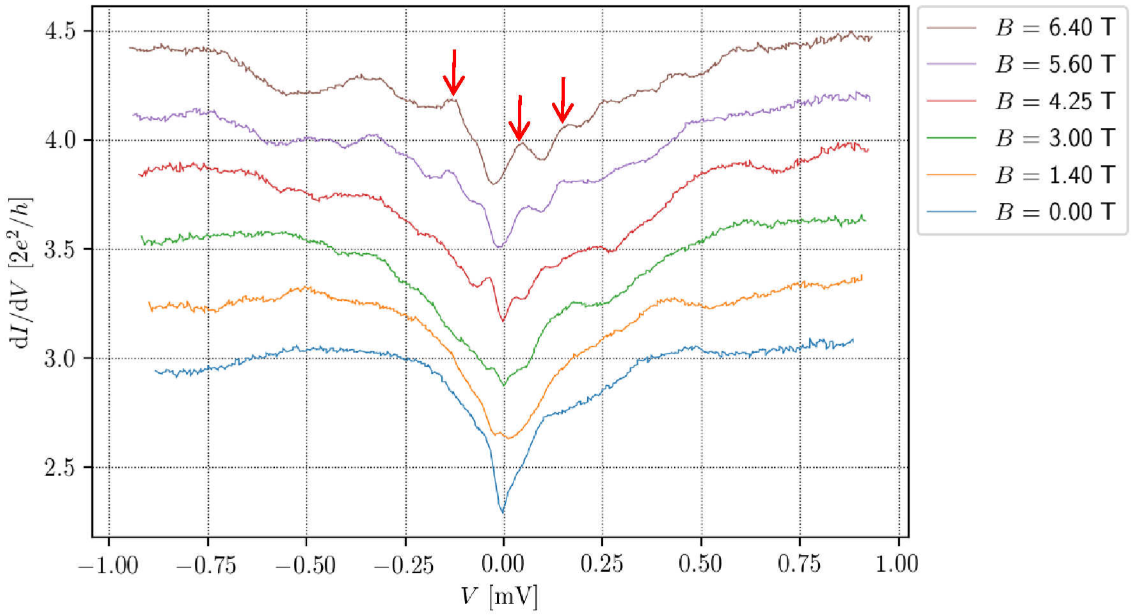

Figure 5.6: Bias voltage sweeps at different magnetic field strengths for large magnetic fields (with red arrows on the subgap features). The offset added for the plot between the curves is $0.3 \times 2e^2/h$.

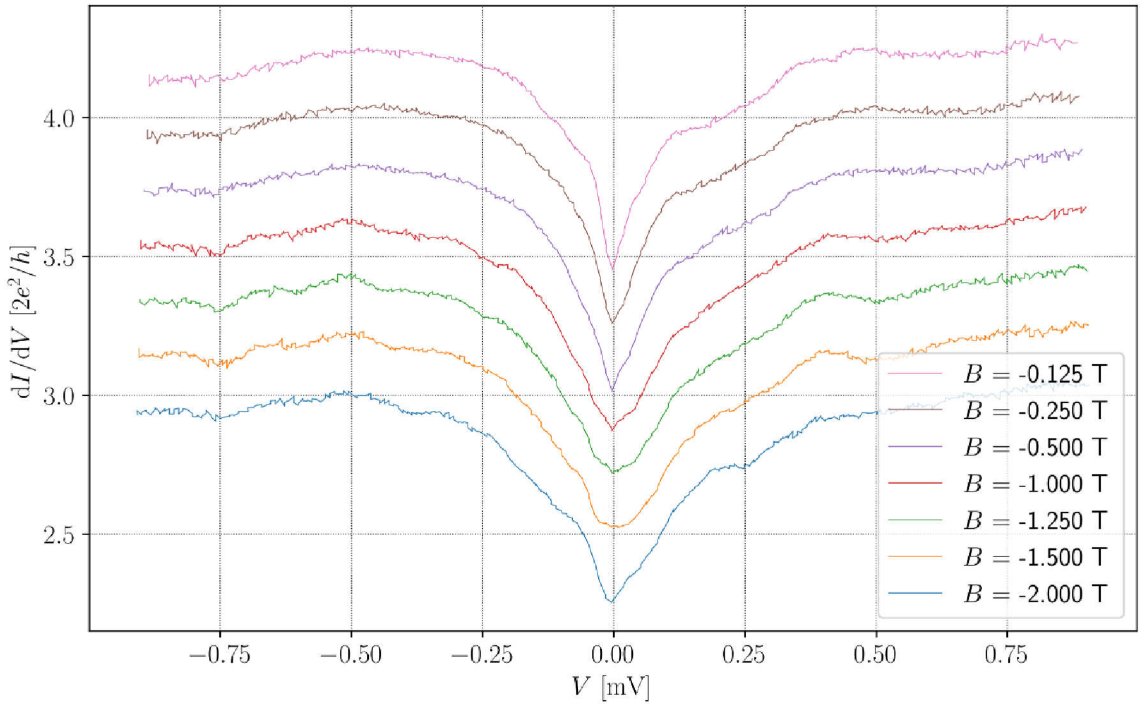

Figure 5.7: Bias voltage sweeps at different magnetic field strengths for small magnetic fields. The offset added for the plot between the curves is $0.2 \times 2e^2/h$. *A change in the gap shape from U-shaped to V-shaped can be clearly seen.*

Figure 5.7 shows the plot of differential conductance measurements over the bias voltage for low magnetic fields. The measurement shows that the gap shape changes with the change of the magnetic field between a V-like shape and a rounded shape. It was also investigated how the differential conductance at zero bias voltage behaves depending on the magnetic field. These measurements are shown in Figure 5.8. At a magnetic flux density of 0.5 T the nanotrench cross-section ($415\,\mathrm{nm} \times 20\,\mathrm{nm}$) is penetrated by a magnetic flux quantum $\Phi_0 = h/e$. However, the oscillations in Figure 5.8 at $T_8 =$ 0.031 K, have a much longer period length, so flux quantum periodicity cannot be observed.

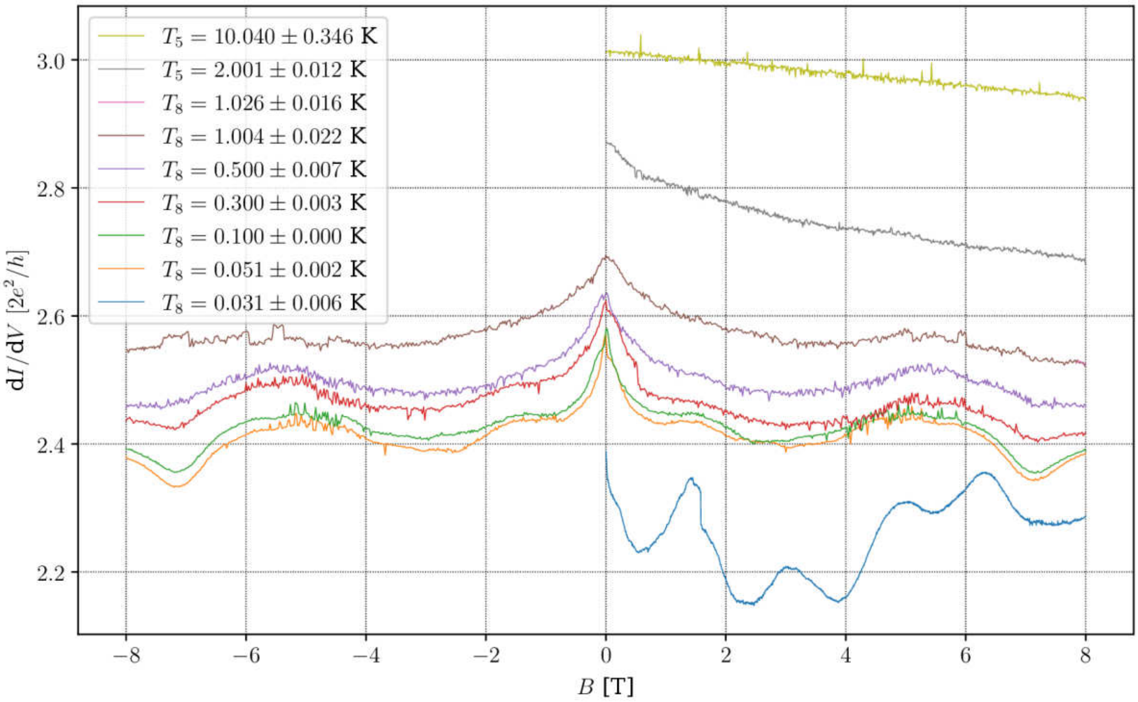

Figure 5.8: Magnetic field sweeps at different temperatures. The blue curve was measured with an AC current of 1 nA *compared to* 10 nA *for the other curves for the lock-in amplifier. A peak can be seen around zero bias voltage, which may be caused by weak anti-localization.*

It can be seen that between 0.031 K and 2 K a peak is formed which is maybe due to weak anti-localization [77, 78]. In addition, an oscillation of the differential conductivity can be clearly detected via the applied magnetic field, especially at 31 mK. However, it is important to note that this curve was measured with an AC current for the lock-in amplifier of 1 nA compared to 10 nA for the other measurements. It can therefore be assumed that the clarity of the oscillation here is not only due to the low temperature, but also to the AC voltage.

5.3.1.1 Dependence of the subgap features on the magnetic field

The second field sweep performed is depicted in Figure 5.9. Here some interesting features can be seen in the superconducting gap which increase especially from about 6 T. Furthermore a general symmetry of these features regarding positive and negative magnetic field can be seen. Because the tunneling conductance is proportional to the local density of states in the nanoribbon end it can be supposed that the features in the superconducting gap are subgap states. These are discussed again in section 5.4.

Figure 5.10 shows line cuts from Figure 5.9, so that without magnetic field only one maybe two subgap features are visible. With an applied magnetic field of 8 T four subgap features are visible. The curves for 8 T and -8 T are almost identical so the peaks are also symmetrical with respect to the magnetic field.

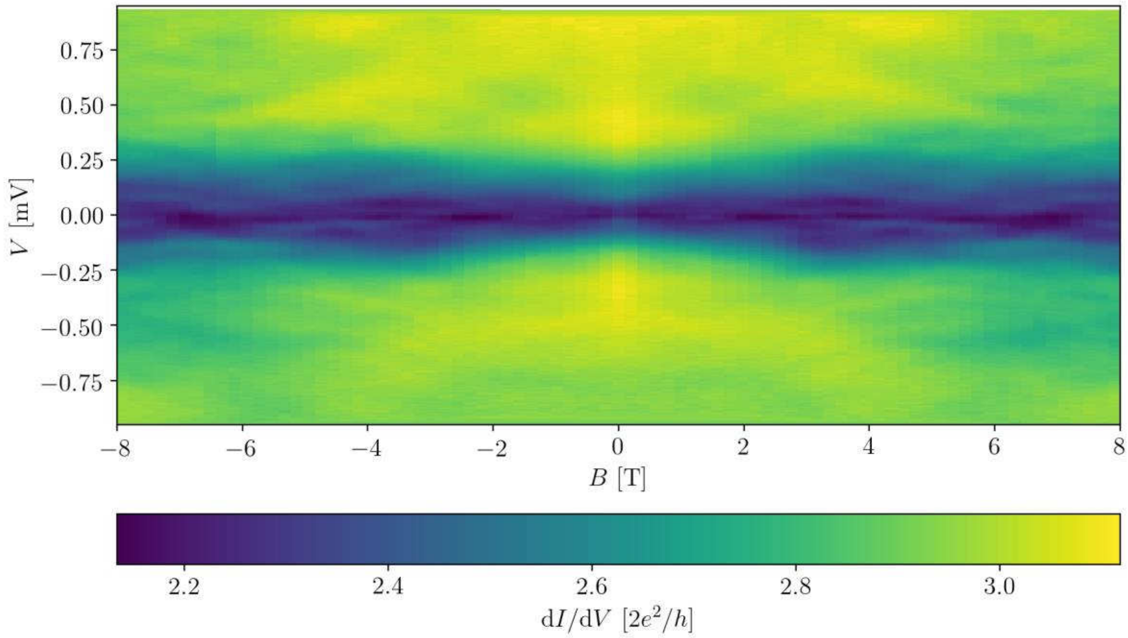

Figure 5.9: Plot of a magnetic field-dependent measurement with a resolution $\Delta B = 0.2$ T *and a ramp rate of* 0.05 µA/s. *In the direction of the bias voltage, the measurement has a resolution of 401 measurement points.*

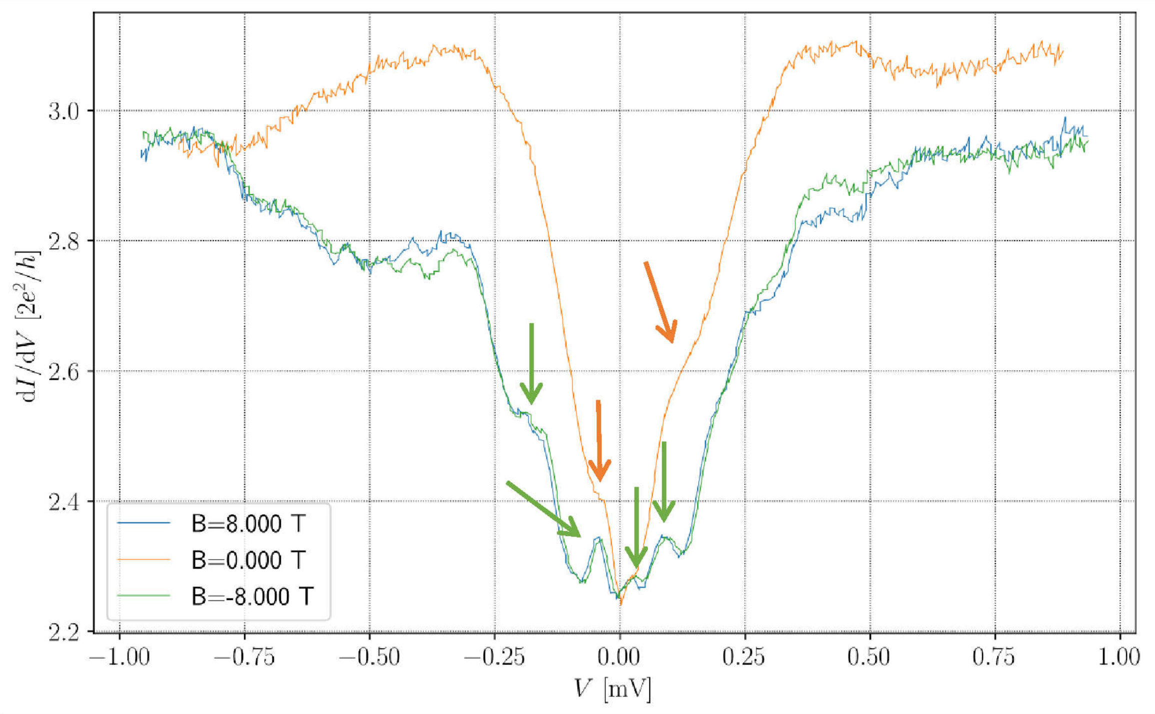

Figure 5.10: Comparison of measurement with positive, negative and without magnetic field. It should be noted that the curves for positive and negative magnetic fields are almost perfectly overlapping.

In Figure 5.11 the same measurement data as in Figure 5.9 is shown as line cut. Each of the curves shown corresponds to an IV sweep at constant magnetic field. In order to be able to clearly display all of them in one plot, a fixed $0.1 \times 2e^2/h$ in relation to the previous curve is added to each of the curves. This makes it easier to recognize the development of individual features in the measured data compared to Figure 5.9.

In Figure 5.11 it can be seen that a subgap feature forms as a visible peak at a certain magnetic field and then changes its energy when the magnetic field changes. Furthermore, the features seem to jump to higher energies when the magnetic field exceeds a certain limit. This statement has to be considered speculative because it is also possible that the state disappears and a new one becomes visible at higher energies.

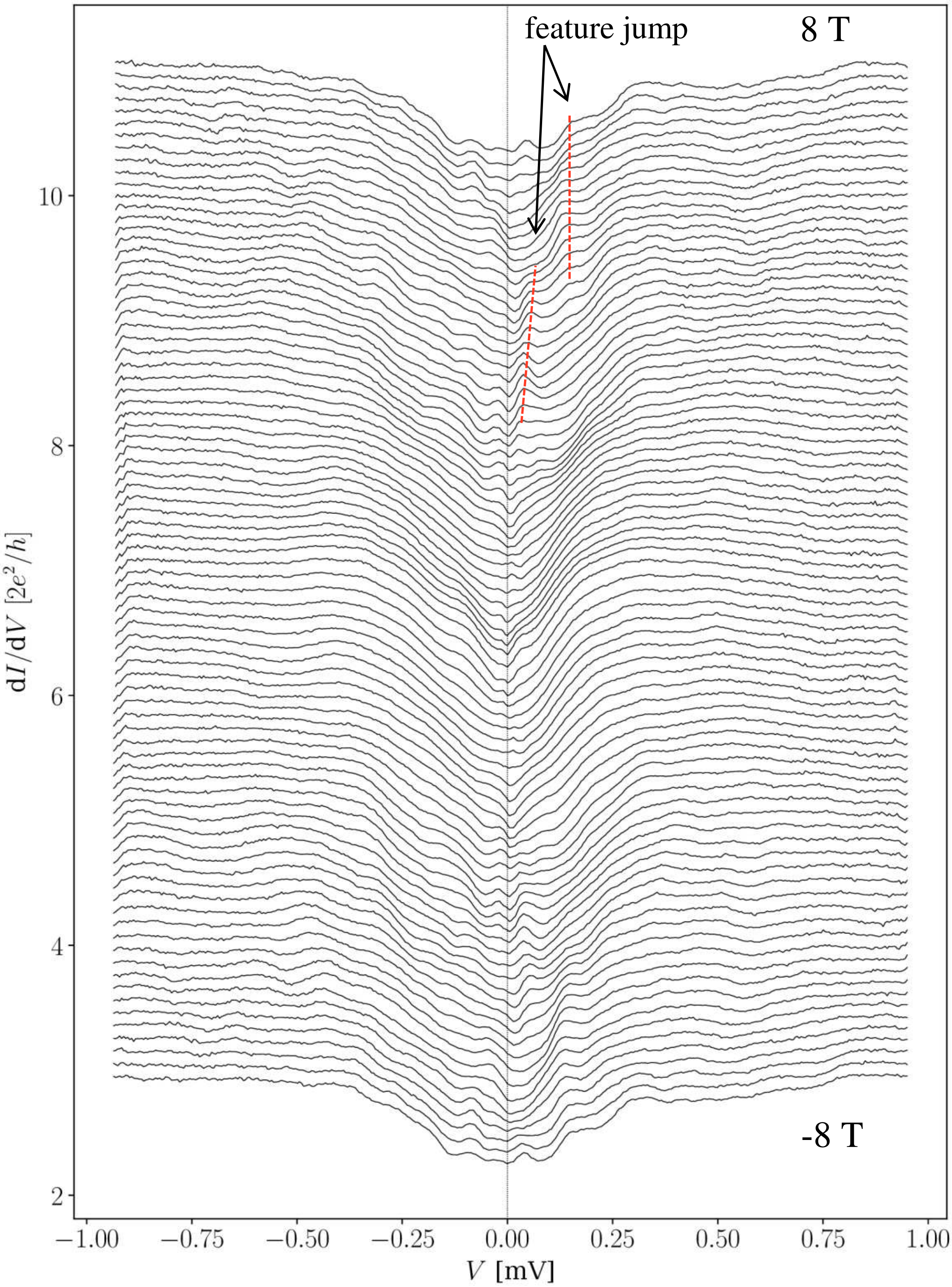

Figure 5.11: Stack plot of line cuts of the measurement shown in Figure 5.9 from -8 T to 8 T. Each curve corresponds to a magnetic field sweep of the measurement. The offset between the curves is $0.1 \times 2e^2/h$.

To better understand the behavior of the peaks in relation to the magnetic field, the positions of the subgap features of Figure 5.11 are shown as points in the V-B plane in Figure 5.12. In addition, features that occurred outside the superconducting gap are also shown as points. Figure 5.12 also shows that the subgap features are symmetrical with respect to the magnetic field direction. Furthermore, the Figure 5.12 shows a widening of the subgap characteristics when the magnetic field strength is increased.

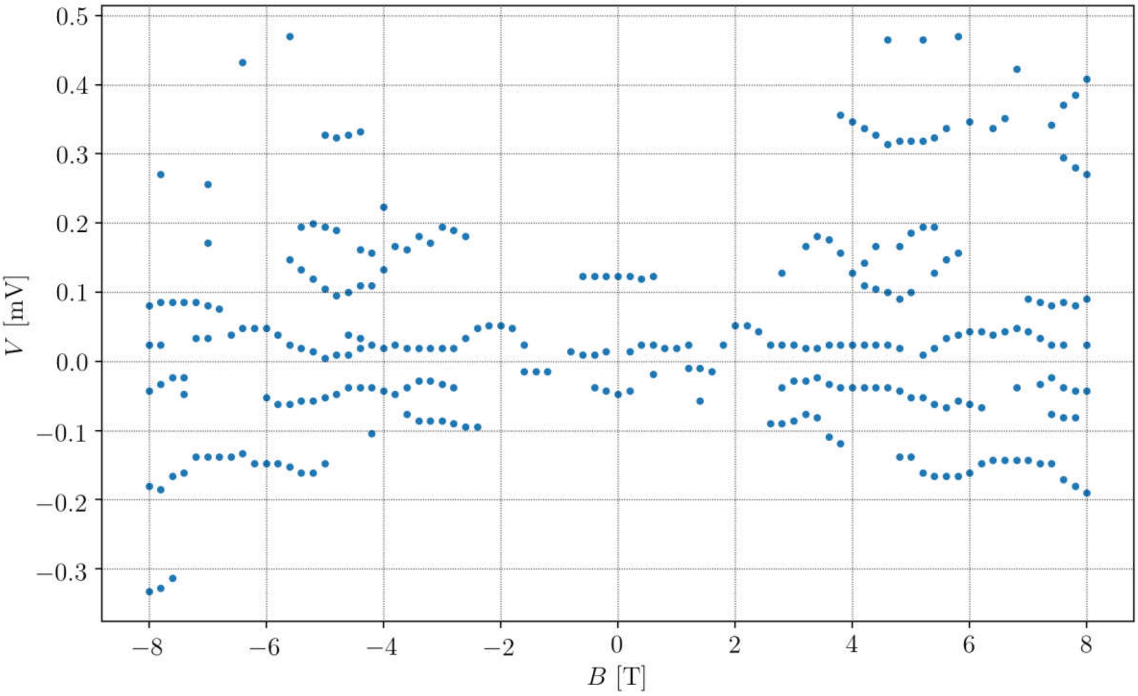

Figure 5.12: Position of the subgap features in the V-B plane of the measurement in Figure 5.9.

The measurement shown in Figure 5.13 provides a better resolution of the subgap states with respect to their magnetic field dependence. It is to see that a subgap feature moves slowly (in the order of 0.04 mV/T) with the amount of the magnetic field (probably continuously) to higher energies. Unfortunately the measurement field sweep resulted in the quench mentioned above. Due to the quench that interrupted the measurement, an accurate magnetic field resolution of the subgap states is only available for −8 T to −6.6 T.

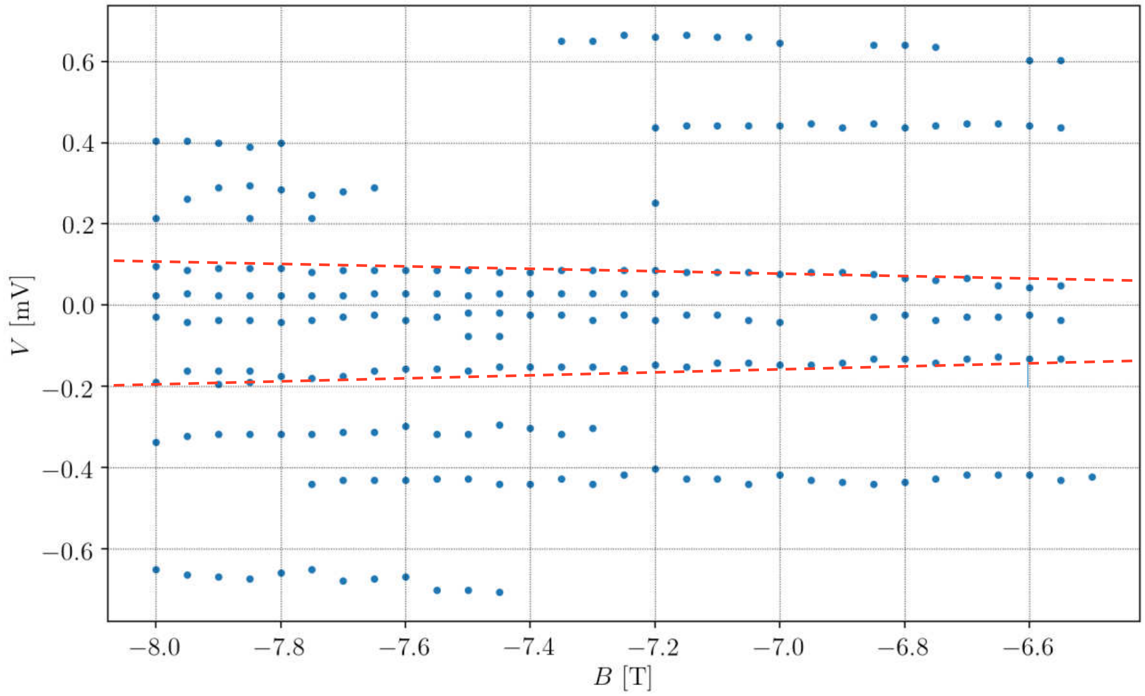

Figure 5.13: Position of the subgap features in the V-B plane of a magnetic field-dependent measurement with a better resolution $\Delta B = 0.05\,\mathrm{T}$ as compared to the measurement in Figure 5.9 with $\Delta B = 0.2\,\mathrm{T}$. The quench took place during this measurement.

After this measurement a further field sweep was performed. However, it was found that the behavior of the sample changed due to the rapid temperature change caused by the quench. For example, the previously visible symmetries of the features are no longer present in the field sweep. Because of this, this measurement is not shown here.

In summary, the measurements showed a soft gap around $E = 0$ of approximately $\Delta \approx 0.25$ meV. Within this soft gap there are subgap peaks showing up as a function of bias voltage V or, alternatively, energy $E = eV$ with a separation of $\Delta E \approx 0.1$ meV with respect to their energy E. These subgap peaks have only a weak dependence of their energy E on the magnetic field B. The subgap peaks become more pronounced for higher magnetic fields B ($B > 2$ T).

5.3.2 Temperature behavior

Different measurements are taken to investigate the temperature dependence of the tunnel junction. In the Figure 5.14 and Figure 5.15 the measurement of the differential tunneling conductance for different temperatures is plotted over the bias voltage. To improve clarity, a fixed offset of $0.3 \times 2e^2/h$ is added to each curve. In Figure 5.14 it can be seen that the superconducting gap opens below 2 K. In Figure 5.15, coherence peaks can also be recognized from approx. 0.5 K.

The width of the opening gap fits well to calculations with the help of $\Delta_0 = 1.76 k_\mathrm{B} T_\mathrm{c} = 0.3$ meV calculated with $T_c = 2$ K. This equation $T_c = \Delta_0 / 1.76\, k_B$ is derived from the BCS theory where the factor 1.76 is to be used for weak coupling [79].

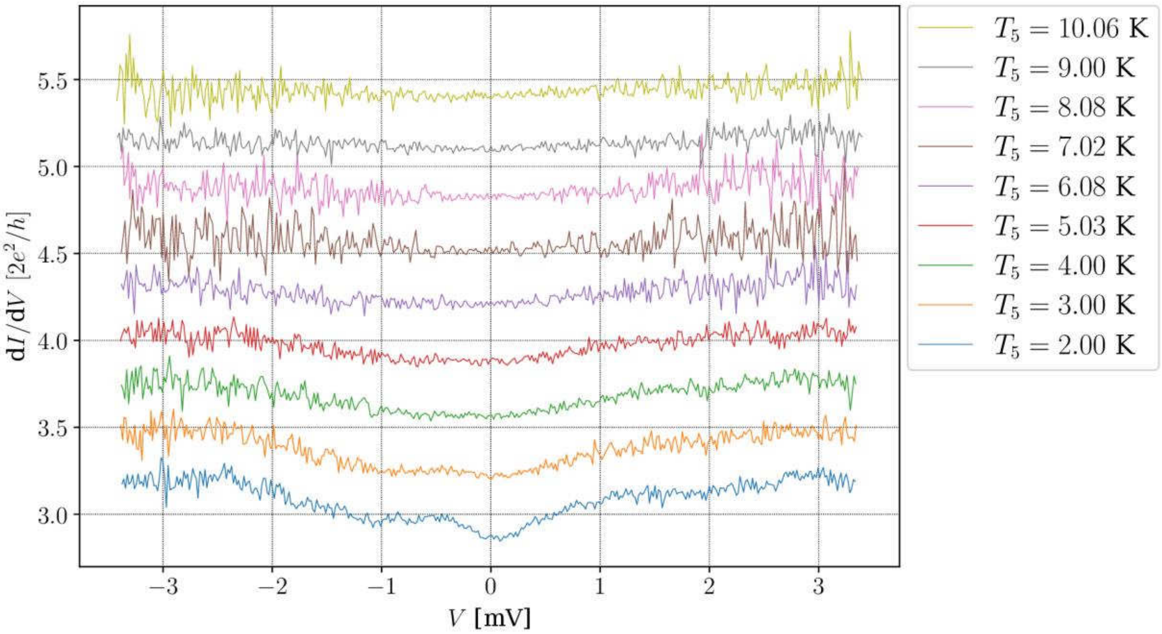

Figure 5.14: Temperature dependency from 10 K to 2 K shown in a stack plot the offset between the curves is $0.3 \times 2e^2/h$.

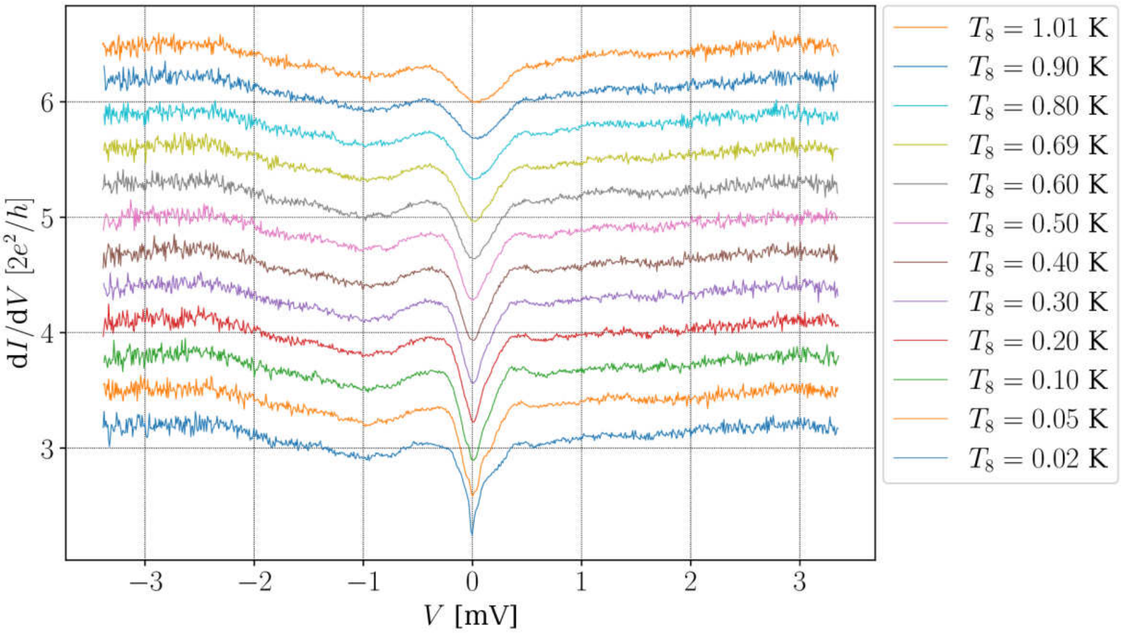

Figure 5.15: Temperature dependency from 1 K to 0.02 K shown in a stack plot. The offset between the curves is $0.3 \times 2e^2/h$.

The development of the differential conductance over temperature at zero bias voltage is shown in Figure 5.16. It can be seen that for the lowest temperature a minimum value of approx. $2.26 \times 2e^2/h$ is reached which then asymptotically increases to approx. $3 \times\ 2e^2/h$ as the temperature rises. The values used for the plot are taken from the same measurement as those for Figure 5.14, Figure 5.15 and similar measurements at other temperatures.

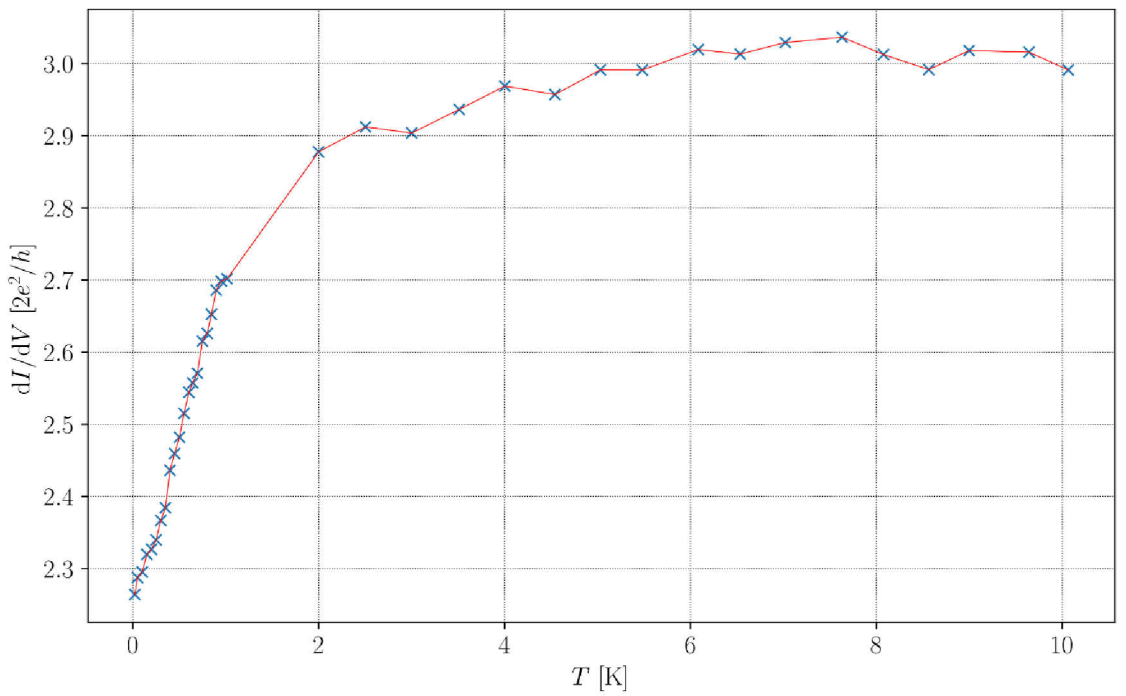

Figure 5.16: Differential conductance versus temperature at zero bias voltage taken from the data shown in Figure 5.14 and Figure 5.15.

5.3.2.1 Temperature dependence of the subgap features

It was also investigated how the subgap features behave with respect to temperature. For this purpose single IV sweeps were performed at a constant magnetic field of B = 6.4 T at different temperatures, these measurements are shown in Figure 5.17. It can be seen that the peaks only become visible when the temperature falls below about T = 0.4 K. This is probably due to the temperature-related smearing of the signatures (the distance between the peaks becomes comparable to $k_B T$ above 0.4 K).

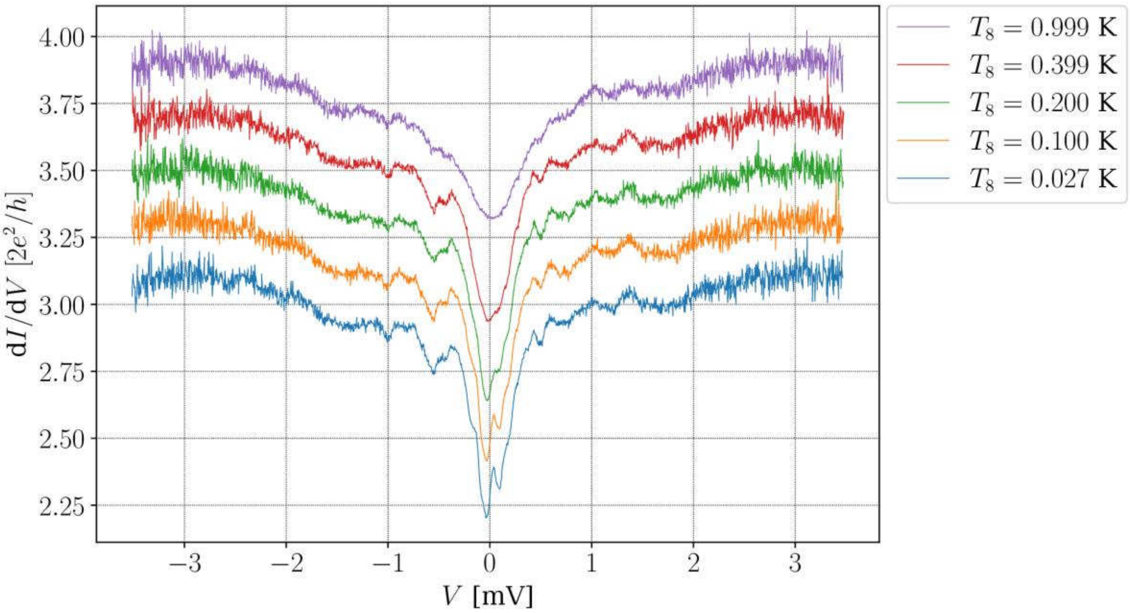

Figure 5.17: Temperature dependency from 1 K to 0.027 K with a magnetic field of 6.4 T. Shown in a stack plot the offset between the curves is $0.2 \times 2e^2/h$.

5.4 Hypothesis for the observed subgap features

In this section, I present a possible physical explanation for the subgap features visible in the measurements. A differential tunnel conductance $\mathrm{d}I/\mathrm{d}V$ from the normal conductor via an insulator into the TI nanoribbon was measured. The differential tunnel conductance $\mathrm{d}I/\mathrm{d}V$ should be proportional to the LDOS (local density of states) at the contact as shown in the section 2.4. Considering the junction geometry in Figure 5.2 it is not clear how far the proximity effect extends and influences LDOS below the barrier. By design of the tunnel junction, we are always probing LDOS below the normal contact.

The simulations showed the ZBP of a MBS for a short junction in the ballistic regime. Unfortunately this could not be observed experimentally. Instead, there are subgap features for which a physical explanation is proposed in the following section. It is important to note that the measured junction has a width of 415 nm. However, the junction is much wider than in the simulations with a width of 10 nm. The short junction in the non-diffusive regime, the behavior shown in chapter 4 is therefore not to be expected.

If the TI of the tunnel junction is in the topological phase, only one state at or close zero energy is to be expected, namely exactly the MBS. Hybridization with the MBS at the opposite end of the wire can give rise to finite energy, but close to zero if the wire is long enough and the induced gap large enough. Unfortunately this was not observed here. However, with the geometry of the junction with a width of 414 nm it is not clear whether a clearly localized MBS can be formed at the end of the nanoribbon. It can be assumed that with such a large width no clearly localized MBS can be formed at the end of the nanoribbon.

5.4.1 Andreev bound states

A model of the Andreev bound states at the end of the proximitized nanowire (the calculations can also be applied to nanoribbons with a rectangular cross section [75]) was developed together with Kristof Moors. The model does not have the limitation of special limit case considerations regarding the junction geometry.

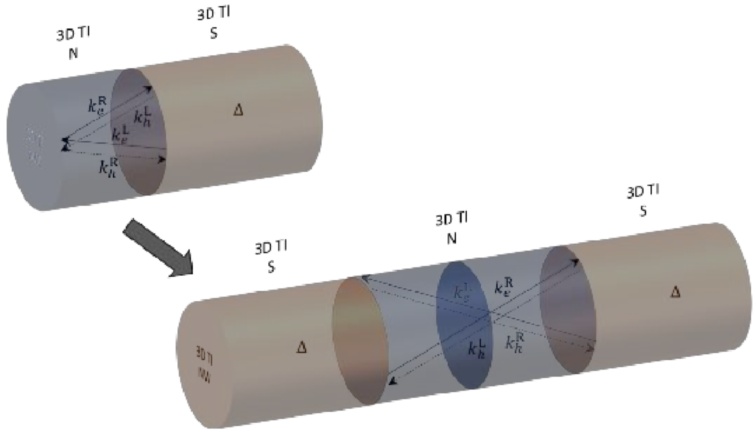

Figure 5.18: End of a proximitized nanowire with a nonproximitized region at the very end. Within the nonproximitized region, Andreev bound states are assumed. To model these Andreev bound states, the end of the nonproximitized region is thought of as being mirrored with respect to the nonproximitized region to obtain a Josephson junction. (Figures by courtesy of Kristof Moors)

The energy spectrum of a nonproximitized 3D nanoribbon with radius r and Fermi energy E_F (related to the Dirac point energy) is given by

$$E(l,k) = \pm \hbar v_{\mathrm{F}} \left(k^2 + \frac{\left(l + \frac{1}{2}\right)^2}{r^2} \right)^{\frac{1}{2}} \tag{5.1}$$

with $l = 0, \pm 1, \pm 2, \ldots$ the quantized angular momentum (different transverse modes). The energy spectrum is thus identical to the spectrum shown in equation (2.8) with $\eta = 0$. We model the nanowire end as a Josephson junction without phase difference by mirroring the nonproximitized wire end. Within the nonproximitized region, Andreev bound states are assumed with specular reflection of the bound states at that wire end shown in Figure 5.18. For the sake of simplicity, the gap Δ assumes an abrupt (steplike) change from proximitized to nonproximitized, resulting in $\Delta(z) = \Delta\Theta(z - L)$ where $0 \leq z \leq L$ applies to the nonproximitized region. In principle, the chemical potential for the proximitized and nonproximitized regions can vary greatly. However, to further simplify matters, we assume a constant chemical potential and perfect Andreev reflection. The energy spectrum results in the Andreev bound states

$$(k_{z,e} - k_{z,h})2L = 2\mathrm{arccos}\left(\left|\frac{E_{\mathrm{ABS}}}{\Delta}\right|\right) + 2\pi\mathrm{n} \tag{5.2}$$

with $n = 0, \pm 1, \pm 2, \ldots$ and the length L of the nonproximitized nanowire region. The equation represents the respective accumulated phases. The right side of the equation contains the phase difference acquired through Andreev reflection and the left side contains the accumulated phase along the nonproximitized length. This phase depends on the wave vector of the holes and electrons. The energy shown in Equation (5.1) is dependent on the wave vector of the holes and electrons, so that the following equations

$$\begin{aligned} k_{z,e} &= \pm \sqrt{\frac{(\mu + E_{\mathrm{ABS}})^2}{(\hbar v_{\mathrm{F}})^2} - \frac{\left(l + \frac{1}{2}\right)^2}{r^2}} \\ k_{z,h} &= \pm \sqrt{\frac{(\mu - E_{\mathrm{ABS}})^2}{(\hbar v_{\mathrm{F}})^2} - \frac{\left(l + \frac{1}{2}\right)^2}{r^2}} \end{aligned} \tag{5.3}$$

for holes and electrons result. This inserted in Equation (5.2) gives

$$\pm\left(\sqrt{\frac{(\mu+E_{\mathrm{ABS}})^2}{(\hbar v_F)^2}-\frac{\left(l+\frac{1}{2}\right)^2}{r^2}}-\sqrt{\frac{(\mu-E_{\mathrm{ABS}})^2}{(\hbar v_{\mathrm{F}})^2}-\frac{\left(l+\frac{1}{2}\right)^2}{r^2}}\right)2L = 2\arccos\left(\left|\frac{E_{\mathrm{ABS}}}{\Delta}\right|\right)+2\pi\mathrm{n} \tag{5.4}$$

By solving this equation for E for different l and n the spectrum of the Andreev bound states can be obtained.

To check if the peaks shown in the measurements are caused by such Andreev bound states, the spectrum is calculated for effective example values.

For the analysis shown here, we assume $E_{\mathrm{F}} = 0.1$ eV, which is in line with estimates based on Hall bar and ARPES measurements [80, 81] and $r = 135.3$ nm is used for the size. We evaluate the left- and right-hand sides of Equation (5.4) which is plotted in Figure 5.19(a-b) for a magnetic flux of $\Phi = 0 \times \Phi_0$ and $\Phi = 0.5 \times \Phi_0$. For intersections of the dashed and non-dashed curves a solution of the equation exists and thus an Andreev bound state. The plots in Figure 5.19(c-d) show the momentum of the states over the number of subbands. Figure 5.19(e-f) shows the relative energy E_{ABS}/Δ of the Andreev bound states over the number of states.

Figure 5.20(a-b) show a plot that is easier to compare to the measurements by plotting a peak at its energetic position through a Gaussian curve for each state. By summing up all these Gaussian curves, the plot is created.

The model for Andreev bound states is promising but the plot shows a clear flux quantum periodicity of the energetic position of the states with respect to the magnetic flux. However, this strong dependence on the magnetic field could not be observed for the peaks in the subgap in the measurements.

An alternative approach is to try to explain the observed peaks by a QD (quantum dot). This is tried in the following section.

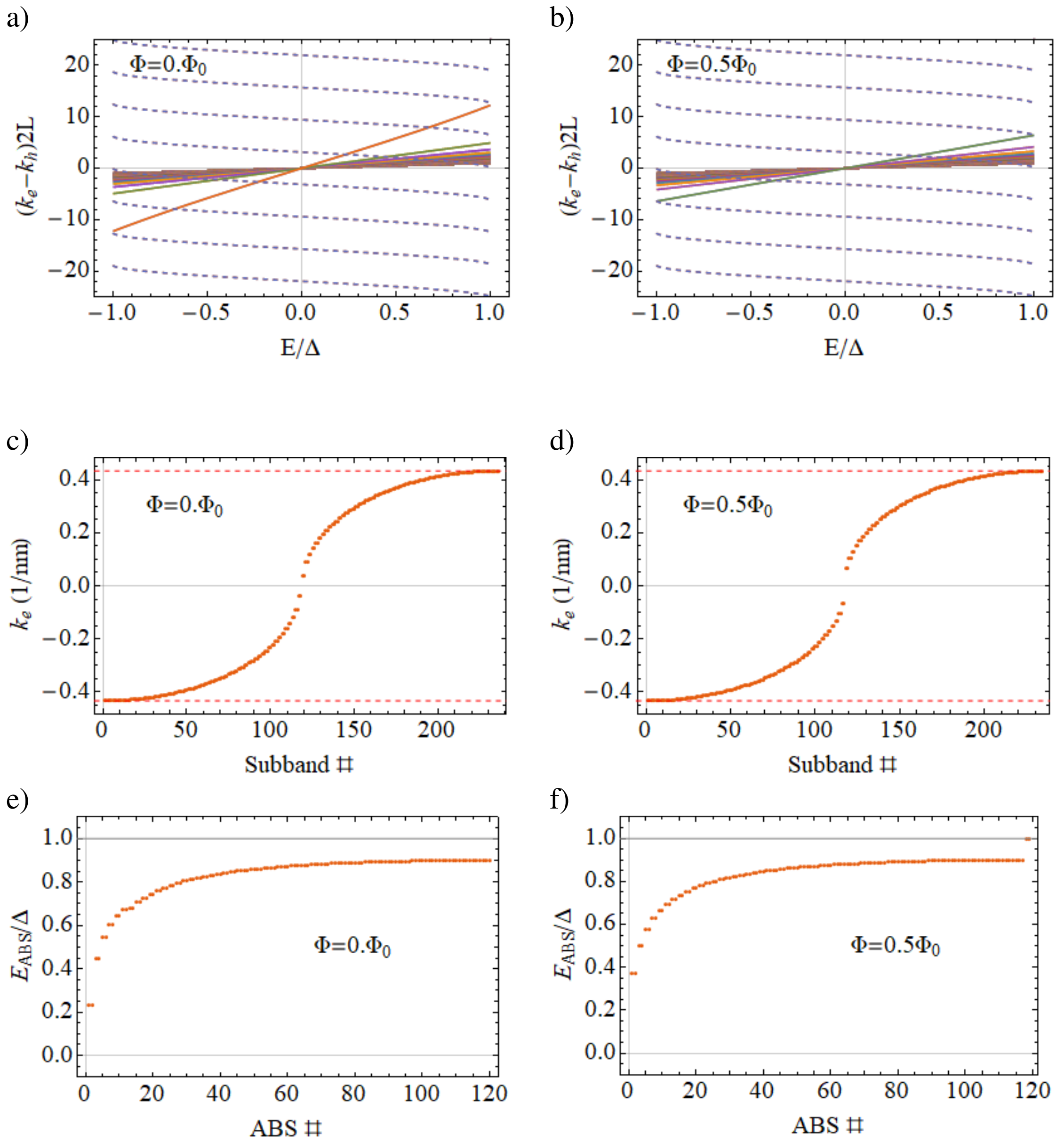

Figure 5.19: a-b) The right and left side of Equation (5.4) are plotted so that a solution of the equation exists for intersections of the dashed and non-dashed curves and thus an Andreev-bound state. c- d) Momentum of the states over the number of subbands. e- f) The relative energy E_{ABS}/Δ *of the Andreev bound states over the number of states (Figures by courtesy of Kristof Moors).*

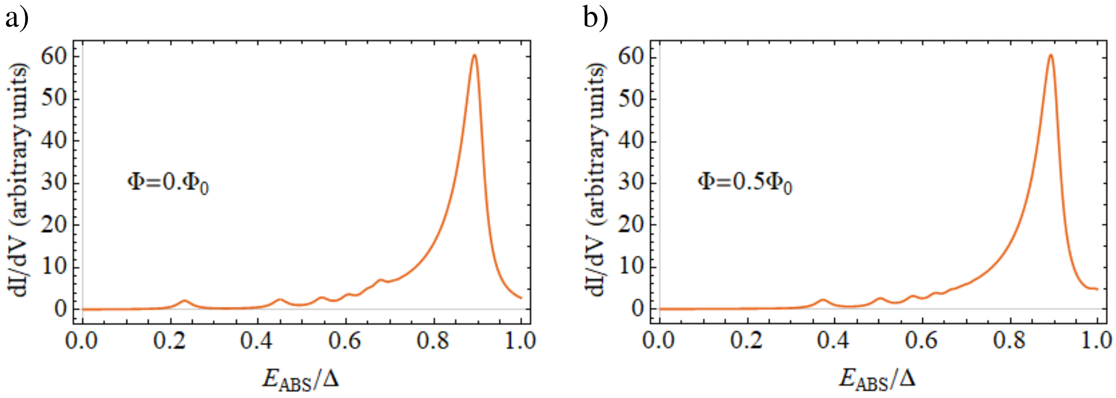

Figure 5.20: Plotting a peak at its energetic position through a Gaussian curve for each state. By summing up all these Gaussian curves, the plot is created (Figures by courtesy of Kristof Moors).

5.4.2 Quantum dot and Coulomb blockade

Rather than considering Andreev bound states or MBS, an alternative explanation that is consistent with the observed subgap features are charge effects of a QD. If the tunnel contact is considered as a barrier to a QD, the capacity of the tunnel barrier results in a charge energy in the range of 0.1 meV, which is approximately the distance of the subgap features. The exact calculation is shown below

$$\Delta E_{\mathrm{QD}} = \frac{e^2}{C} = \frac{e^2}{1.433 \times 10^{-15}\ \mathrm{F}} = 0.11\ \mathrm{meV}$$
$$C = \varepsilon_0 \varepsilon_{\mathrm{r}} \cdot \frac{A}{d} = \varepsilon_0 \cdot 9 \cdot \frac{130\ \mathrm{nm} \cdot 415\ \mathrm{nm}}{3\ \mathrm{nm}} = 1.433 \times 10^{-15}\ \mathrm{F}. \tag{5.5}$$

The energy levels of the QD have an equidistant distance of ΔE with the electron charge e. The capacitance of the QD is C and results from the above calculation since a parallel plate capacitor is assumed for the barrier. The capacitance is proportional to the area of the contact covering the wire end and is inversely proportional to the thickness of the barrier.

If a QD is assumed to exist, the subgap features are caused by charging effects of single electrons on this QD. For such a single electron charge a weak coupling of source and drain to the QD is required. This can be considered as present with the tunnel barrier and the TI proximitized-TI interface as barrier.

In the case of the TI-S interface, if the whole ribbon is considered to be the QD, charge parity effects should show up, an effect that is due to the fact that Cooper pairs have a charge of $2e$. This results in different charge energies for an even or odd number of electrons on the QD. However, this cannot be observed and can therefore be excluded.

Consequently, it can be assumed that the QD consists of the nonproximitized ribbon region. From early experiments (see Refs. [82, 83], for examples) it is known that bulk contribution is dominant in normal (magneto)transport measurements. So it cannot be excluded that the QD extends into the (nonproximitized) bulk. Now as a condition for the occurrence of Coulomb blockade it has to be checked if the energy of the QD is dominated by the charging energy. This can be checked by calculating the energy distance that can be expected for a normal electron gas at Fermi Energy E_F

$$\rho(E_F) = \frac{(2m^*)^{\frac{3}{2}}}{2\pi^2\hbar^3\sqrt{E_F}}, \tag{5.6}$$

$$\Delta E_{\mathrm{EG}} = \frac{1}{\rho(E_F)V}. \tag{5.7}$$

If $E_F = 0.056\,\mathrm{eV}$ and $m^* = 0.58m_{\mathrm{e}}$ [80] is assumed, an energy distance of $\Delta E_{\mathrm{EG}} = 7.357 \times 10^{-4}\,\mathrm{meV}$ results.

The energy distances are four orders of magnitude smaller than those of the QD. The condition is therefore fulfilled and a QD formed by the nonproximitized bulk region can be considered as a possible explanation for the subgap features shown.

Even though the QD interpretation is very promising and in good agreement with the observed subgap peaks and their properties like $\Delta E_{\mathrm{QD}} = 0.11\,\mathrm{meV}$ and low magnetic field dependence, some questions remain. What is the barrier on the superconductor contact side? To realize a Coulomb blockade regime, the QD must be sufficiently isolated from all the leads. It can be argued that the TI-STI interface forms another barrier. Furthermore, due to the geometry and the resulting steep angle of incidence, Andreev reflections are less likely to occur at this interface. However, this only applies to states with high transverse velocity that show up in the middle of the gap. Nevertheless, this could cause further electrical isolation.

6 Conclusion & Outlook

In summary, it has been successfully demonstrated that the fabrication of complex nanostructures such as a tunnel junction consisting of up to four different materials is possible *in situ* using stencil lithography. By precisely optimizing the layout geometry for the stencil lithography mask, it was possible to ensure that the normal conducting contacts were precisely aligned with the 3D-TI nanoribbon without losing the integrity of the mask. Python scripts were used to create a large number of test structures with different geometries on one sample. A simple model for estimating the influence of the stencil lithography mask shadow on the rotation deposition was developed.

The general behavior of the tunnel junction could be determined. The measurements showed the opening of a soft gap with a gap width 2Δ of about 300 µeV to 400 µeV. This gap starts to open at about 2 K and becomes deeper and more V-shaped as the temperature decreases. Thus, it can be assumed that the TI was successfully proximitized by the Nb and that the density of states at the contact point was measured through a tunnel barrier. The results can be considered as a proof of concept, as they confirm the general feasibility of the concept of an *in situ* tunnel junction.

Our first results did not show the expected ZBP for a MBS at the nanoribbon end and our analysis shows that the structure needs further optimization (see outlook below). Instead of a ZBP in the middle of the gap, I identified a robust and equidistant subgap peak spectrum. These peaks indicate the presence of a charge energy dominated QD at the 3D-TI nanoribbon end. Andreev bound states have also been discussed as possible explanations for the measurement results. However, they show an unobserved strong magnetic field dependence in the model. The shown hypotheses are therefore promising and can give hints for future investigations.

Additionally, a model for the numerical simulation of the quantum transport behavior of such proximitized 3D-TI tunnel junctions has been developed. In these simulations a ZBP quantized in height at $2e^2/h$ could be successfully shown.

Outlook

For future work on the tunnel junction shown in this thesis, many questions remain open. The quality and thickness of the tunnel barrier used here are still rather unclear. In order to optimize these questions, transmission electron microscopy (TEM) investigations of the tunnel barrier and the individual interfaces would be very interesting. This could provide information about the exact thickness and quality of the barrier.

Measurements of tunneling junctions with different widths and lengths would also be very helpful to better interpret the data. Since the primary goal is the detection of MBS, the focus for future junction detection should be on reducing the junction width. This would reduce the influence of any QD and reduce the number of possible modes. A better localization of the MBS is also expected. With regard to the QD, reducing the normal contact width (not to be confused with the TI nanoribbon width) at the barrier would be sufficient to increase the QD charging energy.

Exact information about which widths are promising is difficult to give for 3D-TIs. Here further simulations could provide helpful information. As a guideline it would be useful to simulate or measure the widths (approx. 100 nm) of the semiconductor nanowires in which MBSs have already been shown [7, 11-15].

A significant step forward would be the possibility to use gates. The fabrication of these gates is currently prevented by the substrate used in the case of a back gate and by the mask in the case of top gates. Thus, a back gate could be used to influence the chemical potential, offering new possibilities to characterize the tunnel junction. Side gates at the contacts could also be used to study the influence of a possible QD. Such a tunnel contact with side gate could look like the one shown in Figure 6.1.

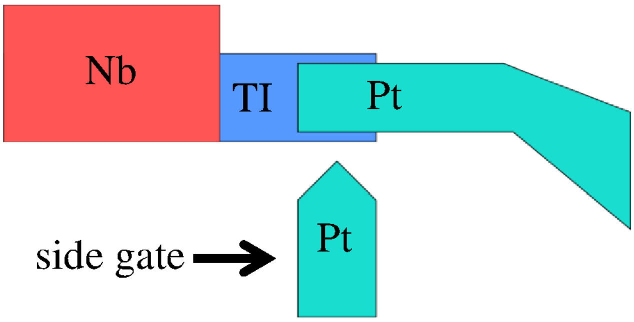

Figure 6.1: Schematic diagram of a top view of a tunnel contact with side gate to influence the energy levels of a QD which may be present at the contact.

7 Acknowledgments

Many great people have supported and helped me for this thesis. In this section I would like to thank them.

I would like to thank Prof. Dr. Detlev Grützmacher who gave me the opportunity to work on such an exciting topic as TIs at the Peter Grünberg Institute (PGI-9).

I would like to thank Prof. Dr. Markus Morgenstern for taking up the role of the second examiner of this master thesis.

A big thank you goes to my supervisor Tobias Schmitt for his patient guidance; his extensive knowledge about the production of nanostructures was very helpful. I also went with Tobias to Twente for a measurement stay, his tireless support during the measurements made the interesting results possible.

Special thanks go to Dr. Peter Schüffelgen for his open and patient management style, which always ensured a good working atmosphere in the group. His enthusiasm and optimism was always contagious and a great source of motivation. His guidance has helped me develop further during my time at Jülich, both personally and in relation to science.

A big thank you goes to Dr. Kristof Moors for his theoretical support. Only the detailed discussions with him made it possible to understand the measurement data. His support in the development of the Kwant model was very helpful. I also want to thank him for the meticulous correction instructions he gave me for this thesis. Through them I learned a lot about how scientific texts should be written.

I would like to thank Michael Schleenvoigt who did the growth of TIs and the deposition of metals together with Max Vaßen-Carl. Here I would also like to thank Benjamin Bennemann for his support during the deposition in the Nano-cluster.

Special thanks to Prof. Dr. Alexander Brinkman of MESA+ Institute of Nanotechnology at the University of Twente for providing the measurement time in their dilution refrigerator. In this context I would also like to thank Prof. Dr. Chuan Li and Daan Wielens for their help in carrying out these measurements.

I would like to thank Dr. Elmar Neumann and Stephany Bunteand for their introduction to SEM imaging. They always had helpful advice available to get good images.

I would like to thank Dr. Florian Lentz for his support in electron beam lithography and his patience in discussing my layouts where he always brought in his deep knowledge.

Thanks to the whole HNF team for their introduction to cleanroom processes. They were always able to help with questions about the various processes.

I would like to thank Jonas Kölzer for providing an important resource for good research, namely good coffee. I thank Anton Faustmann for providing his inexhaustible supply of sweets.

Last but not least, I would like to thank my family without their help I would never have come this far.

8 Bibliography

1. Feynman, R.P., *Simulating physics with computers.* International Journal of Theoretical Physics, 1982. **21**(6): p. 467-488 DOI: 10.1007/BF02650179.

2. Shor, P.W., *Scheme for reducing decoherence in quantum computer memory.* Physical Review A, 1995. **52**(4): p. R2493-R2496 DOI: 10.1103/PhysRevA.52.R2493.

3. Hasan, M.Z. and C.L. Kane, *Colloquium: Topological insulators.* Rev. Mod. Phys., 2010. **82**(4): p. 3045-3067 DOI: 10.1103/RevModPhys.82.3045.

4. Hyart, T., et al., *Flux-controlled quantum computation with Majorana fermions.* Phys. Rev. B, 2013. **88**(3): p. 035121 DOI: 10.1103/PhysRevB.88.035121.

5. Alicea, J., et al., *Non-Abelian statistics and topological quantum information processing in 1D wire networks.* Nature Physics, 2011. **7**(5): p. 412-417 DOI: 10.1038/nphys1915.

6. Majorana, E. and L. Maiani, *A symmetric theory of electrons and positrons*, in *Ettore Majorana Scientific Papers: On occasion of the centenary of his birth*, G.F. Bassani, Editor. 2006, Springer Berlin Heidelberg: Berlin, Heidelberg. p. 201-233.

7. Mourik, V., et al., *Signatures of Majorana Fermions in Hybrid Superconductor-Semiconductor Nanowire Devices.* Science, 2012. **336**(6084): p. 1003-1007 DOI: 10.1126/science.1222360.

8. Sun, H.-H. and J.-F. Jia, *Detection of Majorana zero mode in the vortex.* npj Quantum Materials, 2017. **2**(1): p. 34 DOI: 10.1038/s41535-017-0037-4.

9. Nichele, F., et al., *Scaling of Majorana Zero-Bias Conductance Peaks.* Physical Review Letters, 2017. **119**(13): p. 136803 DOI: 10.1103/PhysRevLett.119.136803.

10. Schüffelgen, P., et al., *Selective area growth and stencil lithography for in situ fabricated quantum devices.* Nature Nanotechnology, 2019. **14**(9): p. 825-831 DOI: 10.1038/s41565-019-0506-y.

11. Chen, J., et al., *Ubiquitous Non-Majorana Zero-Bias Conductance Peaks in Nanowire Devices.* Physical Review Letters, 2019. **123**(10): p. 107703 DOI: 10.1103/PhysRevLett.123.107703.

12. Deng, M.T., et al., *Majorana bound state in a coupled quantum-dot hybrid-nanowire system.* Science, 2016. **354**: p. 1557-1562.

13. Grivnin, A., et al., *Concomitant opening of a bulk-gap with an emerging possible Majorana zero mode.* Nature Communications, 2019. **10**(1): p. 1940 DOI: 10.1038/s41467-019-09771-0.

14. Gül, Ö., et al., *Ballistic Majorana nanowire devices.* Nature Nanotechnology, 2018. **13**(3): p. 192-197 DOI: 10.1038/s41565-017-0032-8.

15. Das, A., et al., *Zero-bias peaks and splitting in an Al–InAs nanowire topological superconductor as a signature of Majorana fermions.* Nature Physics, 2012. **8**(12): p. 887-895 DOI: 10.1038/nphys2479.

16. Liu, C.-X., et al., *Andreev bound states versus Majorana bound states in quantum dot-nanowire-superconductor hybrid structures: Trivial versus topological zero-bias conductance peaks.* Physical Review B, 2017. **96**(7): p. 075161 DOI: 10.1103/PhysRevB.96.075161.

17. Pan, H. and S. Das Sarma, *Physical mechanisms for zero-bias conductance peaks in Majorana nanowires.* Physical Review Research, 2020. **2**(1): p. 013377 DOI: 10.1103/PhysRevResearch.2.013377.

18. Ngabonziza, P., et al., *In situ spectroscopy of intrinsic Bi2Te3 topological insulator thin films and impact of extrinsic defects.* Phys. Rev. B, 2015. **92**(3): p. 035405 DOI: 10.1103/PhysRevB.92.035405.

19. Thomas, C.R., et al., *Surface Oxidation of Bi2(Te,Se)3 Topological Insulators Depends on Cleavage Accuracy.* Chemistry of Materials, 2016. **28**(1): p. 35-39 DOI: 10.1021/acs.chemmater.5b03923.

20. Kane, C.L. and E.J. Mele, *Z2 Topological Order and the Quantum Spin Hall Effect.* Physical Review Letters, 2005. **95**(14): p. 146802 DOI: 10.1103/PhysRevLett.95.146802.

21. Kane, C.L. and E.J. Mele, *Quantum Spin Hall Effect in Graphene.* Physical Review Letters, 2005. **95**(22): p. 226801 DOI: 10.1103/PhysRevLett.95.226801.

22. Thouless, D.J., et al., *Quantized Hall Conductance in a Two-Dimensional Periodic Potential.* Physical Review Letters, 1982. **49**(6): p. 405-408 DOI: 10.1103/PhysRevLett.49.405.

23. Fu, L., C.L. Kane, and E.J. Mele, *Topological Insulators in Three Dimensions.* Physical Review Letters, 2007. **98**(10): p. 106803 DOI: 10.1103/PhysRevLett.98.106803.

24. Moore, J.E. and L. Balents, *Topological invariants of time-reversal-invariant band structures.* Physical Review B, 2007. **75**(12): p. 121306 DOI: 10.1103/PhysRevB.75.121306.

25. Roy, R., *Topological phases and the quantum spin Hall effect in three dimensions.* Physical Review B, 2009. **79**(19): p. 195322 DOI: 10.1103/PhysRevB.79.195322.

26. Schäpers, T., *Semiconductor Spintronics*. 2016, Berlin, Boston: De Gruyter.

27. Bansil, A., H. Lin, and T. Das, *Colloquium: Topological band theory.* Reviews of Modern Physics, 2016. **88**(2): p. 021004 DOI: 10.1103/RevModPhys.88.021004.

28. Zhang, H., et al., *Topological insulators in Bi2Se3, Bi2Te3 and Sb2Te3 with a single Dirac cone on the surface.* Nature Physics, 2009. **5**(6): p. 438-442 DOI: 10.1038/nphys1270.

29. Cook, A. and M. Franz, *Majorana fermions in a topological-insulator nanowire proximity-coupled to an s-wave superconductor.* Phys. Rev. B, 2011. **84**(20): p. 201105 DOI: 10.1103/PhysRevB.84.201105.

30. Cook, A.M., M.M. Vazifeh, and M. Franz, *Stability of Majorana fermions in proximity-coupled topological insulator nanowires.* Phys. Rev. B, 2012. **86**(15): p. 155431 DOI: 10.1103/PhysRevB.86.155431.

31. Cook, A. and M. Franz. *Majorana Fermions in Proximity-coupled Topological Insulator Nanowires*. 2011.

32. Schüffelgen, P., *Exploiting topological insulators for Majorana devices and physics via molecular beam epitaxy*. 2018.

33. Veldhorst, M., et al., *Josephson supercurrent through a topological insulator surface state.* Nature Materials, 2012. **11**(5): p. 417-421 DOI: 10.1038/nmat3255.

34. Zhang, J., et al., *Band structure engineering in (Bi1−xSbx)2Te3 ternary topological insulators.* Nature Communications, 2011. **2**(1): p. 574 DOI: 10.1038/ncomms1588.

35. Kong, D., et al., *Ambipolar field effect in the ternary topological insulator (BixSb1−x)2Te3 by composition tuning.* Nature Nanotechnology, 2011. **6**(11): p. 705-709 DOI: 10.1038/nnano.2011.172.

36. Li, H.D., et al., *Growth of multilayers of Bi2Se3/ZnSe: Heteroepitaxial interface formation and strain.* Applied Physics Letters, 2011. **98**(4): p. 043104 DOI: 10.1063/1.3548865.

37. Alpichshev, Z., et al., *STM Imaging of Electronic Waves on the Surface of Bi2Te3: Topologically Protected Surface States and Hexagonal Warping Effects.* Physical Review Letters, 2010. **104**(1): p. 016401 DOI: 10.1103/PhysRevLett.104.016401.

38. Wang, G., et al., *Atomically smooth ultrathin films of topological insulator Sb2Te3.* Nano Research, 2010. **3**(12): p. 874-880 DOI: 10.1007/s12274-010-0060-2.

39. Hsieh, D., et al., *Observation of Time-Reversal-Protected Single-Dirac-Cone Topological-Insulator States in Bi2Te3 and Sb2Te3.* Physical Review Letters, 2009. **103**(14): p. 146401 DOI: 10.1103/PhysRevLett.103.146401.

40. Weyrich, C., et al., *Growth, characterization, and transport properties of ternary (Bi1−xSbx)2Te3topological insulator layers.* Journal of Physics: Condensed Matter, 2016. **28**(49): p. 495501 DOI: 10.1088/0953-8984/28/49/495501.

41. Onnes, H.K., *Further Experiments with Liquid Helium. D. On the Change of the Electrical Resistance of Pure Metals at very low Temperatures, etc. V. The Disappearance of the resistance of mercury.* Through Measurement to Knowledge, 1991: p. 264-266 DOI: 10.1007/978-94-009-2079-8_16.

42. van Delft, D. and P. Kes, *The discovery of superconductivity.* Physics Today, 2010. **63**(9): p. 38-43 DOI: 10.1063/1.3490499.

43. Lévy, L.-P., *Ginzburg-Landau Theory.* Magnetism and Superconductivity, 2000: p. 285-307 DOI: 10.1007/978-3-662-04271-7_13.

44. Bardeen, J., L.N. Cooper, and J.R. Schrieffer, *Theory of Superconductivity.* Physical Review, 1957. **108**(5): p. 1175-1204 DOI: 10.1103/PhysRev.108.1175.

45. Meissner, W. and R. Ochsenfeld, *Ein neuer Effekt bei Eintritt der Supraleitfähigkeit.* Naturwissenschaften, 1933. **21**: p. 787-788 DOI: 10.1007/BF01504252.

46. Tinkham, M., *Introduction to Superconductivity*. Dover Books on Physics Series. 2004: Dover Publications.

47. Deaver, B.S. and W.M. Fairbank, *Experimental Evidence for Quantized Flux in Superconducting Cylinders.* Physical Review Letters, 1961. **7**(2): p. 43-46 DOI: 10.1103/PhysRevLett.7.43.

48. Bardeen, J., L.N. Cooper, and J.R. Schrieffer, *Microscopic Theory of Superconductivity.* Physical Review, 1957. **106**(1): p. 162-164 DOI: 10.1103/PhysRev.106.162.

49. Cooper, L.N., *Bound Electron Pairs in a Degenerate Fermi Gas.* Physical Review, 1956. **104**(4): p. 1189-1190 DOI: 10.1103/PhysRev.104.1189.

50. Sato, M. and Y. Ando, *Topological superconductors: a review.* Reports on Progress in Physics, 2017. **80**(7): p. 076501 DOI: 10.1088/1361-6633/aa6ac7.

51. Schäpers, T., *Superconductor/Semiconductor Junctions*. Vol. 174. 2001.

52. McMillan, W.L., *Theory of Superconductor---Normal-Metal Interfaces.* Physical Review, 1968. **175**(2): p. 559-568 DOI: 10.1103/PhysRev.175.559.

53. Buckel, W. and R. Kleiner, *Supraleitung: Grundlagen und Anwendungen*. 2013: Wiley.

54. Courtois, H., et al., *Long-range coherence and mesoscopic transport in N–S metallic structures.* Superlattices and Microstructures, 1999. **25**(5): p. 721-732 DOI: 10.1006/spmi.1999.0711.

55. Kitaev, A.Y., *Unpaired Majorana fermions in quantum wires.* Physics-Uspekhi, 2001. **44**(10S): p. 131-136 DOI: 10.1070/1063-7869/44/10s/s29.

56. Qi, X.-L. and S.-C. Zhang, *Topological insulators and superconductors.* Rev. Mod. Phys., 2011. **83**(4): p. 1057-1110 DOI: 10.1103/RevModPhys.83.1057.

57. Majorana, E., *Teoria simmetrica dell'elettrone e del positrone.* Il Nuovo Cimento (1924-1942), 2008. **14**(4): p. 171 DOI: 10.1007/BF02961314.

58. Alicea, J., *New directions in the pursuit of Majorana fermions in solid state systems.* Reports on Progress in Physics, 2012. **75**(7): p. 076501 DOI: 10.1088/0034-4885/75/7/076501.

59. André Melo, C.-X.L., Piotr Rożek, Tómas Örn Rosdahl, Michael Wimmer, *Conductance asymmetries in mesoscopic superconducting devices due to finite bias.*

60. Franz, M., *Majorana's wires.* Nature Nanotechnology, 2013. **8**(3): p. 149-152 DOI: 10.1038/nnano.2013.33.

61. Benia, H.M., et al., *Reactive Chemical Doping of the Bi2Se3 Topological Insulator.* Phys. Rev. Lett., 2011. **107**(17): p. 177602 DOI: 10.1103/PhysRevLett.107.177602.

62. Lang, M., et al., *Revelation of Topological Surface States in Bi2Se3 Thin Films by In Situ Al Passivation.* ACS Nano, 2012. **6**(1): p. 295-302 DOI: 10.1021/nn204239d.

63. Ngabonziza, P., et al., *Gate-Tunable Transport Properties of In Situ Capped Bi2Te3 Topological Insulator Thin Films.* Advanced Electronic Materials, 2016. **2**(8): p. 1600157 DOI: 10.1002/aelm.201600157.

64. Rosenbach, D., *Induced superconductivity in molecular beam epitaxy grown topologicalinsulator thin films, Master’s thesis, University of Twente.* 2016.

65. Schmitt, T., *Low-dimensional Josephson junctions based on molecular beam epitaxy grown topological insulator thin fims, Master’s thesis, RWTH Aachen.* 2017.

66. Kampmeier, J., et al., *Selective area growth of Bi2Te3 and Sb2Te3 topological insulator thin films.* Journal of Crystal Growth, 2016. **443**: p. 38-42 DOI: 10.1016/j.jcrysgro.2016.03.012.

67. Weyrich, C., et al., *Phase-coherent transport in selectively grown topological insulator nanodots.* Nanotechnology, 2018. **30**(5): p. 055201 DOI: 10.1088/1361-6528/aaee5f.

68. Matthias, K., *KLayout*.

69. Groth, C.W., et al., *Kwant: a software package for quantum transport.* New Journal of Physics, 2014. **16**(6): p. 063065 DOI: 10.1088/1367-2630/16/6/063065.

70. Díez Mérida, J., *Tunneling Spectroscopyona Phase Tunable Topological Josephson Junction*.

71. Ren, H., et al., *Topological superconductivity in a phase-controlled Josephson junction.* Nature, 2019. **569**(7754): p. 93-98 DOI: 10.1038/s41586-019-1148-9.

72. Liu, C.-X., et al., *Model Hamiltonian for topological insulators.* Phys. Rev. B, 2010. **82**(4): p. 045122 DOI: 10.1103/PhysRevB.82.045122.

73. Nijholt, B., *Towards realistic numerical simulations of Majorana devices.* 2020(2020-11) DOI: 10.4233/uuid:6cdf1184-ce38-412d-a3a5-1a793c787e58.

74. Peierls, R., *Zur Theorie des Diamagnetismus von Leitungselektronen.* Zeitschrift für Physik, 1933. **80**(11): p. 763-791 DOI: 10.1007/BF01342591.

75. Moors, K., et al., *Magnetotransport signatures of three-dimensional topological insulator nanostructures.* Physical Review B, 2018. **97**(24): p. 245429 DOI: 10.1103/PhysRevB.97.245429.

76. de Juan, F., J.H. Bardarson, and R. Ilan, *Conditions for fully gapped topological superconductivity in topological insulator nanowires.* SciPost Physics, 2019. **6**(5): p. 060 DOI: 10.21468/SciPostPhys.6.5.060.

77. Weyrich, C., et al., *Growth, characterization, and transport properties of ternary (Bi1-xSbx)2Te3 topological insulator layers.* Journal of Physics: Condensed Matter, 2016. **28**(49): p. 495501 DOI: 10.1088/0953-8984/28/49/495501.

78. Kölzer, J., et al., *Phase-coherent loops in selectively-grown topological insulator nanoribbons.* Nanotechnology, 2020. **31**(32): p. 325001 DOI: 10.1088/1361-6528/ab898a.

79. Narlikar, A.V., *Superconductors*. 2014: OUP Oxford.

80. Eschbach, M., *Band structure engineering in 3D topological insulators investigated by angle-resolved photoemission spectroscopy*. 2016, Forschungszentrum Jülich GmbH, Zentralbibliothek: Jülich.

81. Rosenbach, D., et al., *Quantum Transport in Topological Surface States of Selectively Grown Bi2Te3 Nanoribbons.* Advanced Electronic Materials, 2020. **6**(8): p. 2000205 DOI: 10.1002/aelm.202000205.

82. Peng, H., et al., *Aharonov–Bohm interference in topological insulator nanoribbons.* Nature Materials, 2010. **9**(3): p. 225-229 DOI: 10.1038/nmat2609.

83. Qu, D.-X., et al., *Quantum Oscillations and Hall Anomaly of Surface States in the Topological Insulator Bi2Te3.* Science, 2010. **329**(5993): p. 821 DOI: 10.1126/science.1189792.